NORTHWESTERN UNIVERSITY

Nonlinear Dynamical Models: Politics, Stochastics, and a Mexican Hat Dance

A DISSERTATION

SUBMITTED TO THE GRADUATE SCHOOL

IN PARTIAL FULFILLMENT OF THE REQUIREMENTS

for the degree

DOCTOR OF PHILOSOPHY

Field of Engineering Sciences and Applied Mathematics

By

David Sabin-Miller

EVANSTON, ILLINOIS

December 2022

ABSTRACT

Nonlinear Dynamical Models: Politics, Stochastics, and a Mexican Hat Dance

David Sabin-Miller

Dynamical modeling aims to capture the essential mechanics at work in real-world systems while remaining tractable enough to yield mathematical insights for predictions and interventions. The work presented here first takes this approach to the system of political ideology and influence, establishing a model for the continuous-time evolution of individual and population-level ideological distributions. This model strikes a middle ground of complexity, eschewing the normal network- or agent-based approach while maintaining significantly more nonlinear realism than statistical-physics models. Second, we explore an under-studied and formerly ill-defined technical roadblock of that model and establish a technique for properly dealing with other such stochastic systems. Finally we examine a nonlinear potential-coupled particle system with unique self-organizing behavior.

Acknowledgements

First and foremost, these three projects were explored in close collaboration with my advisor, Danny Abrams, whose willingness to try new things and push boundaries allowed me to stick my nose into multiple different fields to produce this broadly interdisciplinary body of work. I am excited to carry this mindset of fearlessly curiosity-following scholarship forward into my academic career.

While her name doesn't appear on any of the manuscripts to follow, I spent plenty of hours collaborating with Northwestern-based political science professor Mary McGrath on the follow-up experiment to the political modeling work—see Section 1.E—and I anticipate working more with her as that project comes to fruition. I deeply appreciate her perspective and assurance that our approach isn't crazy and is actually pretty unique and exciting.

I also owe a debt of gratitude to my graduate committee, Hermann Riecke and Niall Mangan, for their insightful questions and support. The second project explored herein was accelerated significantly by one of Hermann's questions pointing out a flaw in a previous approach to simulating randomness.

I have also benefitted from the feedback and support of other members of the ESAM department here at Northwestern. Bill Kath, Gary Nave, Jithin George, and Andre Archer have all contributed to this work through their thoughts and suggestions.

On a more personal note, my partner Dyani Sabin has been absolutely essential to my success through her support and encouragement, and as a test-subject for sanity checks and (at least marginal) understandability. Similarly, my family has been unwavering in their encouragement.

Lastly, I would like to thank the National Science Foundation Graduate Research Fellowship Program (NSF GRFP) for believing in my vision and providing me funding to pursue these projects I believe will benefit the world, even if it requires a leap of faith away from established work.

Preface

Modeling is both an art and a science. Each new dynamic comes with inherent complexity, leading to a constant balancing act of capturing sufficient realism without becoming overcomplicated. This work has been an ongoing attempt to capture sufficient core dynamics to say something real and new, yet focusing on sufficiently nice examples that we can make reasonably "clean" mathematical statements. This theme applies to all three projects: 1) establishing a political modeling framework which produces tractable predictions while being adaptable to plausibly attainable data, 2) handling a new type of stochasticity and demonstrating its effect on a basic new class of attractor, and 3) exploring/elucidating typical bulk behavior in a complex coupled system of interacting particles.

This work has been a process of finding and following various rabbit-holes, most of which are dead ends, until arriving at positions of value worth sharing—then paving the path followed so others needn't follow the same convoluted route.

The first chapter is based around the political-modeling project, which produced the manuscript "When pull turns to shove: A continuous-time model for opinion dynamics" which was published in Physical Review Research in October 2020 [**1**]. This project attempts to capture sufficient core psychological tendencies and societal forces to build up to population-level ideological distributions. The validation and extension of this work

is ongoing, and hopefully will aid in the endeavor to understand vital and often worrying systems of power.

The second chapter covers a project spun off from that initial work, and compiled in the yet-unpublished manuscript entitled "Modeling and analysis of systems with nonlinear functional dependence on random quantities." [**2**] Our political model included a thorny new type of stochasticity, which ended up requiring the establishment of more general basic definitions in stochastic analysis. This type of stochasticity is subtly different from anything we have seen covered in the literature before, yet we argue may easily arise in a wide variety of modeling contexts, and even perhaps the basic situation of particle velocity amidst turbulence.

The third chapter is based on our working manuscript "A Mexican hat dance: System of Ricker-potential-coupled particles." A seemingly-basic question about coupled particles ended up giving birth to a rich and complex paradigm, which we explore to find some unexpectedly fascinating dynamical behavior, and point at several yet-unexplored frontiers in its study.

Table of Contents

List of Figures

is potentially well-defined. It is important to note the vertical axis scale is different, however; any additional invariance involved in this limit would involve a rescaling the vertical (spatial) axis as well as the existing horizontal axis scaling (implicit in w_0 dependence, since $w_0 \propto k^{-1/2}$). 112

3.S18 **Other Classic Potentials.** Examples of the Lennard-Jones (**left**) and Morse (**right**) potentials from physics. Parameters have been chosen to match the trough coordinates of our default-parameter Ricker potential—$(\pm 1, e^{-2})$—and the peak of $(0, 1)$ for the Morse potential. Still, we note significant qualitative discrepancies, namely the infinite central spike for Lennard-Jones and the "sharp" origin peak for Morse. These qualities preclude the stability (or even well-defined status) of stacking behavior, and thus the particular richness of behavior we find in our Ricker system, but alterations to smooth behavior at the origin may lead to reconciliation. 114

3.S19 **Oscillator interpretation, slow convergence.** Ten Ricker oscillators with preferred distance $2\pi/10$. The left figure shows the system at time $t = 5$, central figure at $t = 25$, and right figure at $t = 30$; the population swiftly self-arranges to become near-evenly but too-compactly arranged, then slowly separates, until suddenly "snapping" to perfectly even spacing. Black dots around circle indicate preferred distance; we see the particles eventually space themselves at the same intervals. Color indicates particle index, to distinguish and keep track of them over time.

115

3.S20 **Ricker oscillator system.** Two hundred Ricker oscillators with preferred distance $2\pi/6$. **Top left:** Random starting state. **Top right:** At $T = 0.1$, the particles have very quickly arranged themselves into a single low-frequency global-potential wave. **Bottom left:** At $T = 0.6$, the low-frequency wave has damped, leaving a mid-frequency wave (with period $2\pi/8$, higher frequency than the Ricker wavelet's preferred distance) of much lower amplitude (two orders of magnitude smaller), with only minute positional adjustments. **Bottom right:** At $T = 20$, the global potential has damped another order of magnitude, to 4×10^{-4}, leaving only the high-frequency spikes of individual Ricker wavelets (which have a "sharp" nondifferentiable corner as they wrap around $\pm\pi$). This "glassy" and distinctly nonuniform state appears to be stable, though it might only be extremely slow to evolve. 116

CHAPTER 1

Political Ideological Dynamics

1.1. Motivation

Accurate modeling of opinion dynamics has the potential to help us understand polarization and what makes effective political discourse possible or impossible. Here, we use physics-based methods to model the evolution of political opinions within a continuously distributed population. We utilize a network-free system of determining political influence and a local-attraction, distal-repulsion dynamic for reaction to perceived content. Our approach allows for the incorporation of intergroup bias such that messages from trusted in-group sources enjoy greater leeway than out-group ones. We are able to extrapolate these nonlinear microscopic dynamics to macroscopic population distributions by using probabilistic functions representing biased environments. The framework we put forward can reproduce real-world political distributions and experimentally observed dynamics, and is amenable to further refinement as more data becomes available.

1.2. Introduction

The field of opinion dynamics seeks to understand the evolution of ideas in populations, a complex interdisciplinary endeavor which has attracted a wide variety of approaches from different disciplines. After early mathematical groundwork [**5**], the growth of network science has led to a boom in models which utilize neighbor-based update rules to examine long-term outcomes for opinion distributions, such as polarization and

consensus [**6**–**19**]. Other researchers have advanced "sociophysics" approaches such as Ising [**20**, **21**], Sznajd [**22**, **23**], and generalized-kinetic models [**24**–**27**], which apply techniques from statistical physics to analyze analogous social systems [**28**]. Complementary to these modeling approaches, theoretical and empirical work from economics and social science has examined the political bias of media entities [**29**, **30**] and their influence on a population [**31**–**35**]. All these approaches contribute valuable insight toward an understanding of this complex topic, but the disparities between their perspectives make direct cohesion a challenge.

Our model takes a different approach, which we believe achieves the key benefits of previous models while expanding flexibility and retaining the ability to incorporate real-world data as it becomes available. One key structural choice we make is to modularize the process of opinion change by breaking it into two parts: perceptions and reactions.

In our model, individuals perceive a probabilistic mix of politicized experiences which depends on their ideology and party. This might be thought of as the continuum limit of a network approach, where influences are so numerous and varied that interactions are best characterized by a probability distribution rather than explicit neighboring agents. This approach also allows us to encapsulate broader societal influences such as politicized media environments, since individuals' perceptual mix may be constantly changing to reflect their changing worldview.

We model individuals' reactions to these perceptions by having their ideology evolve in continuous time. This is governed by ordinary and stochastic differential equations which depend on their current position and their perceptual distribution.

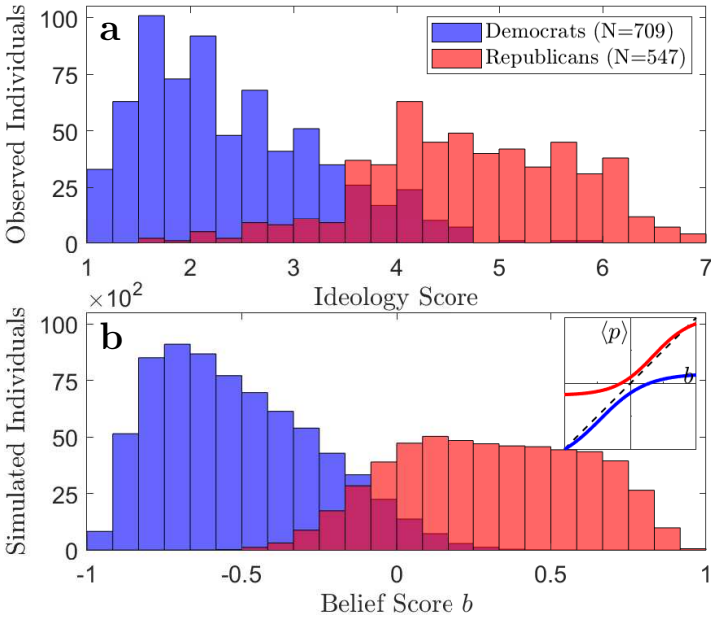

Figure 1.1. **(a) Empirical ideological distributions by U.S. political party.** Average ideological position score from 1 (strongly liberal) to 7 (strongly conservative) on social, economic, and military issues for 1256 U.S. Twitter users. Data from [**3**]. **(b) Model predictions.** Steady state for our simulated population of 70,900 Democrats and 54,700 Republicans, with party perception curves shown in the inset. See Results section for details.

Together, these perception and reaction modules capture a feedback loop between individuals' current beliefs, the biased "slice" of the political world they perceive, and how they update those beliefs as a result.

1.2.1. Political Spectrum

Like many prior approaches (e.g., [**3**, **6**, **7**, **14**, **17**, **29**, **32**, **33**, **36**, **37**]), we consider a single, finite ideology axis. Extensions to this are possible, as discussed in section 1.S.4, but the unidimensional approximation is supported by empirical results showing that the

liberal-conservative dimension captures the great majority of modern legislative behavior [**38**]. Figure 1.1(a) shows a one-dimensional projection of political ideology for the U.S. population based on one study [**3**]; though the precise methods of projecting the political landscape onto one axis differ between sources, other recent reports like that of Pew Research [**37**] show good qualitative agreement.

We will use the term *belief score*, b, to refer to an individual's ideological position between -1 (extreme liberal) and $+1$ (extreme conservative). We abstract all politically-opinionated information an individual is exposed to (hereafter termed *percepts*, p) onto this same axis, so that a percept of $p = +0.5$ is in support of belief score $+0.5$ (conservative), a percept with value $p = 0$ argues for a neutral stance, and so on. Due to the imprecise nature of any measurement on this scale (it's a projection of a highly abstract space that can be quantified in different ways), qualitative results should be robust to small changes in these values.

1.2.2. Opinion Change

Classic "bounded-confidence" models (e.g., [**6**, **7**]), which allow for individuals to interact only with others who are relatively like-minded, have been used to capture the effect of homophily on interaction. But political issues are contentious and are often brought up between those who disagree, and are easily suffused with negative emotional affect rather than agreement or indifference. Repulsion from disliked positions seems to be an important determinant in swing voters: a recent Pew survey [**39**] found that U.S. independents supporting one of the political parties did so mostly due to negative perceptions of the *other* party. So like some other extensions to bounded-confidence models (e.g., [**14**, **17**]),

we supplement local-attraction behavior with distal repulsion: individuals who are exposed to ideas which are too different from their own will not be attracted, but rather be *repelled* from the espoused position of the source. There is experimental evidence that this can be a very potent and real source of ideological movement: in recent work from Bail et al. [**3**], it was found that exposure to 24 tweets per day from a prominent member of the opposing party can have a significant repulsive effect over the course of a month, even among all other political inputs received by the participants (self-identified politically active Twitter users).

1.3. Methods

The first key component of our model is the *reaction function*. This is a continuous function which relates an individual's shift in ideological belief to the difference between a perceived political opinion (the percept, p) and the individual's own belief, b; we will refer to this difference $p - b$ as the *dissonance*. A repulsion effect will be modeled through the existence of a *repulsion distance* d such that percepts less dissonant than d will be attractive and percepts more dissonant than d will be repulsive. This parameter d can be allowed to vary depending on the context of the message, which will allow us to model the important effect of intergroup bias: for example, a somewhat challenging position can be repulsive when it comes from a disliked source but attractive when introduced by a member of one's in-group (see "Adding Intergroup Bias" below).

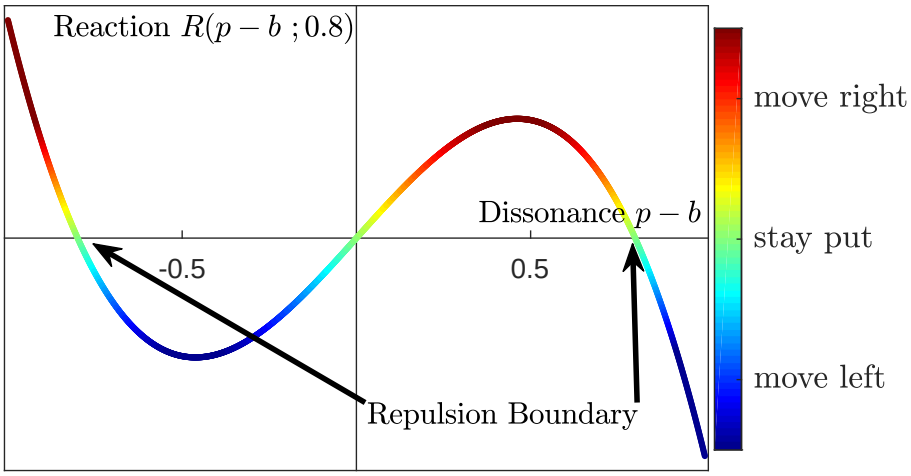

Figure 1.2. **Example reaction function.** Here we show a cubic reaction function, where an individual's reaction depends on dissonance $p-b$. Vertical scale has arbitrary units: the magnitude of this movement depends on time constant τ and current belief score b. For this image a repulsion distance of $d = 0.8$ was chosen.

One simple form for a reaction function that satisfies the above conditions employs a cubic dependence on dissonance:

$$R(p-b;d) = (p-b)\left[1 - \frac{(p-b)^2}{d^2}\right], \tag{1.1}$$

shown visually in Fig. 1.2.

To organically constrain belief dynamics to a bounded domain (in our case, $[-1,1]$), we temper the above reaction function with a multiplicative factor $(1-b^2)$. This has the effect of gradually damping motion near the extremes—thus we interpret the ± 1 boundaries of our finite ideology scale to be asymptotic extremes that are only approachable, not attainable. We also scale the dynamics by a time constant τ which controls the speed of belief change. Then, for an individual j with belief score b_j and repulsion distance d, exposed to percept p (which may depend on many factors), we arrive at the following

differential equation for ideological dynamics:

$$\tau \frac{\mathrm{d}b_j}{\mathrm{d}t} = (1 - b_j^2) \left\{ (p - b_j) \left[1 - \frac{(p - b_j)^2}{d^2} \right] \right\} . \tag{1.2}$$

1.3.1. Perceptual Diets

An important question remains: which individuals are exposed to which messages? The vast majority of work on opinion dynamics has been in a network context, wherein agents update their opinions according to a rule incorporating the positions of some other agent(s) (e.g., [**5**–**11**, **13**, **14**, **17**, **19**, **21**–**23**, **28**]). Our approach sidesteps the need for constructing explicit influence networks, which are difficult to capture due to the many modalities of human interaction. Instead we suppose that an individual's party affiliation and current political position determine their perceived "slice" of the political world—a probability distribution of political experiences, $\rho(p)$ [1]. This continuum approach allows us to personalize political environments to account for "media bubbles" and other biased environments even without a network, and is easily scaled to large populations.

1.3.2. Toy Models

1.3.2.1. Simplest Model. For the simplest concrete implementation of our framework, we might suppose a single-party population is initially distributed across the belief spectrum but is otherwise homogeneous, and that every individual perceives the same delta-distribution of political content, the constant percept $p = C$. Then upon choosing a

[1] Note that this is not necessarily inconsistent with a network approach; we believe a dynamical interaction network dependent on affiliation and political position could lead to a similar model.

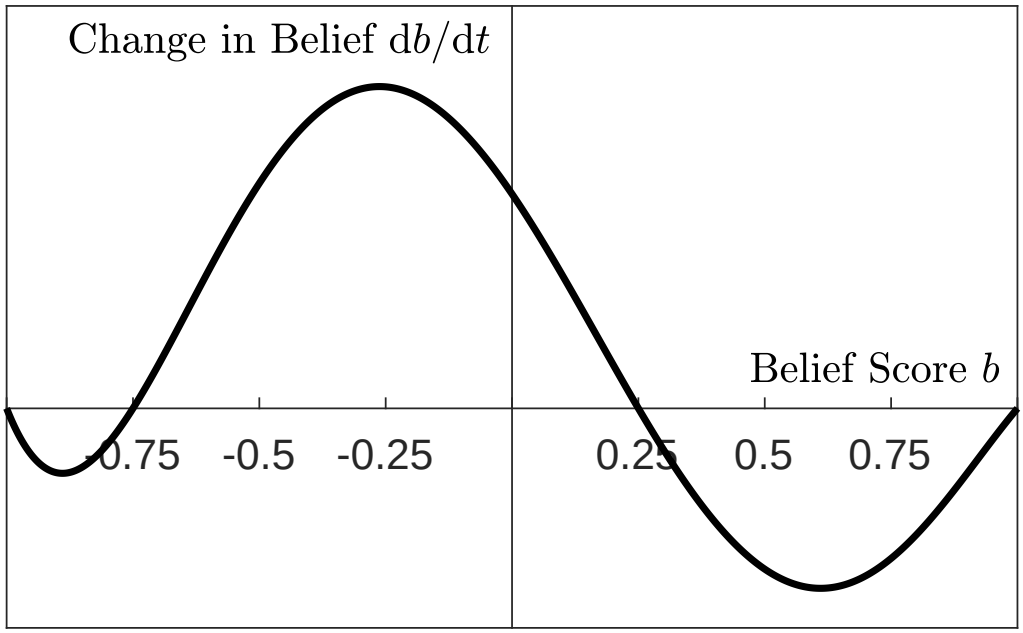

Figure 1.3. **Flow diagram.** Example of differential movement for a population uniformly exposed to a percept with score +0.25 assuming repulsion distance 1 (see Eq. (1.3)). Vertical axis scaling is arbitrary.

repulsion distance d we can exactly determine long-term behavior of the entire group—there will be a single flow function that affects the whole belief spectrum:

$$\tau \frac{\mathrm{d}b_j}{\mathrm{d}t} = (1 - b_j^2) \left\{ (C - b_j) \left[1 - \frac{(C - b_j)^2}{d^2} \right] \right\} . \tag{1.3}$$

This ordinary differential equation (ODE) has fixed points at $b_j = C$, $b_j = C \pm d$, and $b_j = \pm 1$ (due to the imposed domain bounds). The fixed point at $b_j = C$ is stable, and stability of the other points alternates.

For example, if we use the cubic reaction function from Fig. 1.2 above and set $d = 1$, $C = 0.25$, then that party's population experiences differential movement as shown in Fig. 1.3. Fixed points exist at $\{-1, -0.75, 0.25, 1, 1.25\}$ (though beliefs are constrained to the $[-1, 1]$ domain, so the theoretical fixed point at 1.25 is not meaningful). Given time,

all observers between -0.75 and 1 would congregate at 0.25, and all observers starting left of -0.75 would converge to -1. This small segment of the population—the members that are liberal enough to be repelled by the "party line"—might be likely to switch parties in favor of one with more comfortable percepts, though we don't include such party-switching dynamics in this initial model.

1.3.2.2. Adding Intergroup Bias. We would also like our modeling framework to accommodate the tendency for individuals to be more receptive to information from those whom they perceive as allies, i.e., part of their "in-group" [**40**]. For the simplest case, we modify our previous model by adding an "out-group" with its own distinct constant "party line" percept p_{o}. Now percepts have a party identity attached to them, and we allow individuals to consume a mixed diet of in-group and out-group information, at belief scores of p_{i} and p_{o}, respectively. We set repulsion distances d_{i} and d_{o} for in-group (e.g., U.S. Republican) and out-group (e.g., U.S Democrat) messengers, with $d_{\mathrm{o}} \leq d_{\mathrm{i}}$. We can set a fixed fraction f for in-party content, or allow for a belief-dependent skew $f(b)$ such that, e.g., liberal Republicans view a higher fraction of Democratic content than their conservative party-mates. The average flow function $\mathrm{d}b/\mathrm{d}t$ is then a simple weighted average of the flow functions in Eq. (1.2) due to each source:

$$\tau \frac{\mathrm{d}b}{\mathrm{d}t} = (1-b^2)\left[fR_{\mathrm{i}} + (1-f)R_{\mathrm{o}}\right] \ , \tag{1.4}$$

where in general $f = f(b)$, $R_{\mathrm{i}} = R(p_{\mathrm{i}} - b; d_{\mathrm{i}})$, and $R_{\mathrm{o}} = R(p_{\mathrm{o}} - b; d_{\mathrm{o}})$.

To understand the flow in this case, it is informative to consider the purely in-group and purely out-group situations ($f = 1$ or 0, respectively), because all fractional perceptual "diets" are interpolated between them (see Fig. 1.4). We note that exposure to some

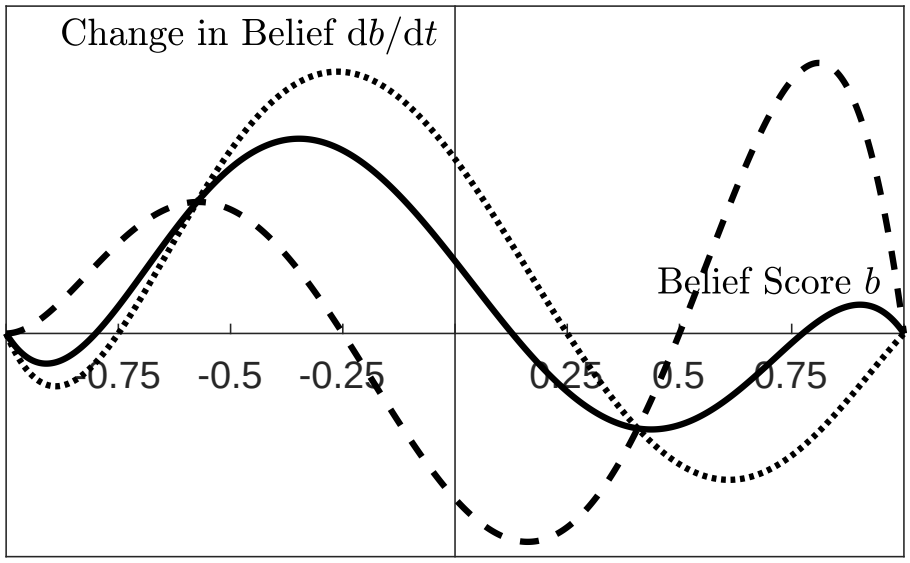

Figure 1.4. **Flow with different messengers.** The flow functions for in-group (dotted) and out-group (dashed) messages of $p_i = +0.25$ and $p_o = -0.25$ with repulsion distances of 1 and 0.75, respectively. The solid curve is the net flow if individuals are exposed to 70% in-group and 30% out-group percepts. Vertical axis scaling is arbitrary.

out-group content can in some cases *increase* polarization for a small extreme group—for example, in Fig. 1.4, individuals starting with $b > 0.75$ will on average move *rightward* when exposed to percepts from a 70%/30% combination of in-group and out-group sources, respectively (solid curve), whereas those same individuals would move *leftward* if presented with in-group information alone (dotted curve). This simple example shows how exposure to—and rejection of—opposing content can have a polarizing influence on a population.

Note that we assume that this "tribal" bias only affects the *reaction* to content, not its subjectively perceived ideological score p. However, the inclusion of such an additional bias effect is reasonable, and may be handled with a slight increase to model complexity (see section 1.S.4).

1.3.2.3. Adding Personalized Perceptions. Putting aside the in-group/out-group balance for a moment, we might expand our simplest model in a different way: by linking individuals' perceptions to their current beliefs via a "perception curve" $p(b)$, which indicates what content they see as a function of position. This reflects the differing "slices" of the political world that individuals see as a result of the differing environments and personal biases that accompany their ideologies.

In our simplest model, where $p = C$, the perception curve is a horizontal line in b vs p space; individuals at all b values perceive the same thing. In a hypothetical "perfectly targeted" world, the perception curve would be the 45° line $p = b$, and nobody would change belief because each person would perceive content perfectly in line with their current worldview.

Luckily, we don't need to privilege one such curve in particular—a graphical analysis method lets us combine *any* perception curve with the reaction function and read off a (qualitative) flow for each segment of the population. To do this, we plot the perception curve $p(b)$, and overlay the 45° line for reference—any time the perception curve intersects it, the individuals at that belief score are stationary, since their perceptions are in agreement with their current beliefs. If the perception curve is slightly above the 45° line, individuals with those beliefs are perceiving something slightly more conservative than their own views, and move right. Similarly, people move left wherever the perception curve is slightly below the 45° line.

We also overlay the repulsion boundaries at distance d above and below that $p = b$ line. If the perception curve exits the resulting "trust band" over some b interval, that

segment of the population is repelled and moves the opposite direction from what would be expected based on small deviations from the 45° line.

It is then straightforward to determine the qualitative behavior of the whole population given any perception curve $p(b)$ by visually examining intersections of the perception curve with the 45° lines, as in Fig. 1.5 (left panels). With a closed form expression for $p(b)$, we can use Eq. (1.2) to obtain an exact flow function (black curves on right panels of Fig. 1.5), and confirm our qualitative analysis. If multiple parties are present, this analysis is performed separately for each, and the resulting reactions are combined as in Eq. (1.4).

The real benefit of this graphical approach is its generality; one can draw any perception curve one would like and simply read off the fixed points and stability. Whenever the perception curve crosses the diagonal with slope less than one, that crossing becomes a stable fixed point. Whenever it crosses with a slope greater than one, the crossing becomes an unstable fixed point instead. If the perception curve crosses a repulsion boundary, shallow crossings create unstable points and steep crossings create stable ones.

While the choice of perception curve entails a large degree of modeling freedom, based on our graphical analysis reasoning we know our model's qualitative predictions aren't particularly sensitive to the choice. Ideally, real-world data could (and should) be used to construct such a curve (e.g., by evaluating the partisan positions of news sources and other political influences experienced by individuals across the political spectrum), though we leave this for future work (see section 1.S.5).

1.3.2.4. Adding Heterogeneity. To move toward a more realistic scenario, we must allow for heterogeneity of both environments and individuals. We can introduce random variation in two distinct components of the model: perceptions (so individuals are exposed

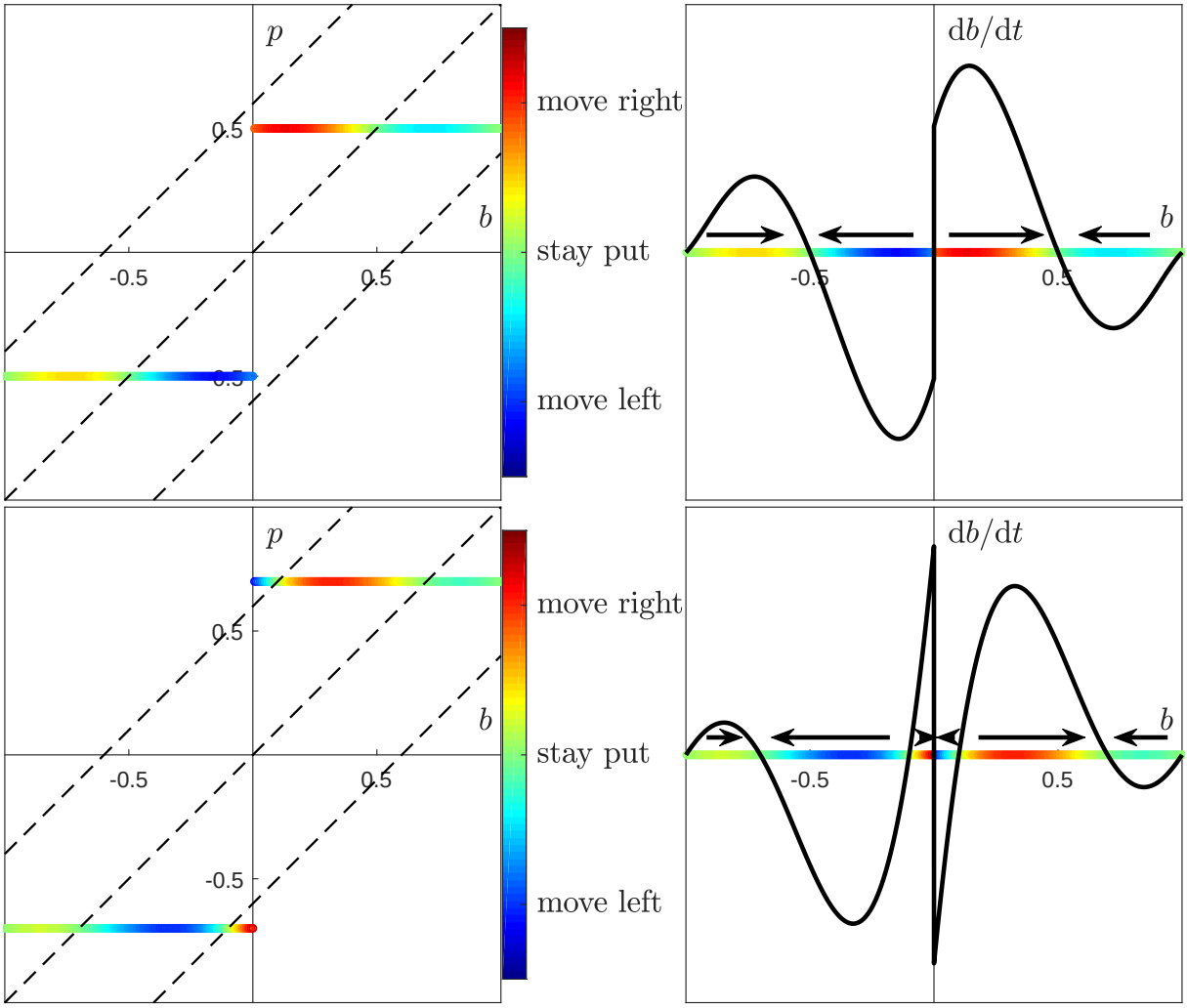

Figure 1.5. **Two-take world.** Graphical analysis of step-function perception curves. Left panels: perception curves color coded for the movement induced, along with dashed $p = b$ line and repulsion boundaries. Right panels: Projection of that flow-velocity color onto the belief axis, compared with the exact population flow calculated from Eq. (1.2) (black curve). Top row: When perception curves lie within the trust region, we see two attractors at the "party line" belief values. Bottom row: with more extreme "party lines," centrists are repelled by either party position, creating a stable central attractor.

to a range of different inputs rather than a single determined value), and the reaction function (so otherwise identical individuals can react differently to the same percept).

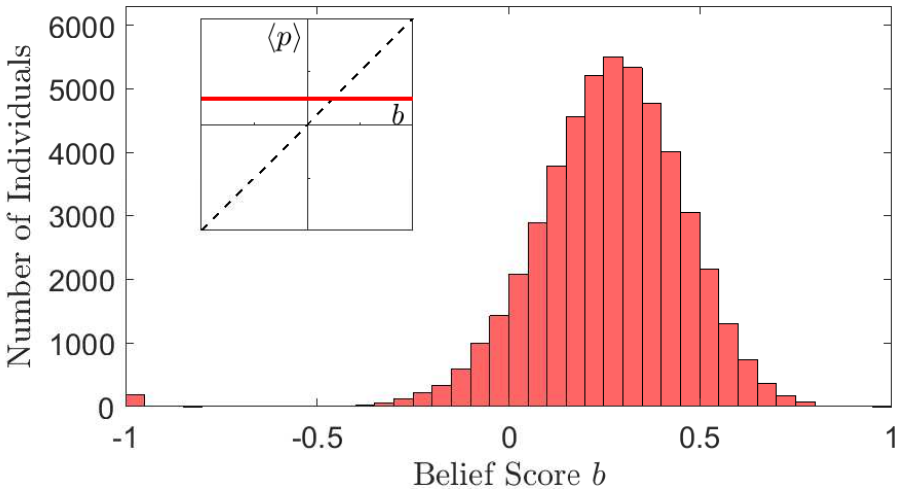

Figure 1.6. **Simulated population distribution.** The stable population state induced by flow function Eq. (1.3) with added Gaussian noise ($\tau = 1$, $dt = 0.001$, $\sigma = 0.25$, $N = 50,000$). Population was initialized to match Republicans from Bail [**3**]. Inset: Perception curve, the constant $C = 0.25$. All variation is in reaction.

For the latter, we add Gaussian noise to the reaction function R, which causes the stable fixed points from our prior analysis to expand into finite-width stable distributions; these may be estimated easily and accurately by Euler-Maruyama numerical integration of our now-stochastic differential equation (SDE). For example, with the conditions in Fig. 1.6, the main body of the party congregates around the primary attractor at 0.25, and a small group is repelled to -1 [2].

If we wish to add variability to the percept instead of the reaction, nonlinear effects become more important, since p—now properly a probability distribution $\rho(p)$—must be fed through reaction function $R(p - b)$ before its effects are determined. This means the net effect of the perceptual diet is a weighted average over all possible percepts, which for smooth percept distributions becomes an integral of $R(p - b)$ against $\rho(p)$. Due to the

[2]In cases like this with multiple attracting "camps" without significant overlap, the long-term populations of each camp may depend on initial conditions.

asymmetry of the reaction function across the repulsion boundary—repulsion as modeled above is stronger than attraction—a symmetric distribution of percepts centered at the boundary will have a net repulsive effect. Thus, if the perception curve $p(b)$ represents the peak of this distribution, symmetrically broadening that distribution effectively *narrows* the trust region. Regardless of the shape of perception distribution, we can still use our graphical analysis technique to solve for net opinion drift, though the repulsion boundaries may warp, as we show in section 1.S.1.

1.3.2.5. Full Model. Taking all these effects together, the model has the following structure:

$$R(p-b;d) = (p-b)\left[1 - \frac{(p-b)^2}{d^2}\right] \tag{1.5a}$$

$$v_{in} = \int_{-1}^{1} R(p-b;d_{in})\ \rho_{in}(p;b,\sigma_p)\mathrm{d}p \tag{1.5b}$$

$$v_{out} = \int_{-1}^{1} R(p-b;d_{out})\ \rho_{out}(p;b,\sigma_p)\mathrm{d}p \tag{1.5c}$$

$$\tau\ \mathrm{d}b = (1-b^2)\left\{[fv_{in} + (1-f)v_{out}]\,\mathrm{d}t + \sigma_r \mathrm{d}W\right\} \tag{1.5d}$$

with ρ_{in} and ρ_{out} as the perceptual distributions for in-group and out-group content respectively, and v_{in} and v_{out} the opinion drift due to those influences.

1.4. Results

When we put together all the modeled effects described above, we find robust realistic distributions at equilibrium (see Fig. 1.1(b)). We used simple sigmoid perception curves (shown in the inset to Fig. 1.1(b), details in section 1.S.3)for the peaks of perceptual diets (beta distributions with standard deviation $\sigma_p = 0.2$), and noisy reactions (standard

deviation $\sigma_r = 0.15$), along with simple linear fractional content ratios

$$f_D = 0.7 + 0.2b \,, \tag{1.6a}$$

$$f_R = 0.7 - 0.2b \tag{1.6b}$$

for Democrats and Republicans, respectively, to emulate a "media bubble" effect. This model's steady state shows good agreement with real-world distributions of U.S. political ideology from Bail et al. [**3**] and Pew Research [**37**]—see Fig. 1.1. For easy comparison with real data, Fig. 1.1(b) shows a simulation of one hundred times Bail et al.'s experimental population: 70,900 Democrats and 54,700 Republicans. In this comparison, we must note that our belief scale is not identical to theirs; ± 1 on our scale are asymptotically extreme, whereas 1 and 7 on Bail et al.'s scale are attainable and signify strong agreement on all surveyed issues.

We can also replicate the experiment of Bail et al. in silico: starting with a population at equilibrium (shown in Fig. 1.1(b)), and artificially inducing counter-attitudinal Democratic content to Republican experimental subjects (a distribution peaked at $p = -0.75$, weighted as if it consisted of 24 percepts on top of a presumed diet of 100 percepts per day) over the course of 30 "days," causes the mean position of those subjects to shift rightwards by a little less than half its natural standard deviation (from 0.30 to 0.42, stdev $\sigma \approx 0.3$). This matches the findings of Bail et al., who found average rightward movement of 0.6 points on a 1-to-7 scale, which represented between 0.11 and 0.59 standard deviations ($p < 0.01$) [**3**]. Implementation details can be found in section 1.S.3.

1.5. Discussion

We have put forward a modeling framework for individual political opinion drift which separates perceived content and the reaction of the viewer to that content, in order to separately model perceptual filtering, the shift from attraction to repulsion for dissonant content, and the effect of intergroup bias. We have presented toy models to elucidate each effect on its own in the absence of noise, and introduced a graphical analysis technique for qualitative analysis of behavior under general belief-dependent perception curves. With the inclusion of additive noise, analytically determined fixed points widen into stable distributions.

With all these effects included and some simple parameter assumptions, we showed that population distributions matching recent survey data emerge naturally. Furthermore, we were able to simulate the experiment of Bail et al. [**3**] and found similar outcomes.

Our approach allows for modeling of important psychological effects such as self-serving bias (perception curves are increasing functions of b) and intergroup bias (repulsion distance depends on source) without requiring a network. This frees future data-gathering efforts from the often challenging task of network tie construction, and allows for easy simulation of very large populations.

In order to approach this topic, we have made considerable simplifications, and it is easy to imagine extensions which might increase the realism of this model (as we discuss in section 1.S.4).We have intentionally chosen a relatively simple structure which is nonetheless able to capture psychological tendencies for repulsion and tribalism, and couple them to a politicized environment, while preserving mathematical tractability. A paucity of available data has forced us to make assumptions on functional forms and parameter

values. While these are reasonable placeholders, they can be modified or replaced as empirical data become available; it isn't hard to imagine experiments which might elucidate qualitative and quantitative effects of interest (see section 1.S.5 and Section 1.E).We hope this endeavor leads to a new sort of data-driven political modeling to better understand human behavior, polarization, and strategies for effective political dialogue.

1.S. Additional Mathematical Analysis

1.S.1. Perception Distributions

As we mention in the "adding heterogeneity" section of the previous section, if our model is to have any claim at accurately modeling the political lives of real people, it must allow individuals to consume not just a single, constant percept $p(b)$ but rather a whole distribution of content, $\rho(p; b, \sigma_p)$. In this case, instead of using the single p value to determine an individual's reaction, we calculate their weighted-average reaction by integrating the probability distribution of percepts they might receive multiplied by the reaction those percepts would cause. We note that our cubic reaction function is asymmetric across the repulsion boundary (it's steeper outside the boundary than inside, so repulsion is "stronger" than attraction). Thus, if individuals receive a distribution of percepts centered at their "perception curve" value $p(b)$, a symmetric widening of their experiences has the *asymmetric* effect of shifting the system's fixed points: since it takes fewer repulsive events than attractive ones to maintain net-zero movement, the fixed point occurs when the center of the perceptual distribution is still in the trust region. In other words, the repulsion boundary is effectively narrowed with regard to the peak percept value $p(b)$.

The precise effects of this perceptual variety depend on the shape of the perceptual distribution and the choice of reaction function. First we'll consider Gaussian-distributed percepts centered on the "perception curve" value $p(b)$, and the cubic reaction function from Eq. (1) of the main text, $(p-b)[1-(p-b)^2/d^2]$. These choices are convenient in that the integral for average belief change is analytically tractable. For clarity, we change variables to "average dissonance" $\mu = p(b) - b$, and let x be the dummy variable of integration for possible dissonance. An approximate version of this integral, with infinite limits of integration (so that many terms drop out), is:

$$\begin{aligned}\tau \left\langle \frac{\mathrm{d}b}{\mathrm{d}t} \right\rangle &= \left(1-b^2\right) \int_{-\infty}^{+\infty} \underbrace{x\left(1-\frac{x^2}{d^2}\right)}_{R(x)} \underbrace{\left[\frac{1}{\sqrt{2\pi}\sigma_p} e^{-\frac{(x-\mu)^2}{2\sigma_p^2}}\right]}_{\rho(x;b,\sigma_p)} \mathrm{d}x \\ &= \left(1-b^2\right)\ \mu\left[\frac{(d^2-3\sigma_p^2)}{d^2} - \frac{\mu^2}{d^2}\right] . \qquad (1.7)\end{aligned}$$

We see that $d^2 - 3\sigma_p^2$ plays the role that d^2 played before, setting the non-origin zeros of the cubic; when μ^2 is greater than this value, the average movement of the individual is *away* from the peak percept. There is also a critical variance $\sigma_c^2 = d^2/3$ at which the system undergoes a pitchfork bifurcation. For $\sigma_p > \sigma_c$ the bracketed term in Eq. (1.7) is always negative, i.e., the net change in belief is always *contrary to* the average media perceived. See Figure 1.S7.

These distribution widths are not unrealistically large; as seen in Fig. 1.S7, for a repulsion distance of 0.8 the standard deviation needs only be 0.46 for the overall effect of a content distribution to be repulsive (i.e. causing movement away from that distribution's mean). Thus, especially for out-group content with a naturally narrower repulsion

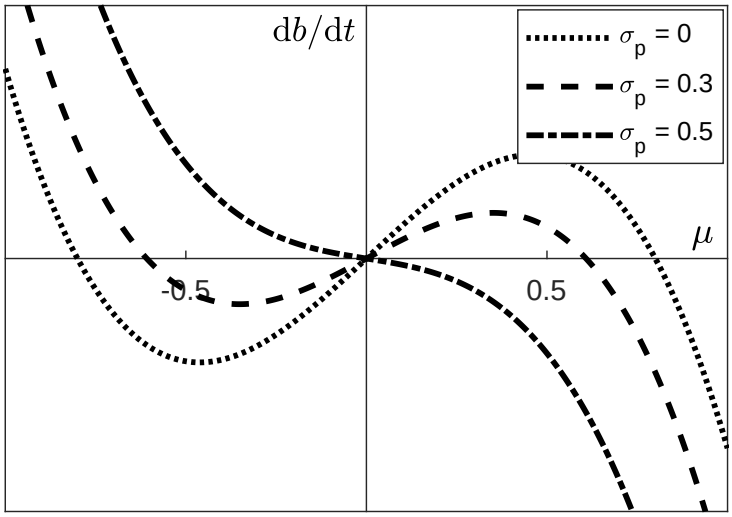

Figure 1.S7. **Effect of perception distribution width on reaction.** Net change in belief $\mathrm{d}b/\mathrm{d}t$ versus expected value of dissonance μ for varying levels of perception distribution width, from Eq. (1.7) with $d = 0.8$. The critical standard deviation for $d = 0.8$ is $\sigma_c = 0.8/\sqrt{3} \approx 0.46$.

distance, viewing a wider distribution of that content can actually cause repulsion, since the extreme percepts will repel the viewer more than the moderate percepts will attract them.

To visualize the effects of normally distributed perceptual distributions $\rho(p; b, \sigma_p)$ replacing deterministic percepts $p(b)$, we can examine density plots for the net movement for all combinations of b and p (repulsion distance $d = 0.8$): see Fig. 1.S8. This is the space that our graphical analysis technique utilizes: if we establish a perception curve $p(b)$, the values of this map that the curve crosses are the realized average movement for each part of the population.

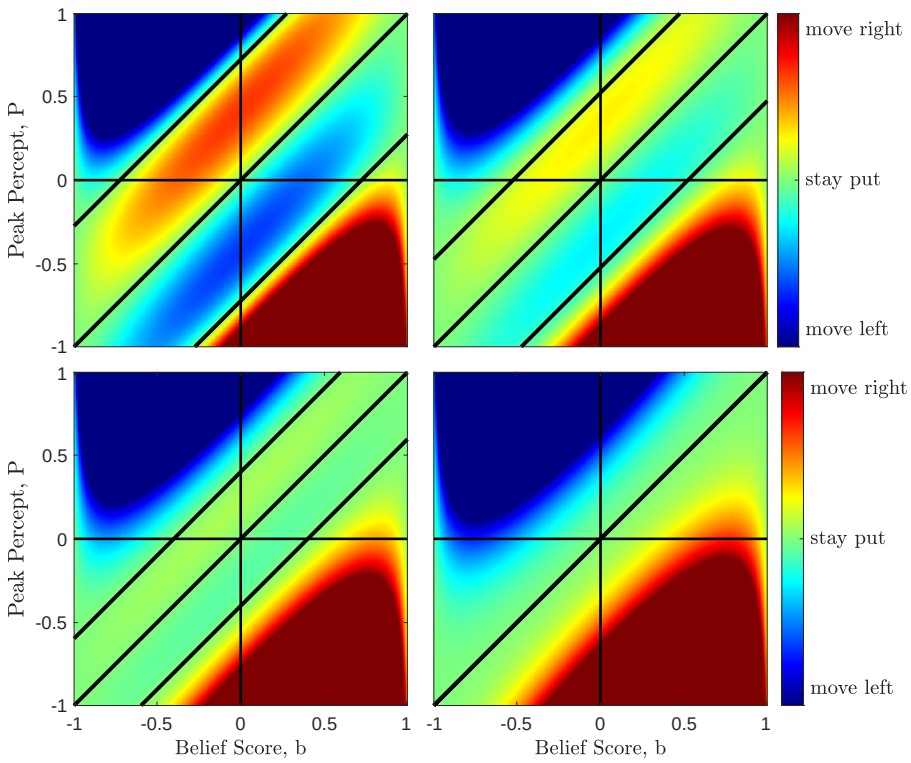

Figure 1.S8. **Reaction map for normally distributed diets.** Average movement caused by normally distributed perceptual diets with peak p, for individuals at belief score b, and repulsion distance $d = 0.8$. Results shown for $\sigma_p = 0.2$ (top left), 0.3 (top right), 0.4 (bottom left), and 0.5 (bottom right).

1.S.1.A. Bounded Percepts: Truncated Gaussian. In deriving Eq. 1.7 we approximated by integrating over the entire real line for dissonance when it should be constrained to the range allowed by percepts in $[-1, 1]$—that is, from dissonance $x = -1 - b$ to $1 - b$. That makes the result somewhat more complicated (note: lacking symmetry around b, we don't utilize the μ substitution, and x represents percept value instead of dissonance):

$$\tau \left\langle \frac{\mathrm{d}b}{\mathrm{d}t} \right\rangle = (1 - b^2) \int_{-1}^{1} \left[\frac{A}{\sqrt{2\pi}\sigma_p} e^{-\frac{(x-P)^2}{2\sigma_p^2}} \right] \left\{ (x - b) \left[1 - \frac{(x - b)^2}{d^2} \right] \right\} \mathrm{d}x$$

$$= A\frac{(1-b^2)\,\sigma_p}{d^2\sqrt{2\pi}}\Bigg\{ \left[1-d^2+2\sigma_p^2+P^2-3Pb+2b^2\right]\left[e^{\frac{-(-1+P)^2}{2\sigma_p^2}}-e^{\frac{-(1+P)^2}{2\sigma_p^2}}\right] + [P-3b]\left[e^{\frac{-(-1+P)^2}{2\sigma_p^2}}+e^{\frac{-(1+P)^2}{2\sigma_p^2}}\right]\Bigg\}$$

$$+\frac{(1-b^2)\,(P-b)}{2d^2}\left\{d^2-3\sigma_p^2-[P-b]^2\right\}\left[\mathrm{Erf}\left(\frac{1+P}{\sqrt{2}\sigma_p}\right)+\mathrm{Erf}\left(\frac{-1+P}{\sqrt{2}\sigma_p}\right)\right]. \tag{1.8}$$

using shorthand $P = p(b)$ for compactness. A is a normalization factor depending on b and σ_p needed to make the truncated Gaussian integrate to 1:

$$A = \frac{1}{\frac{1}{\sqrt{2\pi}\sigma_p}\int_{-1}^{1} e^{\frac{-(x-P)^2}{2\sigma_p^2}}\,\mathrm{d}x} = \frac{2}{\left[\mathrm{Erf}\left(\frac{1+P}{\sqrt{2}\sigma_p}\right)-\mathrm{Erf}\left(\frac{-1+P}{\sqrt{2}\sigma_p}\right)\right]}$$

Fig. 1.S9 shows the reaction map for these truncated-normal diets, computed analytically at each b and p combination.

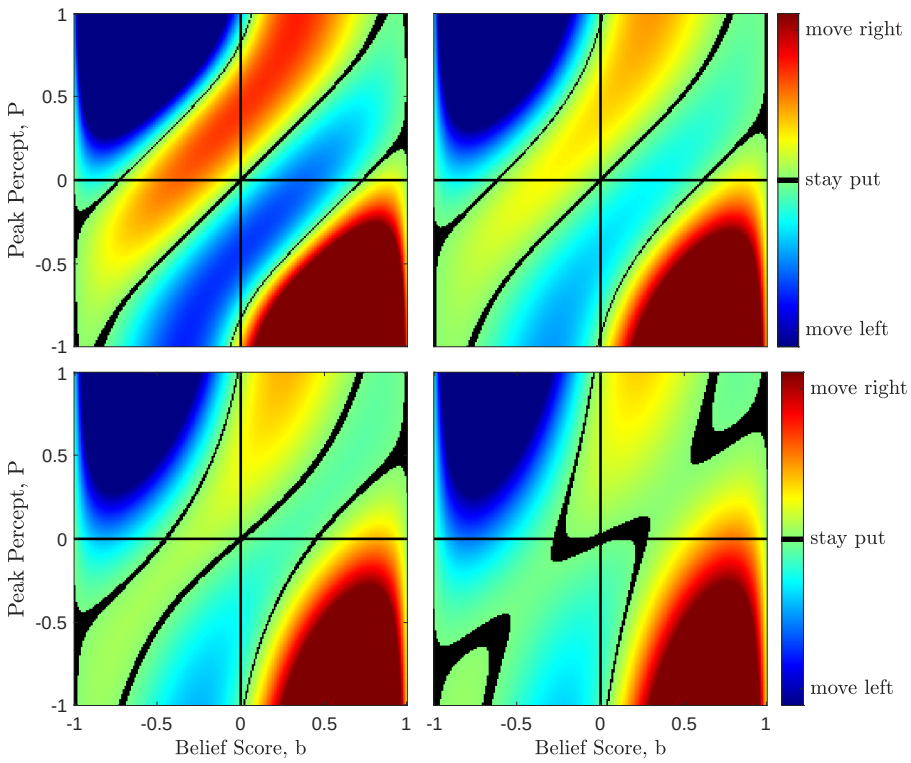

Figure 1.S9. **Reaction map for truncated-normal diets.** Expected movement caused by truncated-normal perceptual diets with peak p (vertical axis), for individuals at belief score b (horizontal axis), with repulsion distance $d = 0.8$. Results shown for $\sigma_p = 0.2$ (top left), 0.3 (top right), 0.4 (bottom left), and 0.5 (bottom right).

1.S.1.B. Bounded Percepts: Beta Distributions. For our simulations, we bounded perceptual diets in a more natural way, by utilizing beta distributions stretched to fit $[-1, 1]$. These distributions approach zero at the boundaries of our domain, fitting our asymptotic-extremes interpretation of this axis. The beta distribution with our endpoints has the equation

$$\text{Beta}_{[-1,1]}(x; \alpha, \beta) = 4\frac{(1+x)^{\alpha-1}(1-x)^{\beta-1}}{2^{\alpha+\beta}}\frac{\Gamma(\alpha+\beta)}{\Gamma(\alpha)\Gamma(\beta)}\,, \tag{1.9}$$

where α and β are parameters of the distribution and Γ is the gamma function.

We can construct a distribution to have any desired mode (peak) $p(b)$ and standard deviation σ_p by solving the implicit equations

$$\text{mode } = p = \frac{\alpha - \beta}{\alpha + \beta - 2} \tag{1.10}$$

$$\text{variance } = \sigma_p^2 = \frac{4\alpha\beta}{(\alpha + \beta)^2(\alpha + \beta + 1)} \tag{1.11}$$

for $\alpha, \beta > 1$ in terms of p and σ. Examples are shown in Fig. 1.S10.

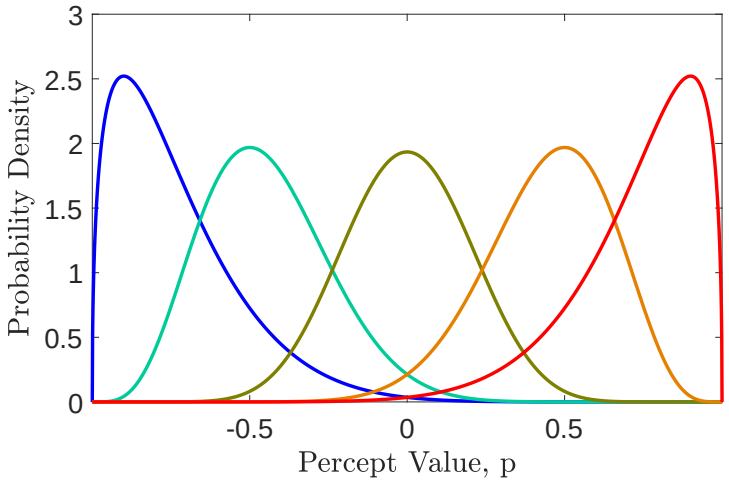

Figure 1.S10. **Beta-distributed diets.** Examples of beta distributions with peaks at $-0.9, -0.5$, 0, 0.5, and 0.9. All have the same standard deviation, $\sigma_p = 0.2$.

Unfortunately, when using these beta distributions, the weighting integrals with our cubic reaction function aren't possible to evaluate in closed form. However, we may numerically compute these integrals for a finite grid of p and b values at any chosen standard deviation to visualize the reaction space. In Fig. 1.S11, we can see the repulsion boundaries bending and bifurcating as σ_p increases.

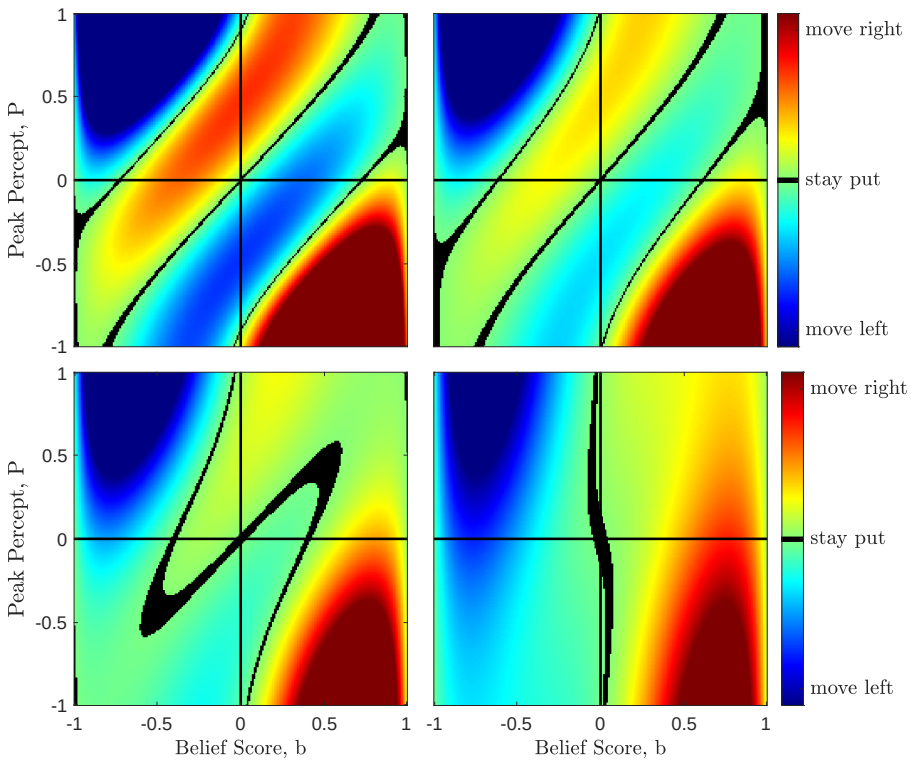

Figure 1.S11. **Reaction map for beta-distributed diets.** Average movement caused by beta-distributed perceptual diets with peak p, for individuals at belief score b, and repulsion distance $d = 0.8$. Results shown for $\sigma_p = 0.2$ (top left), 0.3 (top right), 0.4 (bottom left), and 0.5 (bottom right).

Computing a reaction map like 1.S8, 1.S9 or 1.S11 allows us to use our graphical analysis technique with *any* perception curve, to get a sense of average population drift for the whole political spectrum.

1.S.2. Stochastic Differential Equation Details

For the "realistic" simulation shown in Fig. 1 of the main text, we used beta-distributed perceptual diets with constant standard deviation σ_p. Party perception curves $p_D(b)$ and $p_R(b)$ determine the peaks of these distributions, so that individuals see in-group and

out-group content distributions $\rho_{in}(p; b, \sigma_p)$ and $\rho_{out}(p; b, \sigma_p)$. The average effect of each distribution is the integral against the reaction such content would cause (i.e., Eqs. (1.13) and (1.14)). Each group's effect on the observer is weighted by its content fraction, then the stochastic reaction-noise term is added before all movement is edge-damped, leaving us with Eq. (1.15).

$$R(p-b;d) = (p-b)\left[1 - \frac{(p-b)^2}{d^2}\right] \tag{1.12}$$

$$v_{in} = \int_{-1}^{1} R(p-b;d_{in})\ \rho_{in}(p;b,\sigma_p)\mathrm{d}p \tag{1.13}$$

$$v_{out} = \int_{-1}^{1} R(p-b;d_{out})\ \rho_{out}(p;b,\sigma_p)\mathrm{d}p \tag{1.14}$$

$$\tau\ \mathrm{d}b = (1-b^2)\left\{[fv_{in} + (1-f)v_{out}]\,\mathrm{d}t + \sigma_r \mathrm{d}W\right\} \tag{1.15}$$

This can be made computationally feasible by discretizing the b and p domains (e.g., to the nearest hundredth) and computing the integrals v_{in} and v_{out} at each possible combination—as was done for Figs. 1.S9 and 1.S11, which show v_{out} for different σ_p values. Then in iteration, we simply reference the nearest-case pre-computed value (nearest-neighbor interpolation) rather than computing each individual's weighting integral at each time-step.

1.S.3. Implementation Details

Our "realistic" simulation shown in Fig. 1.1b initialized the population's starting beliefs to uniform random values in $[-1, 1]$ for both parties. The sigmoid perception curves (shown

in Fig. 1.1b inset) used were:

$$\text{Republicans: } p_R(b) = 0.6 \tanh\left[\frac{1.05}{0.6}(b - 0.35)\right] + 0.42, \text{ and}$$
$$\text{Democrats: } p_D(b) = 0.7 \tanh\left[\frac{1.00}{0.7}(b + 0.46)\right] - 0.55 \,,$$

arrived at by rough visual fitting of results to empirical target distributions. Parameter values were:

$$d_i = 1.3,\ d_o = 0.8,\ \sigma_p = 0.2,\ \sigma_r = 0.15 \,.$$

In-group fraction scaled linearly and symmetrically from 0.5 (for $b = +1$ Democrats and $b = -1$ Republicans) to 0.9 (for $b = -1$ Democrats and $b = +1$ Republicans):

$$f_D(b) = 0.7 + 0.2b,$$
$$f_R(b) = 0.7 - 0.2b \,.$$

Equations (1.12), (1.13), (1.14), (1.15) determined population movement over time, utilizing Euler-Maruyama numerical integration. For finding equilibria, the time constant $\tau = 1$ was used.

We note that, in fitting the model's results via the 8 sigmoid parameters, the equilibrium distributions were particularly sensitive to the most-repulsive tails of these curves: cross-party content seen by the more-extreme sections of the spectrum (e.g., the left tail of the Republican-content curve powerfully affected the left edge of the Democrat distribution, and vice-versa). This sensitivity would be significantly reduced in a scenario with saturating repulsion, which we would expect to find from data, but it is the main reason for the parameters being fit to the hundredths place in section 1.4.

For simulation of Bail's experiment, the population was initialized at its equilibrium, but in addition to v_{in} and v_{out} there was a third influence v_{bot} based on an out-group distribution peaked at value $p = -0.75$ shown to Republicans and $p = 0.3$ shown to Democrats, to roughly match the other party's distribution. This extra out-group effect was weighted as if it were 24 additional percepts on top of a 100-percept daily diet, i.e., with weight $f_{bot} = 24/124$. So Eq. (1.15) becomes

$$\tau \, \mathrm{d}b = (1 - b^2) \left\{ [(1 - f_{bot})(f v_{in} + (1 - f) v_{out}) + f_{bot} v_{bot}] \, \mathrm{d}t + \sigma_r \mathrm{d}W \right\} . \tag{1.16}$$

Under this assumption, the time constant $\tau = 30$ caused movement in agreement with Bail et al. [**3**]: slight leftward movement of Democrat mean from -0.51 to -0.53 (about 6% of its natural standard deviation), but significant rightward movement of the Republican mean from 0.30 to 0.42 (about 40% of its natural standard deviation).

All code utilized is available upon request.

1.S.4. Some additional extensions

One simple extension is the addition of more groups/parties, such as independent/unaligned individuals and messages. This would require another perception curve, and a three- or more-way fractional content breakdown instead of the single in-group fraction $f(b)$ as our analysis used.

Additional affiliations such as religion, race, regional identity, etc., may be added to the model without change to the framework. These affiliations would appear as labels that affect the perception curve(s)—since affiliations can change what individuals are exposed to—and inter-group bias, since identity can affect how one reacts to others' opinions

and identity. In particular, the repulsion distance d, representing "trust," "credulity," or "benefit of the doubt," can depend on each affiliation of the individual and of the messenger to allow for more intricate inter-group prejudices than just in-party and out-of-party trust levels. One could also add noise to d values to model individual variation in level of credulity towards other groups. However, given the difficulty of measuring inter-group trust levels, we chose to avoid over-fitting by only utilizing party affiliation in our simulations.

One might also generalize this model to multiple dimensions: instead of a scalar belief value b, an n-dimensional vector $\mathbf{b}$ would represent an individual's beliefs with respect to each of n issue axes. Percepts would engage with one or more of these issues. Lacking relevant data, we do not put forward assumptions on how reaction dynamics might be coupled; one might assume that dynamics along each axis would be largely independent of one another, since position on one issue rarely affects position on another directly. However, it is possible that the dynamics along multiple axes would be coupled by tribalism; being repelled from a message might drive an individual closer to the opposing camp on more axes than just the one being engaged with, as the individual identifies more strongly with the whole opposing party.

One might also suggest that individuals perceive a more extreme version of the other party as they become more extreme themselves. This would require additional perception curves for out-group content rather than re-using the same curve for both parties—in particular, the curves that determine out-group content might be *decreasing* with belief instead of increasing. The large dissonance numbers in this case would likely require a different reaction function—one in which repulsion saturates—since repulsion quickly

dwarfs attraction under our cubic function. As an additional bonus, these new cross-party perception curves could incorporate partisan *interpretation* bias (as well as reaction bias narrowing the repulsion distance), such that even the *same* statement could be given a different subjective ideological rating (p value) when individuals believe it comes from an out-party source.

Another potential extension would be the addition of mechanisms by which the perception curves change over time. Time-dependence could be introduced to investigate hypotheses about the impact of changing media environments, or perception curves might evolve in response to the population state. The latter option would provide a form of indirect coupling between modeled individuals.

1.S.5. Further Work

The modular structure of our framework is amenable to the incorporation of further data, replacing idealized functions and parameters with empirical distributions from surveys and experiments. For example, to refine the reaction function, further experiments like that of Bail et al. [**3**] might investigate the impact of political opinions on individuals, and how the messenger's apparent identity affects the reception of dissonant ideas. As for perceptual environments, the non-network approach means that data collection can focus on averages and distributions rather than influence-network properties and tie reconstruction. Perceptual diets might be estimated from the top down: each media outlet (or other notable source of political influence) might be assigned an ideology score (as others have done, see, e.g., [**29**, **30**, **33**, **41**]), and surveys or viewership data could determine which content is consumed in what proportion by each part of the ideological spectrum.

Alternately, self-report of political influences and their positions could produce estimates of perceptual diets which also account for interpretation bias—the same content might be interpreted differently by different observers.

Regardless of the approach, any such data-driven realization of this framework will possess greater validity and predictive power as more data is collected. We hope that this modeling framework will afford a better understanding of individual and population-level opinion dynamics, and the feedback effects due to personalized political environments.

1.E. Design for Experimental Refinement

This model was designed with the philosophy of admitting realistically-attainable data, and I have designed an experiment which will provide a good deal of it. As the model currently stands, the main areas to be elucidated are:

- The reaction function: how do individuals update their ideological beliefs in response to political percepts, based on their current ideology, the percept's ideology, and party affiliation of each?
- The perception curves: how does the political information ecosystem distribute information to each part of the ideological spectrum, from each party to each party?

But the issue of subjectivity of these ideology-score ratings requires some care, including:

- How consistent are individuals' self-reported ideological positions?
- How do different individuals rate identical percepts?
- How does party affiliation bias those ratings?

In order to address as many of these outstanding questions with as simple an experiment as possible, I have begun constructing a survey to be distributed on the Mechanical Turk platform with the following structure:

(1) Participants are randomly divided into control and treatment groups. This will determine whether their percepts are marked with a speaker's party affiliation or not, to experimentally examine the effect of intergroup bias.

(2) Individuals rate their own overall political position on a liberal-conservative axis as well as where they stand on that same axis on individual issues. Participants also provide their own political party affiliation.

- This will allow us to compare the agreement of overall self-identification with an average of self-reported positions on individual issues.

(3) Participants are shown a batch of political statements, asked to rate their ideological position, and asked to rate their positive/negative sentiment about the statement.

- Ideally we would measure real ideological shift, but for an initial experiment we choose to use sentiment as a proxy. Finding this "sentiment curve" (as opposed to the reaction curve) may in fact have direct practical value for its own sake, for things like political messaging campaigns which are more focused on immediate sentiment than actual incremental ideology shift.

(4) Participants will also be asked to estimate the frequency that they are exposed to political content from each part of the political spectrum.

The data from this will be compared to extract:

- The ideological rating distributions for individual statements.

- The effect of visible party affiliation on statements' ideological rating distributions by participants.
- The "sentiment curve" from the cloud of points produced by participants' sentiment ratings and the ideological dissonance $p - b$ each participant reported to cause that rating. Alternate hypotheses may be explored at this stage, for example de-coupling p and b by viewing the points in (b, p, s) space to see if dissonance is actually a meaningful/useful invariant across the population. From this sentiment curve, an empirical *reaction* curve may be estimated as dissonance times the sentiment curve.
- Sentiment curves for each party viewing unmarked, same-party, or opposite-party content. This will interrogate the hypotheses that (a) intergroup bias is consistent and (b) party affiliation influences sentiment (and by proxy reaction) *separately* from its effect on perception bias (the influence of speaker's apparent party affiliation on the ideology-score ratings given by observers).
- An approximation for perception curves (or perception surfaces) describing exposure of each part of the political spectrum to each other part. This will allow us to interrogate the number of perception curves, and the accuracy of Beta distributions as a model for political information diets.

CHAPTER 2

Handling Nonlinear Stochasticity

2.1. Introduction

Many real-world systems exhibit noisy evolution; interpreting their finite-time behavior as arising from continuous-time processes (in the Itô, Stratonovich, or Hänggi-Klimontovich sense) has led to significant success in modeling and analysis in a variety of fields. Here we examine a previously overlooked class of differential equations where evolution depends nonlinearly on a random or effectively-random quantity. We put forward a method for converting these ambiguous equations into equivalent Itô processes, which may be of great utility for their numerical simulation and theoretical analysis. In particular, we show that this technique provides distinct predictions for the velocity distribution of a particle experiencing quadratic drag amidst turbulence, and for a simpler cubic-drag analogue. We also develop an equilibrium-moment relation for examining the equilibria of Itô attractors, which may provide information when exact solutions are unavailable. We use this technique to extract previously unattainable information about one of our example systems' equilibrium. This work enables the theoretical and numerical examination of a wide class of mathematical models which might otherwise be oversimplified due to a lack of appropriate tools.

2.2. Generalizing Langevin Equations

Langevin equations are often used to represent theoretical differential behavior for systems exhibiting stochastic dynamics (see, e.g., [**42**, **43**]). These equations have a standard form, which we will aim to generalize:

$$\frac{\mathrm{d}x}{\mathrm{d}t} = f(x,t) + g(x,t)\eta_t \,,$$

where η_t represents the "Gaussian white noise" term, δ-correlated in continuous time. If $g(x,t)$ exhibits x dependence, such Langevin equations are ill-defined, necessitating an Itô, Stratonovich, or Hänggi-Klimontovich interpretation [**43**–**45**]. These will differ in their "drift" behavior, but may be converted between one another in a straightforward manner.

Here, we seek to generalize to systems of the form

$$\frac{\mathrm{d}x}{\mathrm{d}t} = R(x,t,\eta_t). \tag{2.1}$$

We argue that, with the proper conversion procedure based on the central limit theorem [**46**], these Langevin-type systems may be reduced to equivalent Itô behavior, allowing for consistent simulation and theoretical analysis.

As a motivating example, we start by highlighting the difference between two similar-looking Langevin-type equations:

$$\frac{\mathrm{d}x}{\mathrm{d}t} = -x^3 + \eta_t, \tag{2.2}$$

$$\frac{\mathrm{d}x}{\mathrm{d}t} = -(x+\eta_t)^3. \tag{2.3}$$

Equation (2.2) is a classic Langevin equation with cubic attraction towards zero and diffusive noise—easily interpreted (in e.g. the Itô sense) as the stochastic differential equation (SDE) $\mathrm{d}x = -x^3\mathrm{d}t + \mathrm{d}W$ (where $\mathrm{d}W$ represents the usual derivative of a Wiener process), enabling all the analytical and numerical options that entails.

Equation (2.3), however, is notably different in that the nonlinear cubing operation happens to a fundamentally random quantity, linking the deterministic and random parts of the equation. Naïve numerical simulation of such a process simply converges to deterministic behavior as the time-step shrinks, since the fluctuations average out before x changes considerably. If timestep-independent stochastic behavior is desired, we must develop a new consistent and coherent interpretation of this equation.

"Baked-in" stochasticity of this type might arise in a variety of physical modeling scenarios. For example, nonlinear drag forces acting on a macroscopic object in a turbulent flow would cause velocity to evolve according to this type of Langevin equation, with "noise" coming from rapidly fluctuating relative fluid velocity—including, e.g., viscous drag on a cylinder in a turbulent wake [**47**]. We compute results for this velocity distribution, and its stark difference from a naïve approach, at the end of this section. Physical systems with nonlinear feedback based on rapidly fluctuating quantities or quantities subject to random measurement error would also be of this type. Inasmuch as measurement error acts as independent random variation of a quantity, the behavior of simulated or artificially forced dynamical systems would also benefit from this analysis. Our interest was motivated by an earlier model for individuals reacting to a stochastic political environment [**1**]. A variety of other physics-inspired nonlinear models of complex real-world phenomena may also share this form.

We note that the systems we are concerned with differ from other ways in which nonlinearity can arise in stochastic systems, for example in the deterministic part (e.g., [**48**]) or when x-dependence appears multiplied by the stochastic quantity (e.g., [**49**, **50**]), or when functions are applied to a continuous random-walking quantity rather than the uncertain/noisy quantity itself (as Itô's lemma would handle [**43**]). Certain specific problems exhibiting nonlinear dependence on stochastic quantities have been examined [**51**], but a general theory of this class of Langevin equations has not been developed.

Our argument is based on the consideration that over any finite time-scale, a theoretical system such as Eq. (2.3) will have experienced a large enough number of nearly-independent increments that the generalized central limit theorem should apply [**52**]. That is, the net increment over any finite time must be drawn from the family of *stable distributions*, or—if the intrinsic noise has finite variance—a Gaussian distribution in particular [**52**]. This intuitively dovetails with the more practically-motivated necessary condition that, in the numerical simulation of any continuous-time system, its behavior must not depend sensitively on the simulated timestep; that is, one relatively large step must result in the same distribution (in an ensemble average sense) as the commensurate number of arbitrarily small steps.

We proceed henceforth with the assumption of finite underlying variance. This means that the increment over any small but finite time must be drawn from a Gaussian distribution with mean equal to the mean of the underlying process. We may also choose this distribution's variance per unit time to likewise match the underlying process, maintaining consistency with the classic Langevin-Itô conversion and agreement in standard cases.

By this reasoning, we argue that every such stochastic process with finite variance is in fact *equivalent* to an Itô SDE over any finite time-scale: in particular, the SDE with deterministic part matching the underlying mean behavior and random part matching its standard deviation. We note that this is not a one-to-one mapping, but rather many-to-one: any stochastic process with the same mean and standard deviation would behave identically, and thus be represented by the same Itô SDE.

That is, for a general stochastic system of the form

$$\frac{\mathrm{d}x}{\mathrm{d}t} = R(x, t, \eta_t) \sim P(r|x, t),$$

where R is some finite-variance stochastic quantity dependent on x and δ-correlated in time, with distribution P, one should simulate the Itô SDE

$$\mathrm{d}x = F(x,t)\mathrm{d}t + G(x,t)\mathrm{d}W, \quad \text{where}$$

$$F(x,t) = \text{mean}\left[R(x,t)\right] = \int_{-\infty}^{\infty} rP(r|x,t)\mathrm{d}r,$$

$$G(x,t) = \text{std}\left[R(x,t)\right] = \sqrt{\int_{-\infty}^{\infty} \left[r - F(x,t)\right]^2 P(r|x,t)\mathrm{d}r},$$

if these quantities exist. We will limit ourselves to stationary and autonomous processes (i.e., $F(x,t) = F(x)$ and $G(x,t) = G(x)$) from this point forward, but the theory should extend to non-stationary processes.

Once we have this Itô equation, we may use standard numerical integration techniques for individual trajectories, or convert the system to a Fokker-Planck form and evolve the

solution's probability distribution $\rho(x)$ directly, with

$$\frac{\partial \rho(x,t)}{\partial t} = -\frac{\partial}{\partial x}\left[F(x)\rho(x,t)\right] + \frac{1}{2}\frac{\partial^2}{\partial x^2}\left[G(x)^2\rho(x,t)\right] \ .$$

As an example, we will now examine a slightly generalized version of Eq. (2.3) to determine the effect of noise with arbitrary constant amplitude σ:

$$\frac{\mathrm{d}x}{\mathrm{d}t} = -(x + \sigma\eta_t)^3. \tag{2.4}$$

In section 2.S.1,we examine a yet more general version of this attractor with arbitrary positive-integer exponent, but for illustration and concreteness henceforth focus on this cubic nonlinear-stochastic attractor. Using the shorthand notation $N(r|\mu,\sigma) = e^{\frac{-(r-\mu)^2}{2\sigma^2}}/(\sigma\sqrt{2\pi})$, we have:

$$\begin{aligned} F(x|\sigma) &= \int_{-\infty}^{\infty} -r^3 N(r|x,\sigma)\mathrm{d}r \\ &= -x^3 - 3\sigma^2 x \end{aligned}$$

and

$$\begin{aligned} G(x|\sigma) &= \sqrt{\int_{-\infty}^{\infty} [-r^3 - F(x)]^2 N(r|x,\sigma)\mathrm{d}r} \\ &= \sqrt{9\sigma^2x^4 + 36\sigma^4x^2 + 15\sigma^6}. \end{aligned}$$

So we argue that the system

$$\frac{\mathrm{d}x}{\mathrm{d}t} = -(x + \sigma\eta_t)^3$$

is equivalent to the Itô SDE

$$\mathrm{d}x = (-x^3 - 3\sigma^2 x)\ \mathrm{d}t + \sqrt{15\sigma^6 + 36\sigma^4 x^2 + 9\sigma^2 x^4}\ \mathrm{d}W, \tag{2.5}$$

which is amenable to various methods of simulation and analysis like any other Itô equation. We note that this Itô equation is significantly different from anything one might obtain from the similar-looking but simply additive Langevin form in Eq. (2.2).

To reiterate: a naïve interpretation of Eq. (2.4) would lead to the Itô SDE

$$\mathrm{d}x = -x^3\mathrm{d}t + \sigma^3\mathrm{d}W\ , \tag{2.6}$$

which has completely different physical behavior than our proposed interpretation in Eq. (2.5)[1]. Basic properties like the variance of the equilibrium distribution differ, with divergence possible in Eq. (2.5) but not in Eq. (2.6). This has significant implications for all types of stochastic models used throughout physics.

As an illustrative physical example, we consider the regime of quadratic drag with rapidly varying relative fluid velocity—of relevance to the behavior of particles in well-developed turbulence. In the one-dimensional case without stochasticity, relative velocity v would vary as $\mathrm{d}v/\mathrm{d}t = -cv|v|$ (here the constant c sets the time scale, and we set it to

[1]In our "naive" interpretation, we assume expansion of $(x + \sigma\eta)^3$ would be approximated with constant noise of amplitude σ^3, though the amplitude of constant noise could also be taken to be a fitted constant.

1 henceforth). When random velocity fluctuations are included, we have:

$$\frac{\mathrm{d}v}{\mathrm{d}t} = -(v + \sigma\eta_t)|v + \sigma\eta_t|. \tag{2.7}$$

This might naïvely be modeled by the Itô equation

$$\mathrm{d}v = -v|v|\mathrm{d}t + \sigma^2\mathrm{d}W\ , \tag{2.8}$$

which has an exact solution for its steady-state probability distribution

$$p(v) = \frac{C}{\sigma^{2/3}} \exp\left(\frac{-2|v^3|}{3\sigma^2}\right), \tag{2.9}$$

where C is a normalization constant, namely $3^{7/6}\Gamma(2/3)/(2^{5/3}\pi)$.

But this system is more faithfully modeled by using our proposed conversion, which yields

$$\mathrm{d}v = F_2(v|\sigma)\mathrm{d}t + G_2(v|\sigma)\mathrm{d}W\ , \tag{2.10}$$

where

$$F_2(v|\sigma) = -\left(\sigma^2 + v^2\right)\mathrm{Erf}\left(\frac{v}{\sigma\sqrt{2}}\right) - \sqrt{\frac{2}{\pi}}x\sigma e^{\frac{-v^2}{2\sigma^2}},$$
$$G_2(v|\sigma) = \sqrt{v^4 + 6v^2\sigma^2 + 3\sigma^4 + 3[F_2(v|\sigma)]^2}$$

(computation details in section 2.S.1).The significant difference in behavior between these systems is illustrated in in Fig. 2.1.

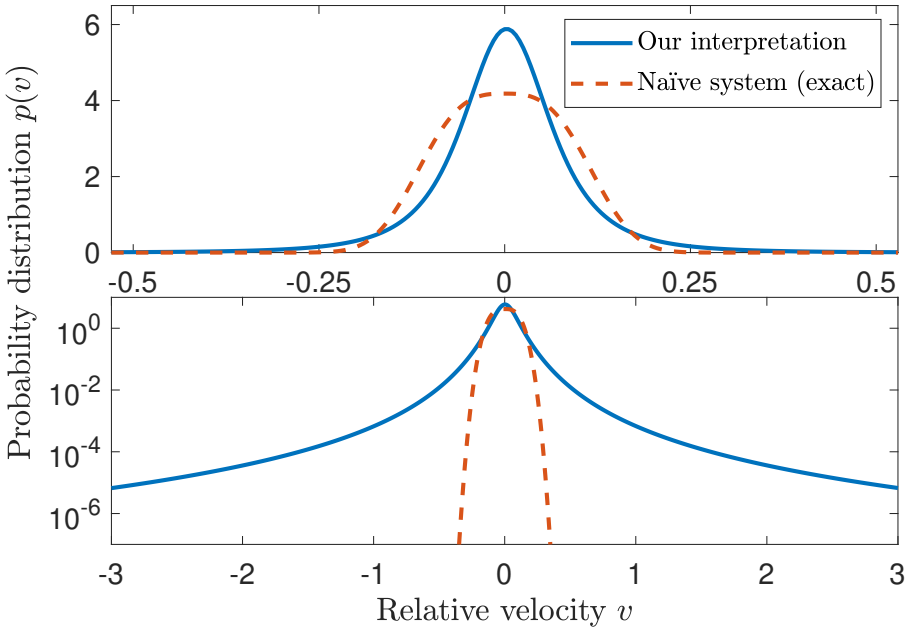

Figure 2.1. **Equilibrium velocity distributions.** Comparison of equilibrium distributions for the drag system in Eq. (2.7) with $\sigma = 0.2$, computed by Fokker-Planck integration of our proposed behavior (2.10) and compared to the exact solution (2.9) for a naïve interpretation of the system's behavior.**Top:** Linear scale. **Bottom:** Zoomed-out log-scale view, emphasizing clear differences in implied behaviors.

2.3. Equilibrium Moment Analysis of Itô SDEs

We now shift our focus from Itô interpretation of generalized Langevin equations to a technique of equilibrium analysis for Itô SDEs themselves. Equilibrium distributions are of considerable interest in any system where they exist. However, in some cases, direct analytical calculation of the steady-state distribution (as described in, e.g., [**43**]) requires integrals that fail to converge. Our interpretation of the stochastic cubic attractor (2.5) is of this type, and we will show that this technique yields insight into its structure.

Suppose we seek to examine the equilibrium distribution (if it exists) of the autonomous Itô SDE

$$\mathrm{d}x = F(x)\mathrm{d}t + G(x)\mathrm{d}W. \tag{2.11}$$

We will use Euler-Maruyama numerical integration [**53**] as a guide: in discrete time, we have

$$\Delta x = F(x)\Delta t + G(x)\sqrt{\Delta t}\ \eta, \tag{2.12}$$

where $\eta \sim N(0,1)$. We may write the expression for the distribution of the new value $\xi = x + \Delta x$ from any previous position x:

$$\begin{aligned} \xi &\sim N\left(x + F(x)\Delta t\ ,\ G(x)\sqrt{\Delta t}\right)\ , \\ P(\xi|x) &= \frac{1}{G(x)\sqrt{2\pi\Delta t}} e^{\frac{-[\xi - x - F(x)\Delta t]^2}{2G(x)^2\Delta t}}\ . \end{aligned} \tag{2.13}$$

Given this probability density function (PDF) for the outcome of a single step from any initial position x, we may write an expression for the evolution of the solution PDF from initial state $\rho_k(x)$ to subsequent state $\rho_{k+1}(x)$ a short time Δt later:

$$\rho_{k+1}(\xi) = \int_{-\infty}^{\infty} P(\xi|x)\rho_k(x)\mathrm{d}x\ .$$

At equilibrium, this operation leaves the distribution $\rho_k = \rho_{k+1} = \rho^*$ unchanged, i.e.,

$$\rho^*(\xi) = \int_{-\infty}^{\infty} P(\xi|x)\rho^*(x)\mathrm{d}x\ . \tag{2.14}$$

Rather than attempt to solve this implicit integral equation for ρ^* directly, we instead examine the second (raw) moment of the distribution μ_2 by multiplying both sides of Eq. (2.14) by ξ^2 and integrating over all ξ:

$$\mu_2 = \int_{-\infty}^{\infty} \xi^2 \rho^*(\xi) \mathrm{d}\xi = \int_{-\infty}^{\infty} \xi^2 \left[\int_{-\infty}^{\infty} \rho^*(x) P(\xi|x) \mathrm{d}x \right] \mathrm{d}\xi$$
$$= \int_{-\infty}^{\infty} \rho^*(x) \int_{-\infty}^{\infty} \xi^2 \frac{1}{G(x)\sqrt{2\pi\Delta t}} e^{\frac{-[\xi - x - F(x)\Delta t]^2}{2G(x)^2 \Delta t}} \mathrm{d}\xi \ \mathrm{d}x \ .$$

After swapping the order of integration[2], we observe that the inner integral over ξ is of the form

$$\frac{1}{s\sqrt{2\pi}} \int_{-\infty}^{\infty} u^2 e^{\frac{-(u-a)^2}{2s^2}} \mathrm{d}u = a^2 + s^2$$

with $u = \xi$, $a = x + F(x)\Delta t$, and $s = G(x)\sqrt{\Delta t}$. So we find

$$\mu_2 = \int_{-\infty}^{\infty} \rho^*(x) \Big[x^2 + 2xF(x)\Delta t + F(x)^2 \Delta t^2 + G(x)^2 \Delta t \Big] \mathrm{d}x \ .$$

Distributing the integral and subtracting μ_2 from both sides (note that the integral of x^2 against ρ^* is simply the definition of μ_2), we find

$$0 = \Delta t \int_{-\infty}^{\infty} \rho^*(x) \left[2xF(x) + G(x)^2 \right] \mathrm{d}x + \Delta t^2 \int_{-\infty}^{\infty} \rho^*(x) F(x)^2 \mathrm{d}x \ , \tag{2.15}$$

[2]Changes in the order of integration will always be allowable for finite μ_2.

which should hold exactly for any such Itô system. Enforcing this to leading order in Δt for our cubic stochastic attractor gives

$$\begin{aligned} 0 &= \int_{-\infty}^{\infty} \rho^*(x)\big[2x(-x^3 - 3\sigma^2 x) + (9\sigma^2 x^4 + 36\sigma^4 x^2 + 15\sigma^6)\big]\mathrm{d}x \\ &= 15\sigma^6 \int_{-\infty}^{\infty} \rho^*(x)\mathrm{d}x + (36\sigma^4 - 6\sigma^2) \int_{-\infty}^{\infty} x^2\rho^*(x)\mathrm{d}x + (9\sigma^2 - 2) \int_{-\infty}^{\infty} x^4\rho^*(x)\mathrm{d}x \ . \\ &= 15\sigma^6 + 6\sigma^2(6\sigma^2 - 1)\mu_2 + (9\sigma^2 - 2)\mu_4 \end{aligned} \tag{2.16}$$

So we obtain a relationship between moments of the equilibrium ρ^*.

However we notice a problem: if σ is large enough that $9\sigma^2 - 2 > 0$ and $6\sigma^2 - 1 > 0$ (i.e., $\sigma > \sqrt{2}/3$), all terms on the right hand side are positive and there is no way for the equality to hold.

If we had preserved all terms from Eq. (2.15), rather than truncating at leading order, we would have obtained the full, exact relation

$$0 = 15\sigma^6 + (36\sigma^4 - 6\sigma^2 + 9\sigma^4\Delta t)\mu_2 + (9\sigma^2 - 2 + 6\sigma^2\Delta t)\mu_4 + \Delta t\ \mu_6 \ . \tag{2.17}$$

This still does not avoid the problematic implication at large σ—in fact, it makes the situation slightly "worse" by adding more positive terms. This contradiction implies that we were wrong to treat μ_2 as finite: the equilibria for these values of σ must have infinite second moments.[3]

[3]We note that the earlier assumption of finite underlying stochastic-process variance was only necessary to arrive at the Itô SDE from the initial Langevin-type equation; our analysis of the Itô SDE itself does not rely on that assumption.

If we repeat our above analysis, but with the $2k^{\text{th}}$ moment of ρ^* instead of the second[4], we have

$$\begin{aligned}\mu_{2k} &= \int_{-\infty}^{\infty} \xi^{2k}\rho^*(\xi)\mathrm{d}\xi \\ &= \int_{-\infty}^{\infty} \rho^*(x) \int_{-\infty}^{\infty} \frac{\xi^{2k}}{G(x)\sqrt{2\pi\Delta t}} e^{\frac{-[\xi-x-F(x)\Delta t]^2}{2G(x)^2\Delta t}} \mathrm{d}\xi \ \mathrm{d}x \ . \end{aligned} \tag{2.18}$$

Integrals of the following form arise:

$$\begin{aligned} I_{2k} :&= \frac{1}{\sigma\sqrt{2\pi}} \int_{-\infty}^{\infty} u^{2k} e^{\frac{-(u-a)^2}{2\sigma^2}} \mathrm{d}u \\ &= (2k)! \sum_{i=0}^{k} \frac{\sigma^{2i} a^{2k-2i}}{(2i)!!(2k-2i)!} \ . \end{aligned}$$

So with any Itô SDE we have

$$\begin{aligned} \mu_{2k} &= \int_{-\infty}^{\infty} \rho^*(x) \left[(2k)! \sum_{i=0}^{k} \frac{(G(x)\sqrt{\Delta t})^{2i}(x+F(x)\Delta t)^{2k-2i}}{(2i)!!(2k-2i)!} \right] \mathrm{d}x \\ &= \sum_{i=0}^{k} \frac{(2k)!}{(2i)!!(2k-2i)!} \Delta t^i \int_{-\infty}^{\infty} \rho^*(x) G(x)^{2i} \sum_{j=0}^{2k-2i} \binom{2k-2i}{j} x^j [F(x)\Delta t]^{2k-2i-j} \mathrm{d}x \ . \end{aligned}$$

Regrouping by powers of Δt and retaining only leading order behavior, we find that the constant term ($i = 0, j = 2k$) cancels from the left hand side, leaving

$$0 = \Delta t \int_{-\infty}^{\infty} \rho^*(x) \left[2kx^{2k-1}F(x) + G(x)^2 \right] \mathrm{d}x \ .$$

[4]For symmetric equilibria like our cubic example, odd moments are all zero.

This relation should hold for any equilibrium of an Itô SDE for which the $2k^{\text{th}}$ raw moment is finite. If $F(x)$ and $G(x)^2$ are polynomials, this may be used to obtain a recursion relation for all moments of the equilibrium ρ^*.

For example, in the case of our cubic nonlinear-stochastic attractor from Eq. (2.4),

$$\begin{aligned} 0 &= \int_{-\infty}^{\infty} \rho^*(x)\Big[2kx^{2k-1}(-x^3 - 3\sigma^2 x) + (9\sigma^2 x^4 + 36\sigma^4 x^2 + 15\sigma^6)\Big]\mathrm{d}x \\ &= 15\sigma^6 + 36\sigma^4\mu_2 + 9\sigma^2\mu_4 - 6k\sigma^2\mu_{2k} - 2k\mu_{2k+2} \end{aligned}$$

for integers $k \geq 1$.

While this slightly under-specified system of equations doesn't yield exact moments, it implies that those moments should lie on a surface, which we confirm by numerical simulation (see section 2.S.2).When the typical magnitude of x is small compared to σ (i.e., $\mu_2 \ll \sigma^2$), however, Eq. (2.5) is well approximated by an SDE with constant noise and linear drift: an Ornstein–Uhlenbeck process [**54**,**55**] (see also, e.g., [**56**] or [**57**]). This implies a normal distribution at equilibrium, with moment relationship

$$\mu_4 = 3\mu_2^2. \tag{2.19}$$

Plugging this additional constraint into our lowest-order relation Eq. (2.16) yields

$$0 = 15\sigma^6 + 6\sigma^2(6\sigma^2 - 1)\mu_2 + 3(9\sigma^2 - 2)\mu_2^2 \,,$$

which agrees well with simulation in the relevant parameter region: see Fig. 2.2. For a direct look at the Gaussian nature of equilibria across this transition, see section 2.S.3.

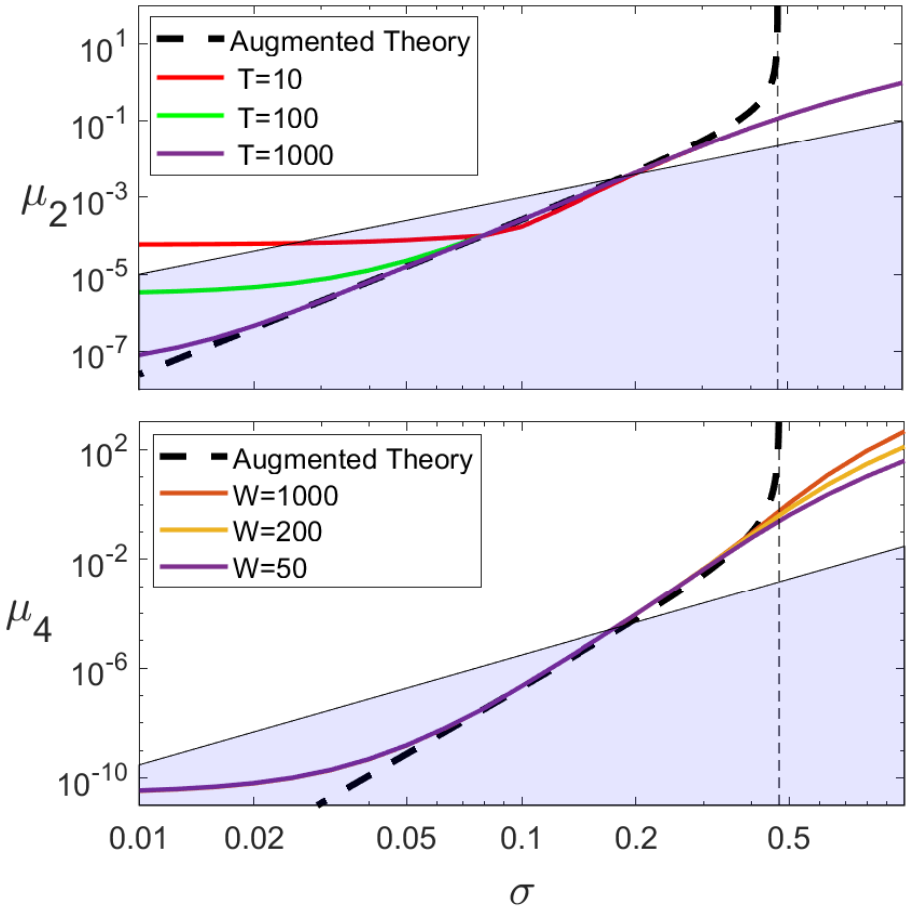

Figure 2.2. **Numerical validation.** Comparison of numerical results (via Fokker-Planck evolution) to the theoretical relation, augmented with the extra Gaussian condition $\mu_4 = 3\mu_2^2$. The shaded region indicates $\mu_2 < 0.1\sigma^2$ (top) and correspondingly $\mu_4 < 0.03\sigma^4$ (bottom), where the Gaussian approximation (from $\mu_2 \ll \sigma^2$) should be most valid. **Top:** Smaller σ values take longer simulated time T to equilibrate, but do approach the theorized line. For high noise amplitudes, the relation need not hold, and indeed theory suggests that μ_2 and μ_4 should diverge for $\sigma > \sqrt{2}/3$ (indicated by the vertical dashed line). **Bottom:** As predicted by theory, the fourth moment μ_4 does indeed appear to diverge for $\sigma > \sqrt{2}/3$, though simulation with ever wider domain width W (measured in number of standard deviations of the equilibrium solution) is needed capture more of the distribution's tails (all curves shown for $T = 100$).

2.4. Discussion and Limitations

The first proposition of this paper—the argument for Ito-equivalency of nonlinear Langevin-type systems—is really a proposed definition rather than a theoretical result. Like Langevin equations themselves, the notation is simple and intuitive, but solid mathematical interpretation requires the use of the more rigorous notation, and we propose that interpretation in terms of Itô calculus.

We apply logic based on the central limit theorem for finite-variance random variables, but the Langevin noise terms are not regular random variables and their variance may not be well-defined or finite. If variance is treated as well-defined but not finite, other (non-Gaussian) stable distributions per time-step may arise, rather than normally distributed Itô time-steps.

We also note the perhaps-undesirable sensitivity to the assumption of Gaussian underlying noise in Eq. (2.1). In particular, the assumption that η_t is normally distributed may be incorrect for some systems with biased or irregularly shaped noise (such as the Beta distributions of percepts in [**1**]), and if the noise shape is known it should be used.

The Itô equilibrium analysis ending with Eq. (2.15) applies to any Itô system with an equilibrium where the second raw moment of that equilibrium is finite, but it is of particular use when the functions F and G^2 are polynomial in nature, since this allows the analysis to culminate with a relation between even moments rather than merely integrals against an unknown distribution.

Finally, in the analysis of our particular cubic-attractor equilibrium, we have employed an approximation (valid only for $\sigma^2 \gg \mu_2$) which allowed us to fully prescribe the moments of the equilibrium when they are finite. It remains unclear whether a more general constraint valid for arbitrary σ can be found.

2.5. Conclusions

We have shown that a class of "nonlinear-stochastic" Langevin equations may be interpreted such that they have well-defined behavior after conversion to an equivalent Itô system. We have applied this theory to a class of nonlinear attracting fixed points to analyze their equilibria via moment relations, and showed that simulations bear out this analysis. This type of equilibrium may be more general than initially apparent, since nearly any isolated attracting fixed point is locally well-approximated by equations of this form.

This conversion technique should lead to more faithful physical modeling, yielding qualitatively different behavior when compared to simplifications which transform a deterministic quantity and add noise afterward. In particular, we have shown that there exists a critical noise level in one such system which leads to divergent moments of its equilibrium, something that cannot occur if x-independent noise is simply added after the nonlinear operation. Conversely, our reasoning also leads to the implication that apparent Itô behavior might be driven by any number of nonlinear Langevin processes.

Independent but complementary to these considerations, the equilibrium-analysis section of this work applies to all Itô systems, and can lead to recursive moment relations or other insights in their study when exact equilibrium solutions aren't attainable. In

particular, we note that the divergent moments this technique exposes for the example system would be difficult to deduce using numerical solutions of the Itô (or corresponding Fokker-Planck) equation in question.

2.S. Additional Mathematical Work

2.S.1. Generalization to positive-integer attractors

Here we examine a generalization of the nonlinear attracting system from the main text: the n^{th}-order attracting fixed point. As in the main text, the nonlinear attracting function is applied to a Gaussian random variable (in the Langevin sense) centered on the current value (using $N(r; x, \sigma)$ as shorthand for the Gaussian pdf with mean x and standard deviation σ):

$$\begin{aligned} r &:= x + \sigma\eta, \text{ i.e. } r \sim N(r|x,\sigma) \\ \frac{\mathrm{d}x}{\mathrm{d}t} &= -\operatorname{sgn}(r)|r|^n, \ n \in \mathbf{Z}^+ . \end{aligned} \tag{2.20}$$

Using the proposed Itô conversion from the main text, this should be equivalent to the system

$$\mathrm{d}x = F(x|\sigma,n)\mathrm{d}t + G(x|\sigma,n)\mathrm{d}W, \text{ where} \tag{2.21}$$

$$F(x|\sigma,n) = \left\langle \frac{\mathrm{d}x}{\mathrm{d}t} \right\rangle = \int_{-\infty}^{\infty} \Big[-\operatorname{sgn}(r)|r|^n \Big] N(r|x,\sigma)\mathrm{d}r \tag{2.22}$$

$$G(x|\sigma,n) = \operatorname{std}\left(\frac{\mathrm{d}x}{\mathrm{d}t}\right) = \sqrt{\int_{-\infty}^{\infty} [-\operatorname{sgn}(r)|r|^n - F(x|\sigma,n)]^2 N(r|x,\sigma)\mathrm{d}r}. \tag{2.23}$$

We first note that G can be easily computed in terms of F:

$$\begin{aligned}
G(x|\sigma,n) &= \sqrt{\int_{-\infty}^{\infty} \Big[-\operatorname{sgn}(r)|r|^n - F(x|\sigma,n)\Big]^2 N(r|x,\sigma)\mathrm{d}r} \\
&= \sqrt{\int_{-\infty}^{\infty} \Big[r^{2n} + 2\operatorname{sgn}(r)|r|^n F(x|\sigma,n) + F^2(x|\sigma,n)\Big] N(r|x,\sigma)\mathrm{d}r} \\
&= \sqrt{\int_{-\infty}^{\infty} r^{2n} N(r|x,\sigma)\mathrm{d}r + 2F(x|\sigma,n)\int_{-\infty}^{\infty} \operatorname{sgn}(r)|r|^n N(r|x,\sigma) + F^2(x|\sigma,n)\int_{-\infty}^{\infty} N(r|x,\sigma)\mathrm{d}r} \\
&= \sqrt{\mu_{2n,x,\sigma} + 3F^2(x|\sigma,n)},
\end{aligned}$$

where the first term is not quite $F(x|\sigma,2n)$—due to the sign difference—but rather the (much simpler) $2n^{\text{th}}$ non-central moment of the normal distribution $N(r|x,\sigma)$:

$$\begin{aligned}
\mu_{2n,x,\sigma} &:= \int_{-\infty}^{\infty} r^{2n} N(r|x,\sigma)\mathrm{d}r \\
&= \int_{-\infty}^{\infty} (x+z)^{2n} N(z|0,\sigma)\mathrm{d}z \\
&= \sum_{i=0}^{2n} \binom{2n}{i} x^{2n-i} \int_{-\infty}^{\infty} z^i N(z|0,\sigma)\mathrm{d}z \\
&= \sum_{j=0}^{n} \binom{2n}{2j} (2j-1)!! x^{2n-2j}\sigma^{2j} \ .
\end{aligned}$$

We now seek F. If n is odd, this calculation is simply the non-central moment again:

$$F(x|\sigma,n) = \int_{-\infty}^{\infty} -r^n \left[\frac{1}{\sigma\sqrt{2\pi}} e^{\frac{-(r-x)^2}{2\sigma^2}}\right] \mathrm{d}r \quad \text{if } n \text{ odd}$$

$$= \sum_{\substack{i=1 \\ i \text{ odd}}}^{n} \binom{n}{i} (i-1)!! x^{n-i}\sigma^i \tag{2.24}$$

$$= \sum_{\substack{i=1 \\ i \text{ odd}}}^{n} A_{n,i}\ x^{n-i}\sigma^i, \tag{2.25}$$

$$\text{where } A_{n,i} := \binom{n}{i}(i-1)!! = \frac{n!}{i!!(n-i)!}\ . \tag{2.26}$$

However if n is even, we must split the integral and the boundary terms no longer cancel due to the sign difference:

$$\begin{aligned}
F(x|\sigma,n) &= \int_{-\infty}^{\infty} \Big[-\operatorname{sgn}(r)|r|^n \Big] N(r;x,\sigma)\mathrm{d}r \\
&= \int_{-\infty}^{0} r^n N(r;x,\sigma)\mathrm{d}r - \int_{0}^{\infty} r^n N(r;x,\sigma)\mathrm{d}r \\
&= \int_{-\infty}^{\infty} r^n N(r;x,\sigma)\mathrm{d}r - 2\int_{0}^{\infty} r^n N(r;x,\sigma)\mathrm{d}r \\
&= \sum_{\substack{i=0 \\ i \text{ even}}}^{n} A_{n,i}\ x^{n-i}\sigma^i - 2\int_{-x}^{\infty} (x+w)^n N(w;0,\sigma)\mathrm{d}w \\
&= \sum_{\substack{i=0 \\ i \text{ even}}}^{n} A_{n,i}\ x^{n-i}\sigma^i - 2\sum_{i=0}^{n} \binom{n}{i} x^i \underbrace{\int_{-x}^{\infty} w^{n-i} N(w;0,\sigma)\mathrm{d}w}_{J_{-x}(n-i)}\ .
\end{aligned} \tag{2.27}$$

We then need to process the expression marked J using IBP, and unlike before we have boundary terms:

$$\begin{aligned} J_{-x}(p) :&= \int_{-x}^{\infty} w^p N(w;0,\sigma)\mathrm{d}w \\ &= \left[(-1)^{p-1}\frac{(p-1)!!}{\sqrt{2\pi}}e^{\frac{-x^2}{2\sigma^2}}\sum_{\substack{j=1\\ j \text{ odd}}}^{p}\frac{x^{p-j}\sigma^j}{(p-j)!!}\right] + \begin{cases} 0, & \text{if p odd} \\ \frac{(p-1)!!}{2}\sigma^p\left[1+\mathrm{Erf}\left(\frac{x}{\sigma\sqrt{2}}\right)\right], & \text{if p even .} \end{cases} \end{aligned}$$

We can now expand the relevant sum from (2.27), separating out the Erf parts of J from the sums:

$$\begin{aligned} -2\sum_{i=0}^{n}\binom{n}{i}x^i J_{-x}(n-i) &= -2\sum_{\substack{i=0\\ n-i \text{ even}}}^{n}\binom{n}{i}x^i\frac{(n-i-1)!!}{2}\sigma^{n-i}\left[1+\mathrm{Erf}\left(\frac{x}{\sigma\sqrt{2}}\right)\right] \\ &\quad -2\sum_{i=0}^{n}\binom{n}{i}x^i(-1)^{n-i-1}\frac{(n-i-1)!!}{\sqrt{2\pi}}e^{\frac{-x^2}{2\sigma^2}}\sum_{\substack{j=1\\ j \text{ odd}}}^{n-i}\frac{x^{n-i-j}\sigma^j}{(n-i-j)!!} \\ &= -\left[1+\mathrm{Erf}\left(\frac{x}{\sigma\sqrt{2}}\right)\right]\sum_{\substack{i=0\\ i \text{ even}}}^{n}A_{n,n-i}\,x^i\sigma^{n-i} \\ &\quad +\sqrt{\frac{2}{\pi}}e^{\frac{-x^2}{2\sigma^2}}\sum_{i=0}^{n}(-1)^i A_{n,n-i}\sum_{\substack{j=1\\ j \text{ odd}}}^{n-i}\frac{x^{n-j}\sigma^j}{(n-i-j)!!}\,, \end{aligned}$$

using the fact that n is even to recondition the sums and simplify the alternating negative sign. We now notice that we can combine all terms of constant j in the second line, rearranging the order of the sums:

$$\sqrt{\frac{2}{\pi}}e^{\frac{-x^2}{2\sigma^2}}\sum_{i=0}^{n}(-1)^i A_{n,n-i}\sum_{\substack{j=1\\ j \text{ odd}}}^{n-i}\frac{x^{n-j}\sigma^j}{(n-i-j)!!} = \sqrt{\frac{2}{\pi}}e^{\frac{-x^2}{2\sigma^2}}\sum_{\substack{j=1\\ j \text{ odd}}}^{n-1}x^{n-j}\sigma^j\sum_{i=0}^{n-j}(-1)^i\frac{A_{n,n-i}}{(n-i-j)!!}\,.$$

So we may rename index variables $i \to k$ and $j \to i$ and define another constant:

$$B_{n,i} := \sqrt{\frac{2}{\pi}} \sum_{k=0}^{n-i} (-1)^k \frac{A_{n,n-k}}{(n-k-i)!!} = \sqrt{\frac{2}{\pi}} \sum_{k=0}^{n-i} (-1)^k \binom{n}{k} \frac{(n-k-1)!!}{(n-k-i)!!}$$

in order to reunify the sums for even and odd i:

$$-2 \sum_{i=0}^{n} \binom{n}{i} x^i J_{-x}(n-i) = \sum_{i=0}^{n} x^{n-i} \sigma^i \cdot \begin{cases} -A_{n,n-i} \left[1 + \text{Erf}\left(\frac{x}{\sigma\sqrt{2}} \right) \right], & i \text{ even} \\ B_{n,i}\ e^{\frac{-x^2}{2\sigma^2}}, & i \text{ odd} \end{cases}.$$

And finally recombine with the first term of (2.27) to get F itself:

$$\begin{aligned} F(x|\sigma,n)|_{n \text{ even}} &= \sum_{\substack{i=0 \\ i \text{ even}}}^{n} A_{n,i}\ x^{n-i}\ \sigma^i + \sum_{i=0}^{n} x^{n-i}\sigma^i \cdot \begin{cases} -A_{n,n-i} \left[1 + \text{Erf}\left(\frac{x}{\sigma\sqrt{2}} \right) \right], & i \text{ even} \\ B_{n,i}\ e^{\frac{-x^2}{2\sigma^2}}, & i \text{ odd} \end{cases} \\ &= \sum_{i=0}^{n} x^{n-i}\sigma^i \cdot \begin{cases} A_{n,i} - A_{n,n-i} \left[1 + \text{Erf}\left(\frac{x}{\sigma\sqrt{2}} \right) \right], & i \text{ even} \\ B_{n,i}\ e^{\frac{-x^2}{2\sigma^2}}, & i \text{ odd} \end{cases}. \end{aligned} \tag{2.28}$$

In particular, for the $n = 2$ case which might have utility for modeling drag amidst turbulence, we have

$$\begin{aligned} F(x|\sigma,2) &= -\left(\sigma^2 + x^2\right) \text{Erf}\left(\frac{x}{\sigma\sqrt{2}} \right) - \sqrt{\frac{2}{\pi}} x\sigma e^{\frac{-x^2}{2\sigma^2}}\ , \\ \implies G(x|\sigma,2) &= \sqrt{\mu_{4,x,\sigma} + 3F^2(x|\sigma,2)} \\ &= \sqrt{x^4 + 6x^2\sigma^2 + 3\sigma^4 + 3\left[\left(\sigma^2 + x^2\right) \text{Erf}\left(\frac{x}{\sigma\sqrt{2}} \right) + \sqrt{\frac{2}{\pi}} x\sigma e^{\frac{-x^2}{2\sigma^2}} \right]^2}\ . \end{aligned}$$

2.S.2. Additional figures

Here we have provided some additional 3-dimensional figures elaborating on the 2-dimensional ones from the main text.

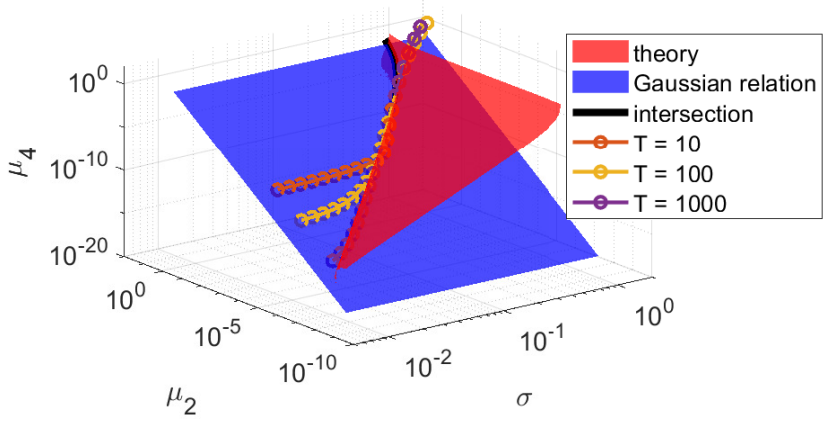

Figure 2.S3. **Small-noise convergence.** Three dimensional version of Fig. 1 (top panel) from the main paper; at small noise σ, solutions converge over increasing simulated time T to the intersection of the Gaussian condition and Eq. (11), our theorized surface from the main paper relating the equilibrium's second and fourth moments to the inherent noise σ: $0 = 15\sigma^6 + 6\sigma^2(6\sigma^2 - 1)\mu_2 + (9\sigma^2 - 2)\mu_4$.

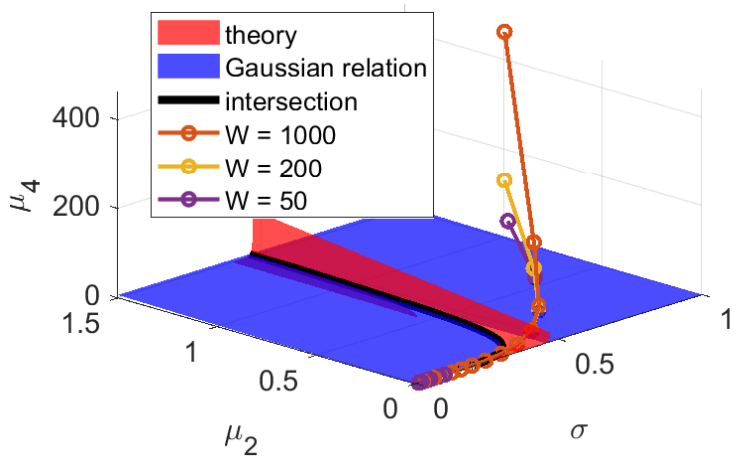

Figure 2.S4. **Large-noise divergence.** Three dimensional version of Fig. 1 (bottom panel) from main paper relating noise amplitude σ to the second and fourth moments of the equilibrium (μ_2 and μ_4, respectively), but on a linear scale. We can see the clear suggestion of divergence for (at least) μ_4; as our domain captures more standard deviations W of the solution, the measured μ_4 grows without bound. We propose that noise values σ beyond the asymptote "curtain" $\sigma^* = \sqrt{2}/3 \approx 0.47$ must have divergent second and fourth moments.

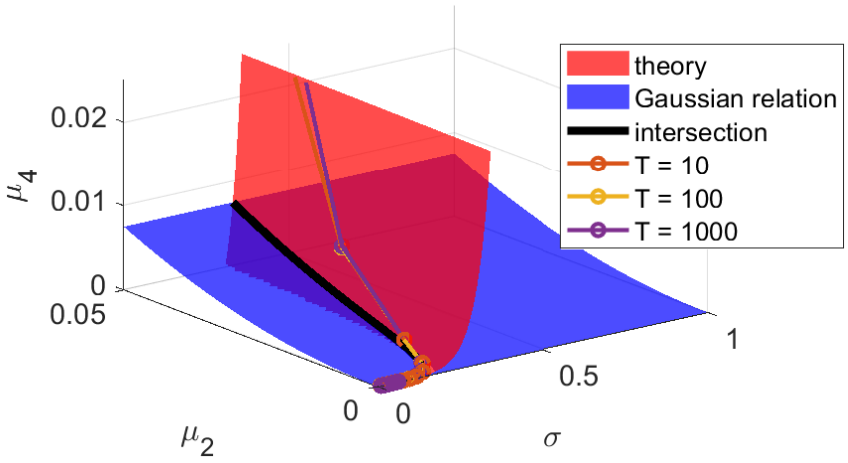

Figure 2.S5. **Gaussian validity boundary.** Three dimensional, linear-scale zoom of the region where the Gaussian assumption fails to hold. Our solutions fall off the intersection line due to their non-Gaussian nature.

2.S.3. Gaussian/non-Gaussian transition

In the main text we argue that the small-noise limit of the stochastic-cubic-attractor system leads to a Gaussian equilibrium. We can see this transition clearly in Fig. 2.S6.

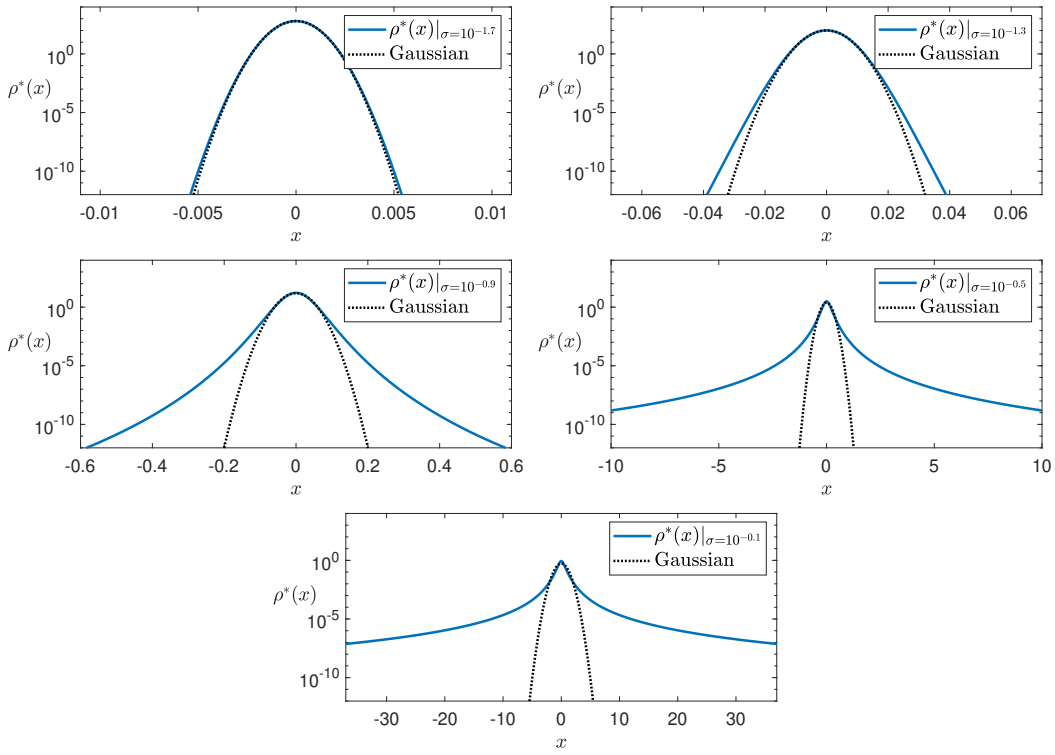

Figure 2.S6. **Equilibrium shape transition.** Comparison of equilibrium distributions for different noise values to Gaussian distributions with the same standard deviation. **Top Left:** For small σ, equilibria exhibit the signature parabolic shape (on semi-log axes) indicating a near-Gaussian distribution. **Other panels:** For larger σ, equilibria exhibit increasingly "fat tails" differentiating them from Gaussians.

CHAPTER 3

A Mexican Hat Dance: System of Ricker-Potential-Coupled Particles

3.1. Motivation

Systems of coupled particles are a classic problem in modeling and applied mathematics (e.g., [**58**–**61**] and many others) . The final project of this thesis involves the investigation of particles interacting via a "potential function" which exhibits finite short-distance repulsion and long-distance attraction: the Ricker wavelet (as explored in, e.g., [**62**, **63**]). Work has been done on the birth of multimodality in similar systems [**64**], but we wanted to explore the behavior as populations of such particles were "squeezed" together, similar in concept to "particle in a box" considerations from quantum physics (e.g., [**65**]). The most interesting domain to study ended up being the infinite real line with a quadratic potential well, but we also examined "oscillator" interpretations with the particles' positions on a circle representing phase (see section 3.S.4).

Local repulsion and distal attraction may call to mind the Lennard-Jones and Morse potentials from physics (see section 3.S.3). These models for intermolecular potential energy have features rendering them distinct from our Ricker wavelet: infinite repulsion in the case of Lennard-Jones, and a "sharp" non-differentiable peak at the origin for Morse. However, these models may not be applicable in situations where coexistence at the same position is allowed, due to their nonphysical implications at $x = 0$. However,

we believe a "smoothing" of the Morse potential's central peak (such as by integration against a "blurring" kernel function) would cause qualitatively similar results to what we observe in our Ricker system, and it is possible other "soft-core" potential systems (e.g., [**66**–**68**]) could find our results applicable. The smooth and coexistence-friendly dynamic embodied by our Ricker wavelet may also apply to neuronal phase models under proper conditions (e.g., [**69**–**71**]).

3.2. The Modified Ricker Potential

We use a modified[1] form of the Ricker wavelet as the potential function due to each particle:

$$U(x) = \left[1 - \left(\frac{k}{k-1}\right)\left(\frac{x}{s}\right)^2\right] e^{-k\left(\frac{x}{s}\right)^2}, \tag{3.1}$$

which is pictured in Fig. 3.1.

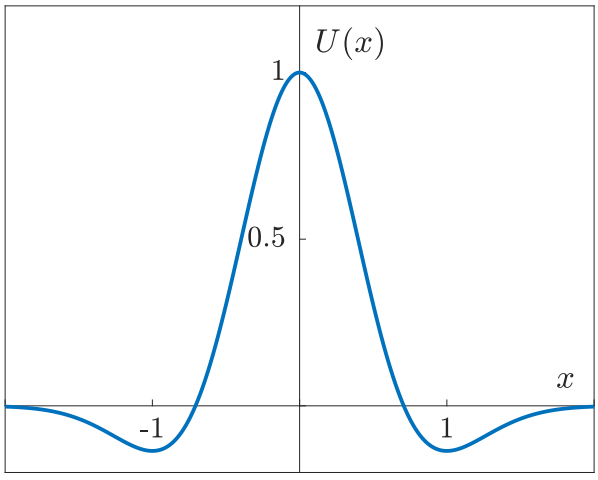

Figure 3.1. **Ricker Wavelet.** Our Ricker wavelet Eq. (3.1) with parameters $s = 1$ and $k = 2$.

[1]The "modification" here is an isolation of the trough position into the parameter s and other constants into the parameter k, while fixing the peak height at 1.

This function has the following nice properties:

(1) central peak at $(0, 1)$

(2) symmetric troughs at $x = \pm s$

(3) trough depth controlled by $k \in [1, \infty)$: as $k \to 1^+$, trough depth $\to \infty$, and as $k \to +\infty$, trough depth $\to 0^+$

Due to the central hump and symmetric troughs, this potential provides short-range, finite repulsion coupled with long-range attraction to a "preferred distance." This qualitative shape is known as a "Mexican Hat Potential."

The potential at position x due to a particle at position x_i is

$$U(x|x_i) = \left[1 - \frac{k}{(k-1)s^2}(x - x_i)^2\right] e^{-\frac{k(x-x_i)^2}{s^2}} . \tag{3.2}$$

We suppose that n particles, indexed 1 through n, have one-dimensional positions x_i and influence each other through their modified Ricker potential via the first order dynamical system

$$\frac{\mathrm{d}x_i}{\mathrm{d}t} = -\left.\frac{\mathrm{d}U_{tot}}{\mathrm{d}x}\right|_{x_i} = -\left.\left(\frac{\mathrm{d}U_0(x)}{\mathrm{d}x} + \sum_{j=1}^{n} \frac{\mathrm{d}U(x|x_j)}{\mathrm{d}x}\right)\right|_{x_i},$$

where confinement is imposed by the global potential function U_0, which we choose to have a quadratic shape

$$U_0(x) = \frac{x^2}{w^2}$$

with width-control parameter w. Figure 3.2 shows an example arrangement of particles in such an arrangement.

We note for later reference the first and second derivatives of our Ricker potential:

$$\frac{\mathrm{d}U}{\mathrm{d}x} = -\frac{2k^2}{(k-1)s^2}x\left(1-\frac{x^2}{s^2}\right)e^{-\frac{kx^2}{s^2}}\ , \tag{3.3}$$

and

$$\frac{\mathrm{d}^2U}{\mathrm{d}x^2} = -\frac{2k^2}{(k-1)s^2}\left[1-\frac{3+2k}{s^2}x^2+\frac{2k}{s^4}x^4\right]e^{-\frac{kx^2}{s^2}}\ . \tag{3.4}$$

In particular we note that particles have no self-interaction due to the zero derivative of the Ricker potential at the origin.

Unless otherwise noted, we use default parameter values $s = 1, k = 2$. We note that s may be scaled out of the problem entirely with appropriate scaling of space (via $\tilde{x} = x/s$ and $\tilde{w} = w/s$) and time (as $\tilde{t} = t/s$), but the parameter k does qualitatively affect behavior (as we briefly explore in Section 3.S.2 at the end of this discussion).

3.2.1. Intriguing Collective Behavior

Free of constraint (e.g., if $w \to \infty$), these particles settle into a uniform spacing, with each particle residing at the preferred distance s from its neighbors. However, when confined, they exhibit highly nonuniform and rich behavior.

With random starting positions, we see spontaneous organization of the particles depending on the choice of confinement parameter w. The particles form "stacks," since their repulsion weakens as they get nearer to each other, but the number of particles in each stack can vary, and indeed the stacks exchange particles as w changes. We demonstrate this spontaneous organization in Fig. 3.3. There is some slight asymmetry in Fig. 3.3 due

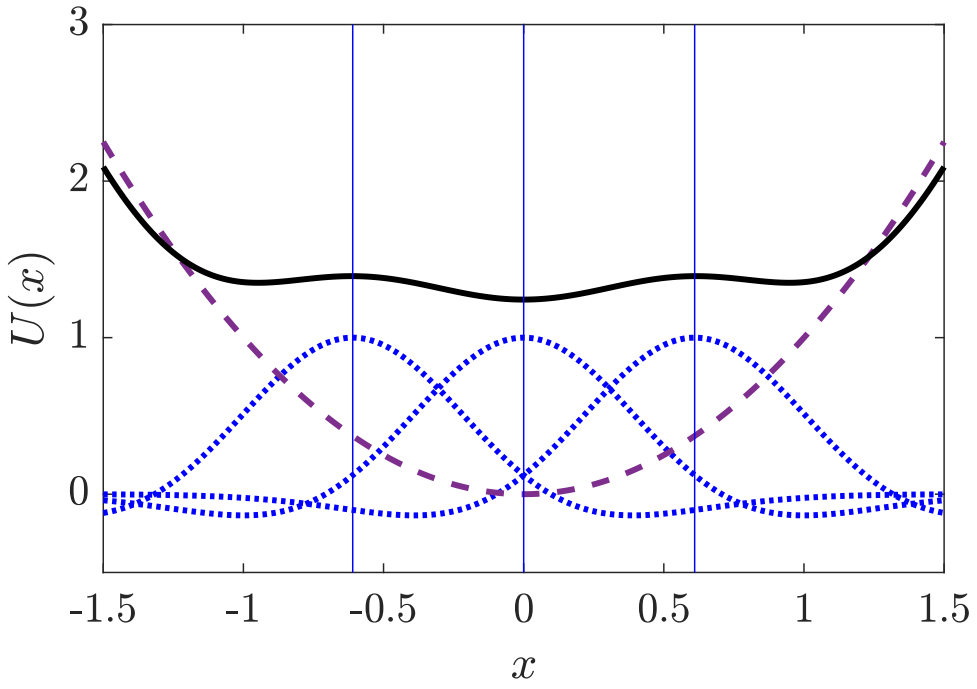

Figure 3.2. **Three particles at equilibrium.** Example of three particles at an equilibrium. The vertical solid blue lines show particle positions, the dotted blue curves show the particles' Ricker potentials, and the dashed maroon parabola is the background potential well. The solid black curve is the total potential, and we can see the derivative is zero at each particle's position, indicating this arrangement is at equilibrium. This arrangement is stable; since a particle never influences itself, each particle effectively "sees" the global potential minus its own contribution, which makes each particle's position in this arrangement a "trough" from its own point of view.

to high dimensional multistability with various stack sizes; if we enforce symmetry, we see a picture of "core" behavior as shown in Fig. 3.4.

We note that this is actually a 2-dimensional view of an n-dimensional bifurcation diagram, with each particle's position occupying one dimension. However, the interchangeability symmetry of the particles allows the display of the whole population to serve as analogue for any single particle's possible positions.

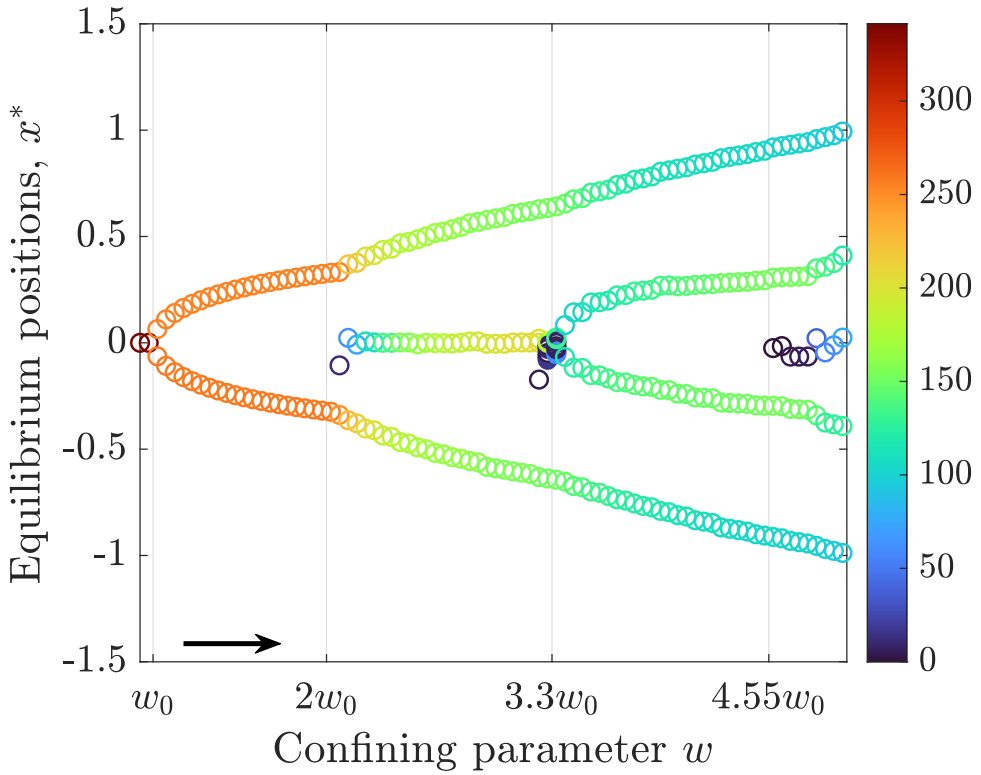

Figure 3.3. **Equilibrium diagram,** $n = 512$**.** A diagram showing equilibrium positions for a population of 512 independent Ricker-potential-carrying particles confined in a quadratic potential well. The horizontal w-axis tick marks are placed at approximate bifurcation points, and persist on other diagrams of this type for comparison's sake. The rightward-pointing arrow indicates that that equilibria were continued with gradually increasing parameter w. Ricker-potential constants for this run (and all other diagrams in this section) were $s = 1, k = 2$. See section 3.3 for additional simulation details.

3.3. Methods/Simulation details

Particles were started with random Gaussian positions with standard deviation 0.1 on the small-w end. The positions were updated using ODE45 numerical integration for an initial duration of $T = 20n^{-1/2}$ time units (chosen empirically to approximate equilibration-time scaling with n), with exponentially scaling integration time until all

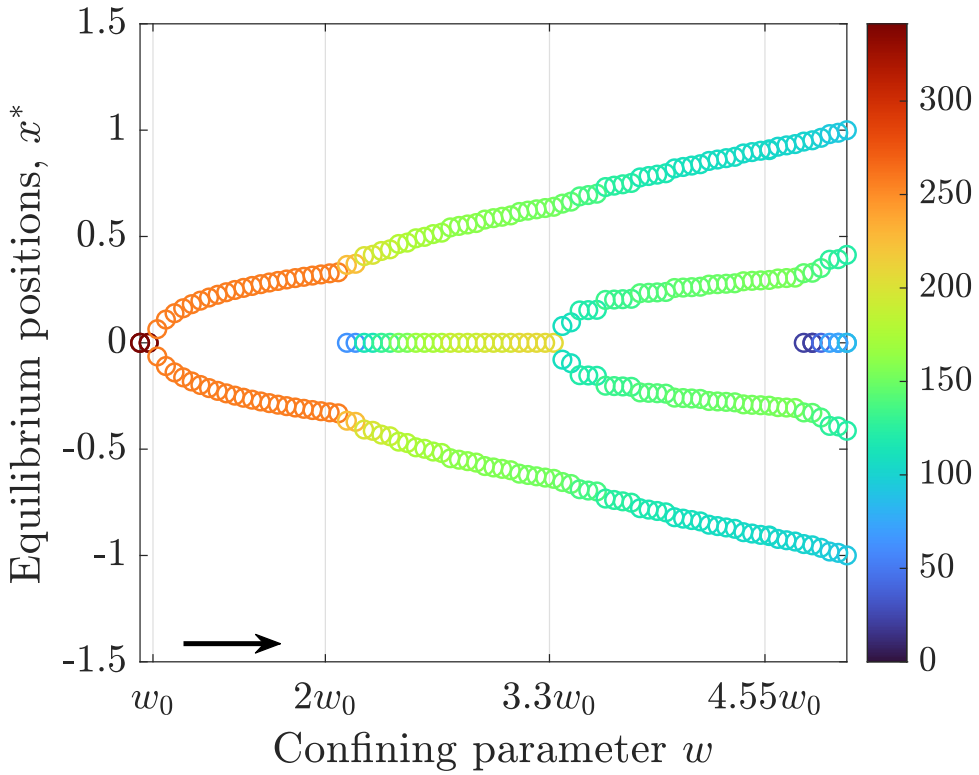

Figure 3.4. **Equilibrium diagram, $n = 512$, symmetry enforced.** A symmetry-enforced version of Fig. 3.3. Besides being "cleaner," however, we also notice the apparent bifurcation points change slightly.

particles have moved less than 0.001 units, or a run ends with $T > 5000n^{-1/2}$ (which occurs after 8 doublings, for a maximum total run-time of $10,220n^{-1/2}$ time units for any single w value). This was necessary since equilibration time grows dramatically near bifurcation points.

After each integration converged or hit the time limit at one w value, final positions were recorded and a small random perturbation of each particle's position (Gaussian with standard deviation 0.001) was applied to that ending state before the parameter value w was updated and the next simulation commenced—this ensured we only recorded stable

equilibria. This process proceeded from $w = 0.925w_0$ to $5w_0$ before descending along those same values; the black arrows in these diagrams indicate the direction of this continuation.

The stack-size information (encoded by color) can be further emphasized with a third dimension, as we show in Fig. 3.5. Thus we see even more clearly the pattern of sta-

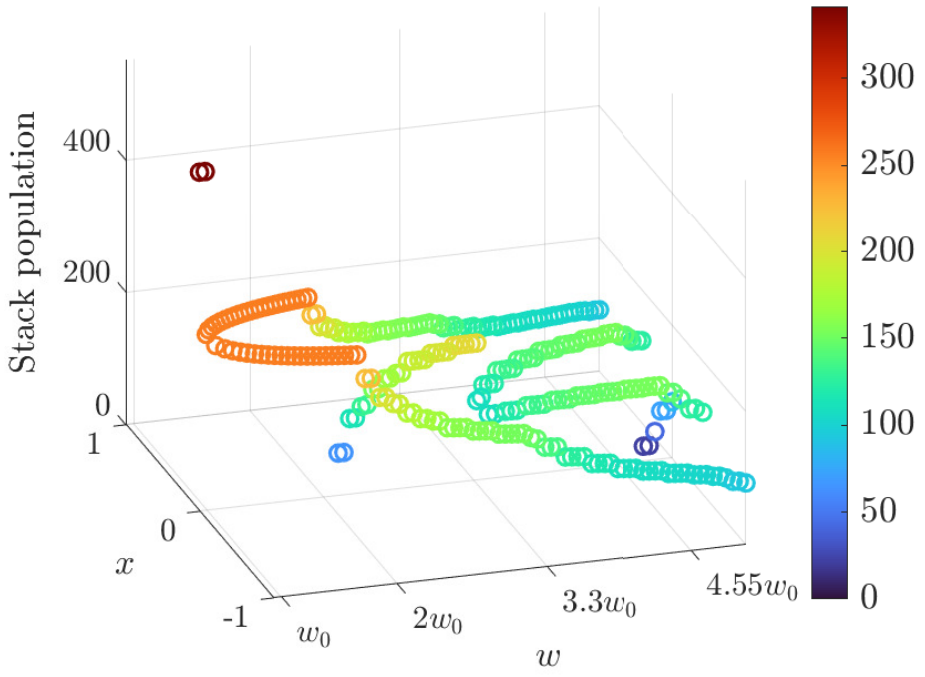

Figure 3.5. **Symmetry-enforced large system, 3D view.** A 3D view of the data in Fig. 3.4, with stack-size information encoded in the vertical axis as well as color. This emphasizes the continuous shift in population fractionation and the structure of the major bifurcations.

ble behavior. For very small w (strong confinement, i.e., a narrow parabolic well) all the particles stack up at the origin, but the population splits apart into two symmetric stacks[2] when w passes a critical threshold we label w_0—we derive a formula for this value

[2]There is some multistability with regards to slight asymmetry of these two stacks; for example, sometimes the stacks are 63 and 65 particles, and the system is stable, although in that case their positions are not perfectly symmetric—the larger stack settles slightly closer to the origin.

(Eq. (3.13)) in the "Large n analysis" section. As w continues to grow, the stacks drift apart and the origin becomes stable again, and we see particles "fall" inwards to settle there. Initially only a few particles stably rest there, but as the stacks continue to separate the central stack grows, until it becomes large enough to split into two in a manner that appears similar to its initial bifurcation at $w = w_0$.

There are many other, more complex equilibria possible, but for large n the equilibrium diagram appears to become increasingly well characterized by the aforementioned behavior, as shown in Fig. 3.6. All the "major" bifurcations (birth of central stacks, splitting of central stacks) appear to happen at the same multiples of the critical parameter value w_0, thus with proper scaling of the w axis (to match w_0) the diagrams appear increasingly similar to one another.

We will start our exploration with smaller, more tractable examples and then progress from there to the more general, large-n cases.

3.3.1. Small-n particular cases

3.3.1.1. Two-particle case. We can solve for the equilibrium condition by assuming based on symmetry that the two particles reside at $\pm x^*$— plugging in $2x^*$ as the distance in equation (3.3) and setting $\mathrm{d}x/\mathrm{d}t = -\mathrm{d}U_{tot}/\mathrm{d}x = 0$. The equilibrium condition on the

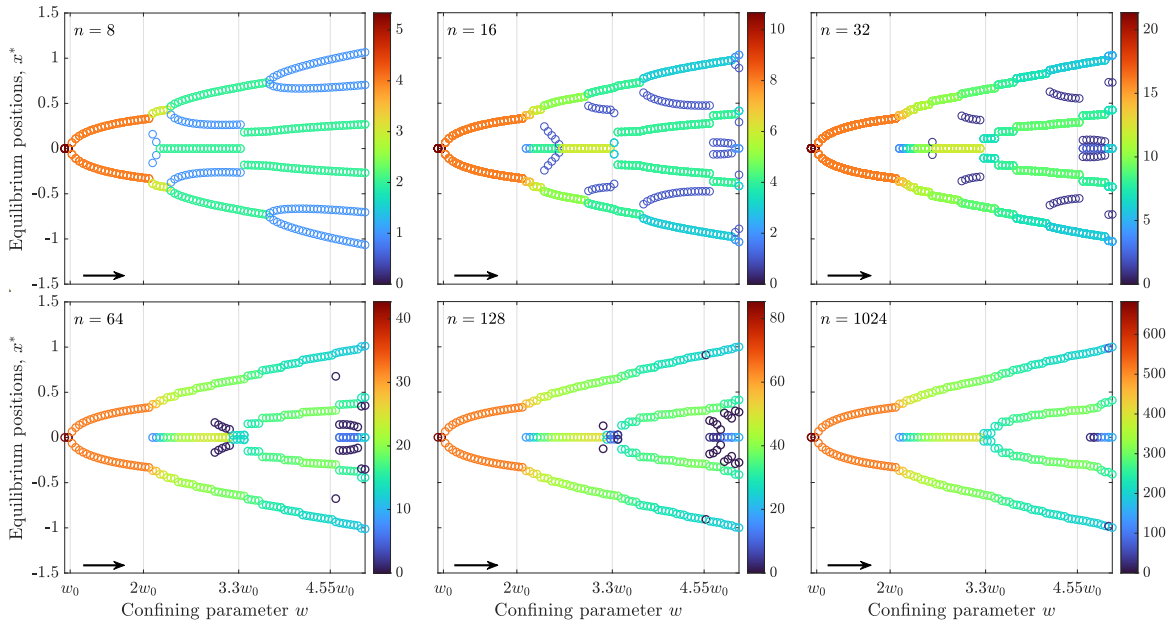

Figure 3.6. **Symmetry-enforced system, n convergence.** Equilibrium diagrams for increasing population sizes n. The diagrams appear to converge in a visual sense to the same few "major" bifurcations, which occur at nearly the same multiples of the critical parameter value w_0 (given in Eq. (3.13)). This motivates us to understand and characterize this large-n generic behavior.

particle at $+x^*$ becomes

$$\left.\frac{\mathrm{d}U_{tot}}{\mathrm{d}x}\right|_{x^*} = \frac{2x^*}{w^2} - \frac{4k^2x^*}{(k-1)s^2}\left(1-4\frac{x^{*2}}{s^2}\right)e^{-\frac{4kx^{*2}}{s^2}}$$

$$0 = 2x^*\left[\frac{1}{w^2}e^{\frac{4kx^{*2}}{s^2}} - \frac{2k^2}{(k-1)s^2}\left(1-4\frac{x^{*2}}{s^2}\right)\right]e^{-\frac{4kx^{*2}}{s^2}}$$

$$\implies x^* = 0 \qquad \text{or}$$

$$0 = \frac{1}{w^2}e^{\frac{4kx^{*2}}{s^2}} - \frac{2k^2}{(k-1)s^2}\left(1-4\frac{x^{*2}}{s^2}\right) \tag{3.5}$$

So the bifurcation diagram (in w against x^*) is given by the implicit equation (3.5), which can be solved explicitly for w^2 as:

$$w^2 = \frac{(k-1)s^2}{2k^2} \frac{e^{\frac{4kx^{*2}}{s^2}}}{\left(1 - 4\frac{x^{*2}}{s^2}\right)} \ ,$$

or solved for $(x^*)^2$ instead,

$$[x^*(w)]^2 = \frac{s^2}{4}\left[1 - \frac{1}{k}\, W\left(\frac{(k-1)s^2e^k}{2kw^2}\right)\right] \ , \tag{3.6}$$

where $W(\cdot)$ is the Lambert W function, defined as the solution to

$$W(z)e^{W(z)} = z \ .$$

Fig. 3.7 shows this solution overlaid on the equilibrium diagram for two particles.

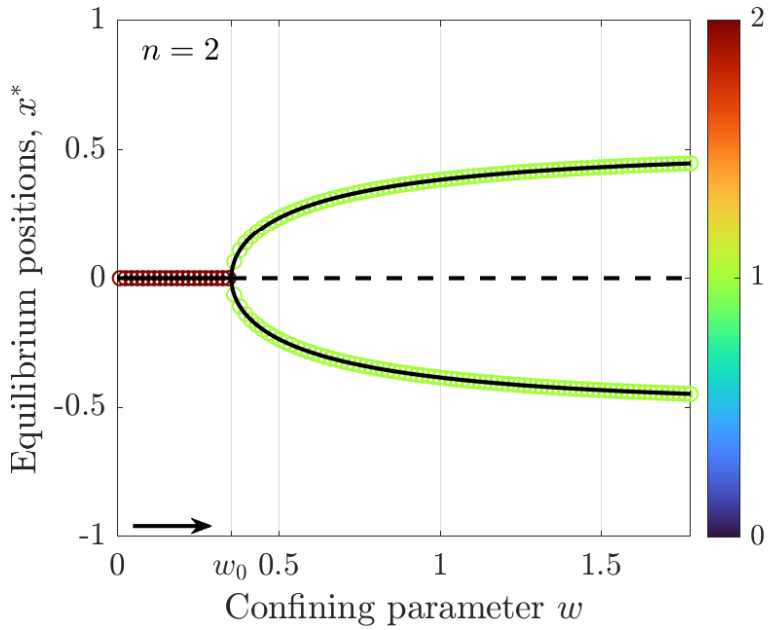

Figure 3.7. **Two-particle bifurcation diagram, with exact solutions.** Equilibria for the two-particle system, with exact analytical solutions $x^* = 0$ (dashed when unstable) and Eq. (3.5) overlaid in black. The critical parameter value w_0 ($= \frac{1}{\sqrt{8}}$ in this case) is marked as well.

For a more explicit, albeit approximate solution, we may expand (3.5) for small x^* (effectively assuming near-bifurcation w). Setting $x = \epsilon \ll 1$, we find

$$
\begin{aligned}
0 &= \frac{1}{w^2}\left(1 + \frac{4k\epsilon^2}{s^2} + O\left(\epsilon^4\right)\right) - \frac{2k^2}{(k-1)s^2}\left(1 - 4\frac{\epsilon^2}{s^2}\right) \ , \\
\frac{2k^2w^2}{(k-1)s^2} &= \frac{1 + \frac{4k\epsilon^2}{s^2} + O\left(\epsilon^4\right)}{1 - 4\frac{\epsilon^2}{s^2}} \\
&= \left(1 + \frac{4k\epsilon^2}{s^2} + O\left(\epsilon^4\right)\right)\left(1 + 4\frac{\epsilon^2}{s^2} + O\left(\epsilon^4\right)\right) \\
&= 1 + \frac{4+4k}{s^2}\epsilon^2 + O\left(\epsilon^4\right) \ , \\
w^2 &= \frac{(k-1)s^2}{2k^2}\left(1 + 4\frac{k+1}{s^2}\epsilon^2 + O\left(\epsilon^4\right)\right) \\
w(x) &\sim \frac{s}{k}\sqrt{\frac{k-1}{2}}\left(1 + 2\frac{k+1}{s^2}x^2 + O(x^4)\right) \ . \qquad (3.7)
\end{aligned}
$$

Then by inversion, defining the constant $w_{0,2}$, we can get the leading-order $x(w)$ behavior near this bifurcation:

$$w_{0,2} := \frac{s}{k}\sqrt{\frac{k-1}{2}} \tag{3.8}$$

$$x^*(w) \sim \frac{s}{\sqrt{2w_{0,2}(k+1)}}\sqrt{w - w_{0,2}}\ . \tag{3.9}$$

This matches the expansion of the exact Lambert-W-based solution near $w = w_{0,2}$. Eq. (3.8) gives w_0 for the $n = 2$ case; we derive the general-n version in the "Large-n analysis" section (Eq. (3.13)).

3.3.1.2. Three- and four-particle cases. Three- and four-particle systems have unique stable equilibria for all w, which are shown in Fig. 3.8; unfortunately these resist such easy exact-solution form as the $n = 2$ case. Other equilibria exist for these systems (such as $1-2$ states[3] in the $n = 3$ case, $1-2-1$ and $1-3$ states in $n = 4$, and the fully-stacked origin state at $w > w_0$), but none of them are stable. In Fig. 3.9 we show all such equilibrium positions using the MatCont analytical-continuation software package for Matlab (MatCont v7.3, see [**4**]) to track those unstable artificially-partitioned states as well as the stable state we actually see in regular numerical simulations.

The nonzero stable branches for $n = 3$ (and $k = 2, s = 1$) are solutions to the implicit equation

$$e^{8x^{*2}} + (4x^{*2} - 4)w^2 e^{6x^{*2}} + (32x^{*2} - 8)w^2 = 0\ ,$$

[3]This notation indicates the partition state of the particles, i.e., the number of particles in each stack, in order. In this case, there are two visibly-distinguishable $1-2$ states since the two-particle stack can be above or below the single-particle stack, though each of those represents six equilibria in full state space due to permutations of the particles.

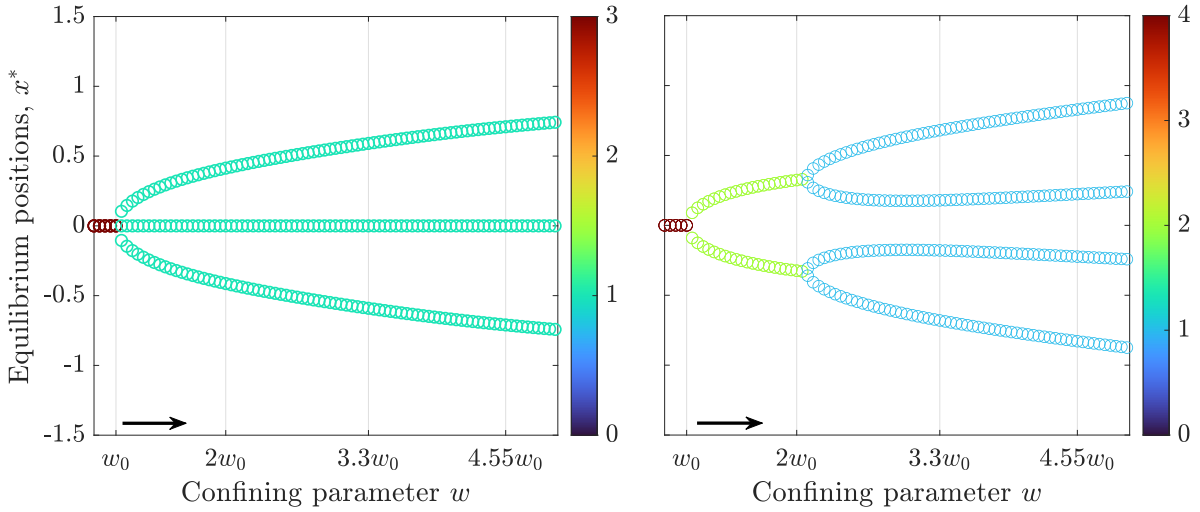

Figure 3.8. **Three- and four-particle bifurcation diagrams.** Equilibria for 3-particle (**left**) and 4-particle (**right**) systems. For these small n, these are the only stable states. Note that we have shifted to using multiples of w_0 on the w axis, for comparison with higher n cases.

which is the result of assuming symmetry (one particle at 0 and the other two at x^*) and solving for nonzero x^* solutions to the equilibrium condition on the particle at x^*. For large $w \gg w_0$ this relationship converges to $w^2 = e^{2x^2}(4-4x^2)^{-1}$ (or explicitly in x: $x^2 = 1 - \frac{1}{2}W(\frac{1}{2}e^2/w^2)$); for w near w_0 ($w_0 = \sqrt{3}/6$) the relation is well approximated by $x^2 \approx 1/9 - 1/108\ w^{-2}$ instead.

In the 4-particle case, $(n = 4, k = 2, s = 1)$ we can find the implicit equation for the $2-2$ (i.e. two stacks of two particles each) state, namely

$$w^2 = \frac{e^{8x^{*2}}}{16(1-4x^{*2})}\ ,$$

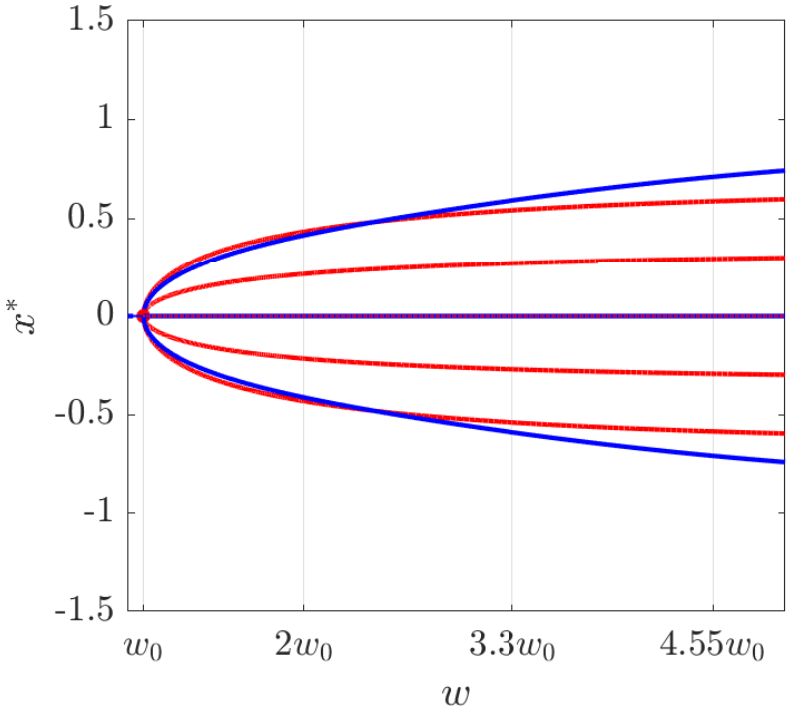

Figure 3.9. $n = 3$ **bifurcation diagram, all equilibria.** The equilibrium diagram similar to the left panel of Fig. 3.8, but made with analytical-continuation software (MatCont v7.3) [**4**], showing unstable equilibria (in red) as well as stable ones (in blue). We note that since this is a 2D projection of a 4D bifurcation diagram (all three state variables are superimposed on the same vertical axis), stable and unstable branches appear to "cross" without exchanging stability but in fact belong to entirely different branches in state space. For example, the stable curved branches correspond to the outer particles of the $1-1-1$ state, while the red branches which cross them are for the single particle in the unstable $2-1$ state (meanwhile the inner branches correspond to the location of the 2-stack in that state). Similarly, the origin beyond w_0 is a stable position if the system is in the $1-1-1$ state but an unstable position for the fully-stacked state, so it is both blue and red-dotted in this figure.

which is stable from $w = w_0$ ($= 1/4$ in this case) to $w \approx 2.1w_0$ as seen in Fig. 3.8. More exactly, the $2-2$ state splits into the $1-1-1-1$ state when $w = w_c$, where

$$w_c^2 = \frac{1 + 20x^{*2} - 64x^{*4}}{16(1 - 4x^{*2})} \ ,$$

and where x^* satisfies the implicit equation

$$1 + 20x^{*2} - 64x^{*4} = e^{8x^{*2}} \ .$$

The $1-2-1$ state, while never stable, is also relatively tractable, with outer stack positions given by the relation

$$8w^2 = \frac{e^{8x^2}}{1 - 4x^2 + (1-x^2)e^{6x^2}} \ .$$

$$\mathrm{d}x = F(x)\mathrm{d}t + G(x)\mathrm{d}W$$

Other particular states may also have similar implicit equilibrium expressions, but their multitude makes this endeavor an impractical strategy for understanding the system for general n.

3.3.1.3. Five-particles: birth of multistability. With five particles, we see the first case where there is multistability, by two different mechanisms. First of all, unlike $n = 3$ the origin cannot stably hold a particle as we cross w_0, and the population splits into a $3-2$ state, which is necessarily asymmetric in position. Then the indifference between which stack has 3 particles leads to bistability between two visibly different states, though they might be considered the same state up to reflection of the domain. Second, the point that the system drops to a $2-1-2$ state (on an increasing-w pass) is different from the point that it jumps back to the $3-2$ state (on a decreasing-w pass). We can see this in the difference between upper-left and upper-right panels in Fig. 3.10. This is because there is a region of bistability between $3-2$ and $2-1-2$ configurations—the loss of stability of $3-2$ happens at a higher w value than the gain of stability of $2-1-2$. This hysteresis

with respect to increasing and decreasing parameter w is explored more generally in the "Medium-n analysis" section below.

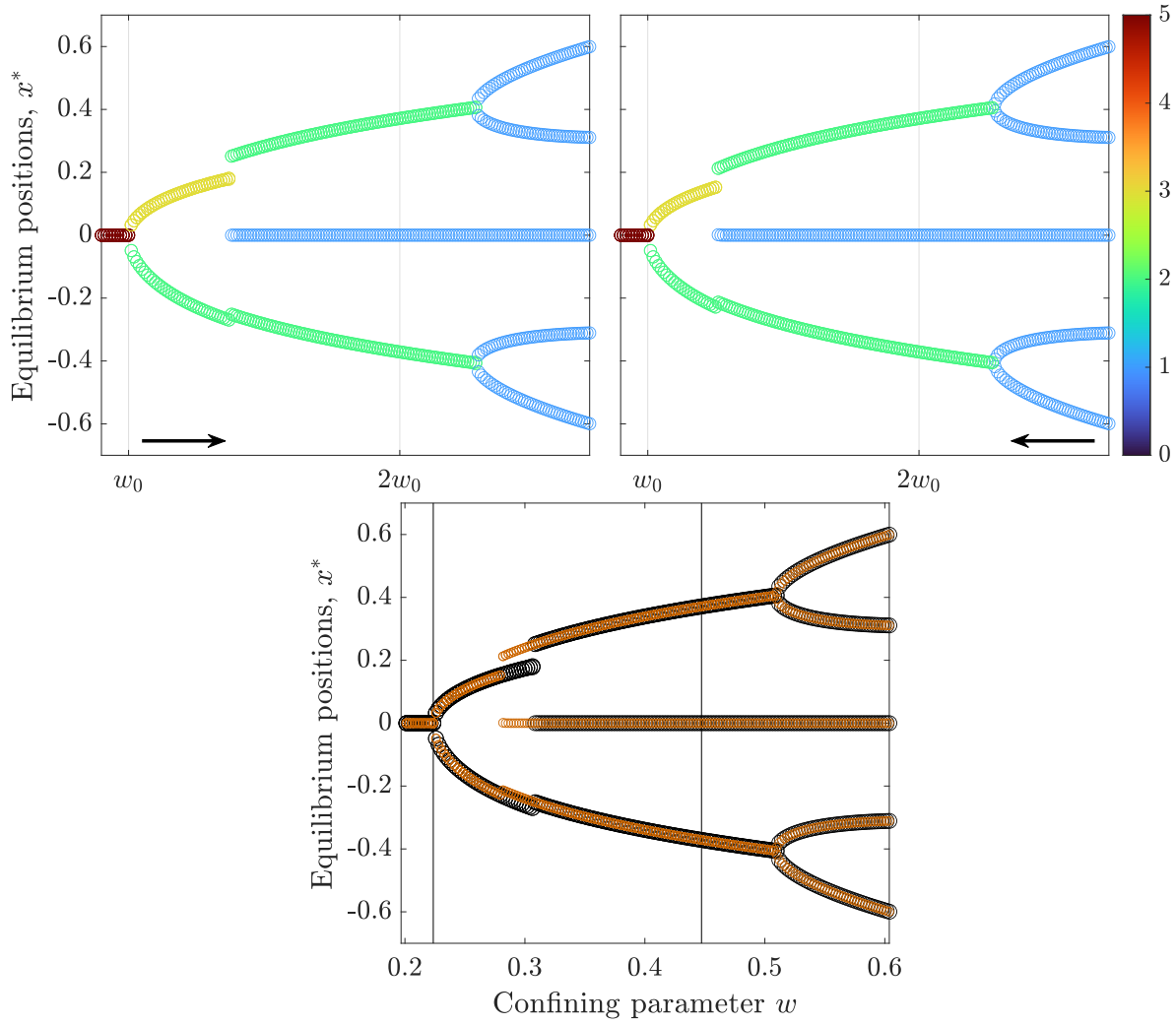

Figure 3.10. **Increasing- and decreasing-w equilibrium diagrams, five particles.** Zoomed equilibrium diagrams for five particles. **Top Left:** increasing-w pass; note the asymmetric $3-2$ state arms are slightly longer. **Top Right:** decreasing-w pass, with shorter $3-2$ arms. The overlapping region exhibits bistability of $3-2$ and $2-1-2$ states. **Bottom:** Overlay with increasing-w in black and decreasing-w in orange, emphasizing the area of bistability around $w = 0.3$. Previous w_0 multiple reference points persist as vertical lines, but decimal values are provided for finer reference.

3.3.2. Medium-n analysis

To get a sense of how the transition to the large-n behavior happens, we will look at a medium-scale n, in particular $n = 32$.

Figure 3.11 shows part of the bifurcation diagram for 32 particles, which shows hints of the dynamical process by which the particles transfer between stacks. At this resolution, we can see three "connecting" branches in the top right (decreasing-w) figure where single particle pairs transfer from the central stack to the outer ones.

Just as with the $n = 3$ and $n = 4$ diagrams, there are many more equilibria than we see in Fig. 3.11. First of all, we only see stable equilibria due to our method of forward-time numerical integration with minutely perturbed initial conditions, so we do not see the huge number of unstable equilibria. Second, we have enforced symmetry in this simulation, so we are missing the slightly asymmetric *stable* states that can (and generally do) result when particles are individually free; the enforcement of symmetry is nevertheless justified as we seek a generic central pattern around which many co-stable perturbations exist. But even in the symmetric case, there is co-stability of states, which is demonstrated by the discrepancy between increasing- and decreasing-w passes. Exploring these discrepancies will provide intuition about how the system behaves at higher n.

3.3.2.1. Repeated Hysteresis. The bottom panel of 3.11 emphasizes the differences between the increasing- and decreasing-w passes, with increasing-w pass in black and decreasing-w in orange. Two of those "branches" are isolated in Fig. 3.12.

To understand the hysteresis in Fig. 3.12, we start at the left side of the left-two figures, at $w = 0.2$. The top-left figure, a scatter plot of the full population, hides the stack-size information, but this is a $12 - 8 - 12$ arrangement in both black (increasing-w)

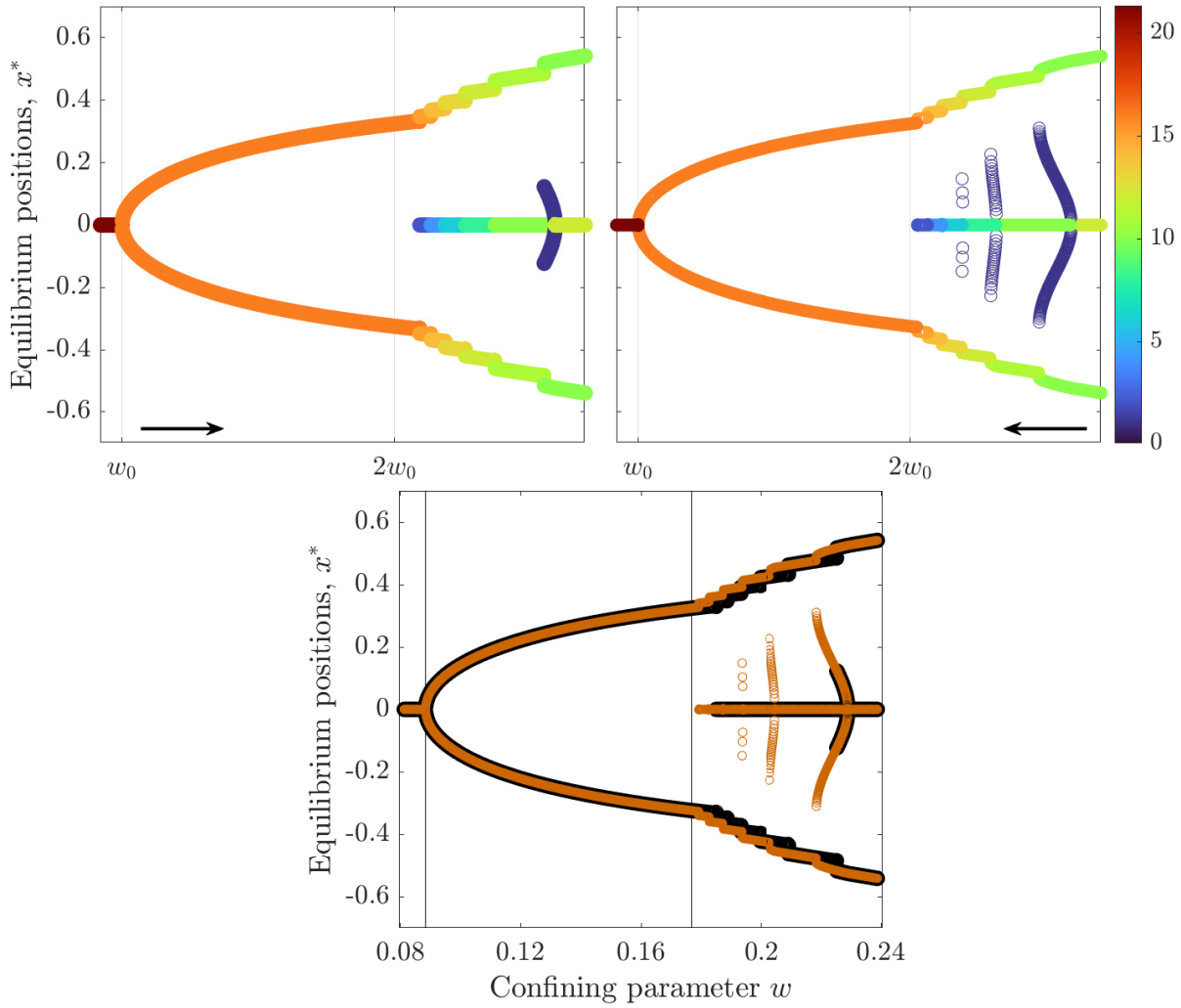

Figure 3.11. **Equilibrium Diagrams, $n = 32$, zoomed.** Bifurcation diagram for 32 particles, zoomed for higher resolution, displaying particle transfer branches and the system's multistability. **Top Left:** Increasing w pass, where particles "fall" to the center only when the outer stacks lose stability at their previous capacity. **Top Right:** Decreasing w, with particles transferring in three visible branches when the central stack becomes "overstuffed" and sheds particles to the outer stacks. **Bottom:** Both passes overlaid to emphasize differences, with forward pass in black and backward pass in orange.

and orange (decreasing-w) passes. The bottom-left figure shows us why; the "free" pair

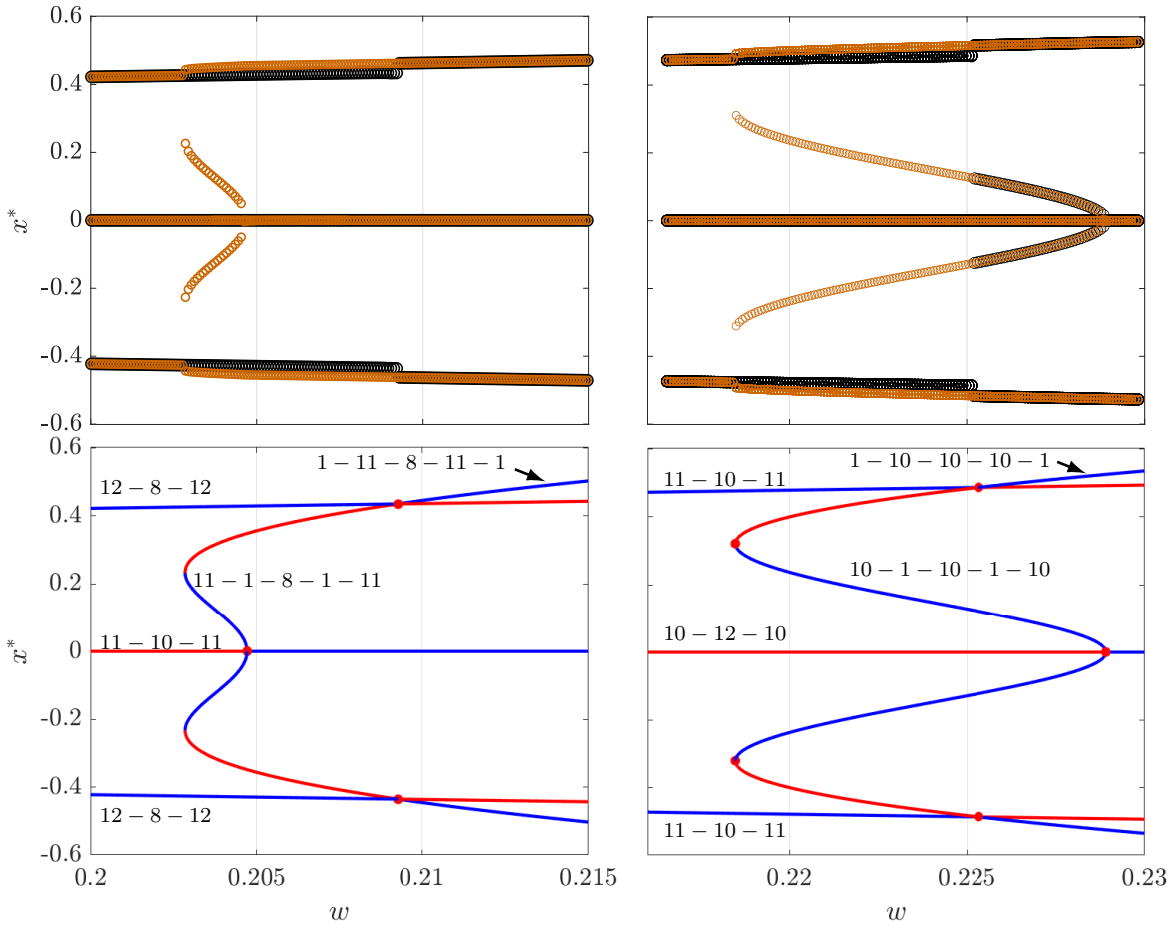

Figure 3.12. **Particle-transfer branches.** Zoom views of central and right "transfer arms" from Fig. 3.11. **Top:** Overlaid scatter plots of the full-population equilibria, for forward (black) and backward (orange) passes. **Bottom:** Stability of states evaluated using MatCont analytical-continuation software, tracking locations where the transferring "free" particle pair can be—with stable positions are shown in blue, and unstable in red. The free pair may align with the other stacks (seen as effectively-horizontal lines, like the state labeled $12-8-12$; these persist through bifurcations but switch stability), or may reside in-between or outside them (e.g., the $11-1-8-1-11$ state which becomes $1-11-8-11-1$ in the bottom-left figure). The left figures explore the empirically observed transition from a $12-8-12$ state on the low w side to $11-10-11$ for higher w, and the right figures explore the transition from $11-10-11$ (lower w) to $10-12-10$ (higher w). For these parameters, $w_0 = 0.0884$.

of particles may only stably exist at the outer stack positions for this parameter value (the central position is red, indicating instability).

As the parameter value increases, this arrangement stays stable until slightly under $w = 0.21$, when we see this branch undergoes a transcritical bifurcation. Theoretically, the pair could drift outward beyond the outer stack at this point, as the lower-left figure indicates, but that diagram assumes the other stacks stay perfectly stacked, while in reality we perturb all particles with noise, and that state isn't robust to that broken symmetry. So what we actually see is that one pair falls to the origin and the rest remain together, corresponding to the $x^* = 0$ stable state in the bottom-left figure, and the overall population state $11 - 10 - 11$.

However, as we decrease w again, the system stays at this $11 - 10 - 11$ state until the branch point near $w = .205$, where the free pair's position follows stable branches away from the origin (in a $11 - 1 - 8 - 1 - 11$ state) until those branches go vertical in an apparent saddle-node bifurcation, at which point the pair jump suddenly to join the outer stacks again. During this bistable region, the position of the outer stacks differs slightly, which is reflected in the disalignment of outer stacks in the top-left figure.

A similar process occurs at slightly higher parameter value, reflected by the right two figures. In this case, the population is transitioning between $11-10-11$ and $10-12-10$ states. The only qualitative difference this time is the transcritical loss of stability at the outer position occurs *before* the central pitchfork bifurcation, so the outer pair is dropped to that branch of the pitchfork in a $10 - 1 - 10 - 1 - 10$ state on the forward pass rather than all the way to the center. On the backwards pass, of course, that $10-1-10-1-10$

state persists longer before losing stability and the transferring particles rejoin the outer stacks.

In this way, we see how bistability occurs between distinct population fractionations. As we can see in Fig. 3.11, the fractionation changes more rapidly when the central stack is small, which we may now understand causes these branches to overlap, yielding multi-stability between more than two fractionation states. Furthermore, as Fig. 3.6 displays, these transitionary states become narrower (in w) as n increases, such that we no longer easily see them at finite resolution. In the infinite-n limit, there is a continuous family of these bifurcations (and corresponding family of transition curves) as the central fractionation changes smoothly rather than in these discrete jumps, and smooth bands of stable fractionation (and corresponding stack positions) accordingly.

3.3.3. Large-n analysis

As Fig. 3.6 suggests, the overall system behavior appears to converge for large numbers of particles, under the appropriate scaling of the w axis. This makes discussion of the large-n limit meaningful—indeed it appears that the rapid "transitionary" bifurcations from the previous section become effectively invisible, while the "major" central stack-birth/stack-splitting bifurcations remain. There is still fractionation indifference (i.e. bands of possible stable population percentages in each stack), and the location of these major bifurcations can still vary meaningfully between forward and backward parameter continuation, as Fig. 3.13 shows.

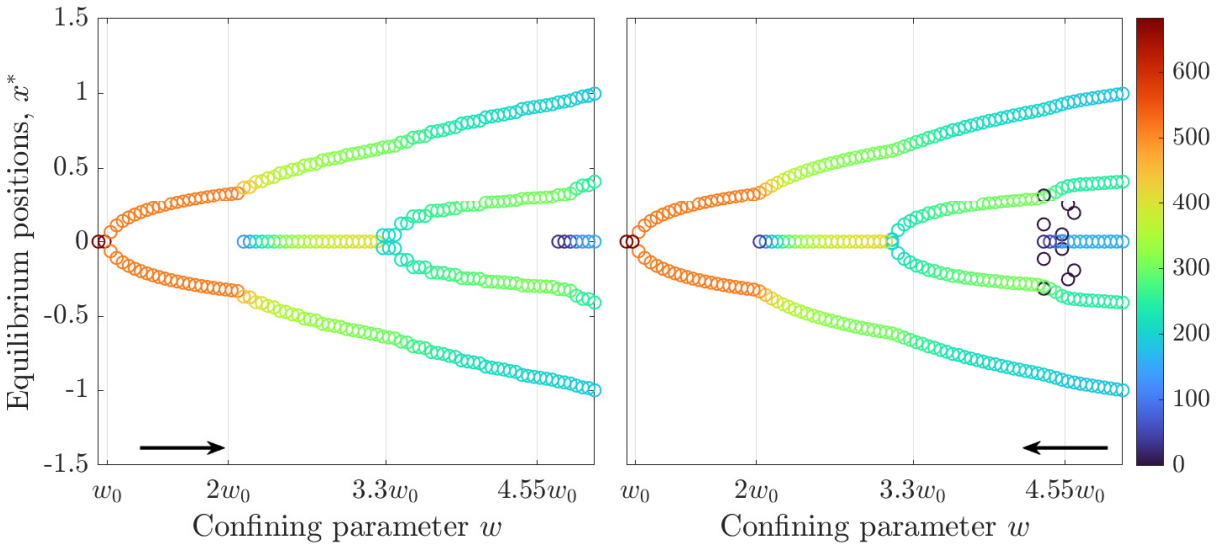

Figure 3.13. **Equilibrium diagrams, large-n forward and backward passes.** Equilibrium diagrams for 1024 particles, with symmetry enforced. Some differences between forward and backward passes indicate the persistence of stability bands: we see different stable fractions of the population at the origin, and correspondingly different bifurcation points of the origin stack.

We can check the stability of particular configurations like we did in Fig. 3.9 for 3 particles, again using the MatCont analytical-continuation software package for Matlab—for example, testing the stable and unstable equilibrium positions of a 129$^{\text{th}}$ "test" particle given 128 particles in two stacks of 64—this is shown in Fig. 3.14.

In Fig. 3.14 we see that the test particle can align with either of the large stacks (desymmetrizing their locations imperceptibly). But we also see that the birth of stability at the origin is in fact due to a second pitchfork bifurcation with very short-lived asymmetric unstable branches which cross the outer stack positions and become stable, roughly corresponding to sitting in the trough outside the two large stacks (and in fact approaching that well location, $\pm 3s/2$, as $w \to \infty$).

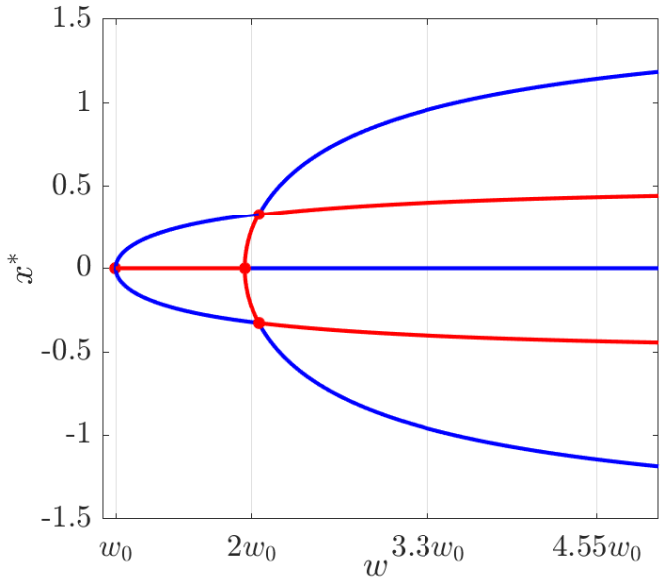

Figure 3.14. **Stable and unstable equilibrium positions for a 129^{th} particle.** Analytical-continuation software Matcont yields the stable (blue) and unstable (red) equilibrium positions for a 129^{th} particle in a system with two perfectly-aligned stacks of 64 particles (which reside at the narrower U-shape, technically but imperceptibly influenced by the position of this 129^{th} particle). We see that the "test particle" can stably align with those two stacks from $w = w_0$ up to slightly above $w = 2w_0$, the latter point occurring right after the birth of stability at the origin. At that point, it must either fall to the center or flee to the outside trough position. In this context, we see stability at the center is born as a pitchfork bifurcation, and we may observe the small region of bistability between $64-65$ and $64-1-64$ states (which includes $2w_0$). For $n = 129$, $w_0 = 0.0442$.

3.4. Analysis

Here we present some analytical results for this system for general n.

3.4.1. General Equilibrium Statement: Existence

For particle j to be at equilibrium:

$$\frac{\mathrm{d}x_j}{\mathrm{d}t} = -\frac{\mathrm{d}U_{tot}}{\mathrm{d}x}\bigg|_{x_j} = 0 = -\frac{2x_j}{w^2} + \sum_{i=1}^{n} \frac{2k^2(x_j - x_i)}{(k-1)s^2}\left(1 - \frac{(x_j - x_i)^2}{s^2}\right) e^{-\frac{k(x_j-x_i)^2}{s^2}} \tag{3.10}$$

If the RHS is positive, particle j will move right, and if negative, left. If it is zero for all particles, the system is at equilibrium. There are many particular states, such as all the particles at the origin $(0, 0, \ldots, 0)$, two symmetric stacks $(x^*, x^*, \ldots, x^*, -x^*, -x^*, \ldots, -x^*)$, etc., which may satisfy this equilibrium condition for various parameter values.

3.4.2. Stability

We can analytically examine the stability of the fully-stacked state at the origin, recovering the critical bifurcation value w_0 below which that state is stable—and in fact appears to be the *only* equilibrium.

The elements of the j^{th} row of the Jacobian matrix for the system (3.10) are

$$\begin{cases} J_{jj} = -\dfrac{2}{w^2} + \dfrac{2k^2}{(k-1)s^2} \displaystyle\sum_{\substack{i=1 \\ i\neq j}}^{n} \left[1 - \frac{3+2k}{s^2}(x_j - x_i)^2 + \frac{2k}{s^4}(x_j - x_i)^4\right] e^{-\frac{k(x_j-x_i)^2}{s^2}} \\ J_{ji} = -\dfrac{2k^2}{(k-1)s^2}\left[1 - \dfrac{3+2k}{s^2}(x_j - x_i)^2 + \dfrac{2k}{s^4}(x_j - x_i)^4\right] e^{-\frac{k(x_j-x_i)^2}{s^2}} \end{cases}, \tag{3.11}$$

which, at the origin (corresponding to the fully-stacked state), yields

$$J_{jj}|_O = -\frac{2}{w^2} + (n-1)\frac{2k^2}{(k-1)s^2} \ ,$$
$$J_{ji}|_O = -\frac{2k^2}{(k-1)s^2} \ .$$

Due to the symmetry, we can identify all the eigenvectors.

(1) The eigenvector $v_1 = (1, 1, \ldots, 1)$ corresponding to the full stack drifting left or right from the origin has eigenvalue $\lambda_1 = -2/w^2$, which is always negative, indicating that the 1-stack system is stable to these types of perturbations (unsurprising based on intuition for a single particle).

(2) The other $n-1$ eigenvectors consist solely of symmetric two-particle divergence; i.e., vectors of the form $(-1, 1, 0, 0, \ldots, 0)$ with the positive 1 in each of the other $n-1$ positions. These vectors all have eigenvalue $\lambda = -2/w^2 + 2nk^2/(k-1)s^2$. The 1-stack state is thus stable to these types of perturbations for

$$\frac{w}{s} < \frac{1}{k}\sqrt{\frac{k-1}{n}} \ . \tag{3.12}$$

Solving for w, this gives us the critical parameter value w_0 for general n:

$$w_0 = \frac{s}{k}\sqrt{\frac{k-1}{n}} \ . \tag{3.13}$$

We note that this agrees with the $n = 2$ particular case, Eq. (3.8). This also suggests the appropriate way to rescale the w axis as n varies, since the structure appears (at least asymptotically for large n) to depend only on the ratio w/w_0.

3.4.3. Two-stack state

The simplest nontrivial arbitrary-n case, the two-*stack* state—where the population is split into two symmetric stacks of $n/2$ particles each—is quite relevant to examine since it is the dominant behavior for approximately $w_0 < w < 2w_0$. It is exactly solvable via a simple tweak of the logic which led us to Eq. (3.5), with the influence from the other "particle" being multiplied by $n/2$ while the background contribution is unchanged:

$$\begin{aligned}
\left.\frac{\mathrm{d}U_{tot}}{\mathrm{d}x}\right|_{x^*} = 0 &= \frac{2x^*}{w^2} - \left(\frac{n}{2}\right)\frac{4k^2x^*}{(k-1)s^2}\left(1-4\frac{x^{*2}}{s^2}\right)e^{-\frac{4kx^{*2}}{s^2}} \\
0 &= 2x^*\left[\frac{1}{w^2} - \frac{nk^2}{(k-1)s^2}\left(1-4\frac{x^{*2}}{s^2}\right)e^{-\frac{4kx^{*2}}{s^2}}\right] \\
\implies x^* &= 0 \qquad \text{or} \\
w^2 &= \frac{s^2(k-1)}{nk^2}\frac{1}{1-4\frac{x^{*2}}{s^2}}e^{\frac{4kx^{*2}}{s^2}} \\
w^2 &= w_0^2\frac{e^{\frac{4kx^{*2}}{s^2}}}{1-4\frac{x^{*2}}{s^2}} \qquad (3.14)
\end{aligned}$$

3.4.4. Return of stability at the origin

We seek an understanding of the second "major" bifurcation: the birth of the three-stack state near $w = 2w_0$, with a small central stack between the two large symmetric stacks. We can easily check the curvature of the potential landscape at the origin between two equal stacks, using this as a test to identify when a particle would stably rest there. We

note that this spot sees an identical contribution from all particles at $\pm x^*$:

$$\left.\frac{\mathrm{d}^2 U_{tot}}{\mathrm{d}x^2}\right|_{x=0} = \frac{2}{w^2} + n\left[-\frac{2k^2}{(k-1)s^2}\left(1 - \frac{2k+3}{s^2}x^{*2} + \frac{2k}{s^4}x^{*4}\right)e^{-\frac{kx^{*2}}{s^2}}\right]$$
$$= \frac{2}{w^2} - \frac{2}{w_0^2}\left(1 - \frac{2k+3}{s^2}x^{*2} + \frac{2k}{s^4}x^{*4}\right)e^{-\frac{kx^{*2}}{s^2}};,$$

so the birth of stability happens when this curvature crosses 0, at

$$w_c^2 = w_0^2 \frac{e^{\frac{kx^{*2}}{s^2}}}{1 - \frac{2k+3}{s^2}x^{*2} + \frac{2k}{s^4}x^{*4}}\ . \tag{3.15}$$

When we combine this condition with the two-stack equilibrium relation for w^2, Eq. (3.14), we get

$$w_0^2 \frac{e^{\frac{kx_c^{*2}}{s^2}}}{1 - \frac{2k+3}{s^2}x_c^{*2} + \frac{2k}{s^4}x_c^{*4}} = w_0^2 \frac{e^{\frac{4kx_c^{*2}}{s^2}}}{1 - 4\frac{x_c^{*2}}{s^2}}$$
$$1 - 4\frac{x_c^{*2}}{s^2} = \left(1 - \frac{2k+3}{s^2}x_c^{*2} + \frac{2k}{s^4}x_c^{*4}\right)e^{\frac{3kx_c^{*2}}{s^2}}\ , \tag{3.16}$$

which defies closed-form solution but which we may numerically approximate for our default parameters $k = 2$ and $s = 1$, yielding $x_c^* \approx 0.324$. We can see that this agrees empirically with the stack width coincident with the birth of stability in our large-n figures like Figs. 3.4 and 3.13.

This approximation for x^* in turn allows us to approximate w_c, by using either relation again. Using Eq. (3.14) with $k = 2, s = 1$, we have

$$w_c^2 = w_0^2 \frac{e^{8x_c^{*2}}}{1 - 4x_c^{*2}} ,$$

$$x_c^* \approx 0.324176\ldots$$

$$\implies w_c \approx 1.99978 w_0 .$$

This is suspiciously close to $2w_0$, but these approximations were done using 16-digit precision, so it appears to indeed be distinct. We note that this value depends on k (though s may be scaled out as always); for example, for $k = 100$ we have $w_{c,100} \approx 1.791 w_0$.

After the central stack's creation, the exchange of particles between central and outer stacks is complicated, since the fraction of the population at the origin influences the position of the outer stacks, which in turn influences the stable fraction at the origin. We observe empirically that the outer stacks drift apart in a roughly linear manner, which may be helpful, though we leave this exploration for future work.

We note that the increasing-w sweep only sees particles at the center when they are kicked out of the outer stacks to populate it. On the decreasing-w pass, however, the center hosts a larger stable population at each w value reached, since continuation from the right causes the accumulation of all nearby particles at the center, where they stay until they are ejected to the outer stacks. It is perhaps counterintuitive that these particles "climb" the global potential as it narrows, but it is nevertheless true; the narrowing background potential pushes the outer stacks inward enough that the center becomes less stable, at

which point it is "overstuffed" and repels some of its former constituents to join the other stacks.

The decreasing pass thus acts as a lower bound for the *maximal* stable fraction at the center, and the increasing pass acts as an upper bound on the *minimal* stable fractionation. We expect a continuous band of stable fractionations between those values, as indicated by Fig. 3.15. We leave further exploration of the bands of stability in the $n \to \infty$ limit for future work.

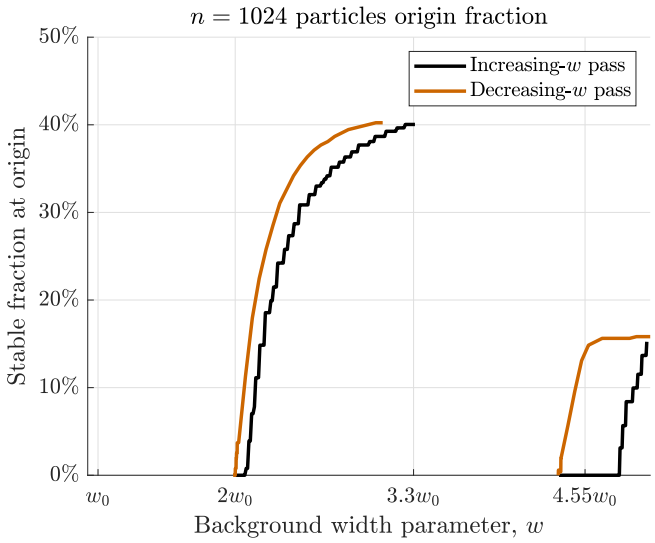

Figure 3.15. **Origin fractionation bands, $n = 1024$.** Fraction of population at origin for forward and backward passes with small noise. These curves demonstrate the existence of bands of stability, and are an approximation of those bands. The true bands may be slightly wider, but the fractionations between these curves are stable for corresponding w values.

3.5. Discussion/Conclusion

We have examined a system of particles with first-order coupling through Ricker wavelet potential functions, and found remarkably rich self-organizing behavior. Intuitive small-n cases transition to archetypal large-n limiting behavior, with non-origin bifurcations becoming compacted into invisibility while other, "major" bifurcations (those regarding stability of the origin) persist and stabilize for large n. Multi-stability abounds, and persists for large n; overlapping hysteresis in the position of individual particles becomes stability bands for fractions of the population.

There is plenty more to be explored with these particles. We have not systematically examined dependence on the parameter k, which controls trough depth, though we showcase some promising initial findings in section 3.S.2 below. Also of interest is the oscillator interpretation, with these particles living on a finite periodic domain, for which we present some intriguing initial findings. Behavior with other types of confinement, such as a finite "hard-walled" box, is also an open question. Some of these model variants may lend themselves to real-world applications such as those mentioned in the introduction.

We hope this work provides a solid foundation for the exploration of this system and its variants, which offer tantalizing glimpses of order governing a wild dynamical zoo of possible behavior.

3.S. Extra Findings

3.S.1. Fresh random starts

Without continuation—i.e., when the simulation at each w value proceeds from an entirely random starting state rather than a slightly-perturbed version of the previous

equilibrium—we see a "fuzzier" but ultimately similar picture; see Fig. 3.S16. This does yield some information about the system's tolerance for asymmetry; the two-stack state for $n = 128$ can be as lopsided as $68-60$ in this run and still appear stable. More lopsided stable two-stack states may be possible with biased initial conditions, however.

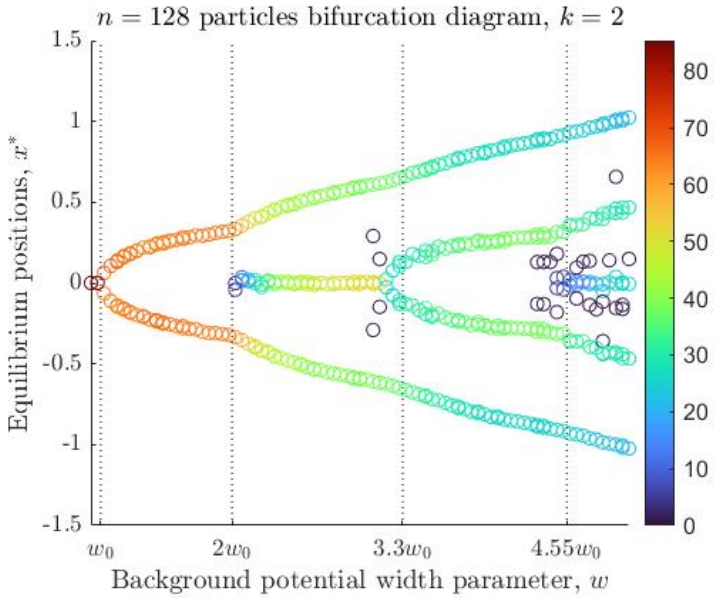

Figure 3.S16. **Equilibrium diagram without continuation.** Equilibrium states with a fresh Gaussian random start every time. Stack size here gives a lower bound for tolerance of asymmetric fractionation; the greatest asymmetry in the two-stack state observed here is $68 - 60$.

3.S.2. k dependence

The parameter k distorts the equilibrium diagram; Fig. 3.S17 shows what happens when k grows. We see that large k coincides with a narrower population (smaller range on vertical axis); this is perhaps unintuitive since large k makes the Ricker wavelet's trough shallower, which intuitively means less stability, and perhaps the dominance of repulsion. However, that would imply a wider population, while we see a narrower one. We might

instead take away the competing explanation that the Ricker wavelets' weaker attraction to their preferred distance means the particles don't "buoy" their partners away from the origin as strongly, which leads to more dominance of the background potential-well containment overall.

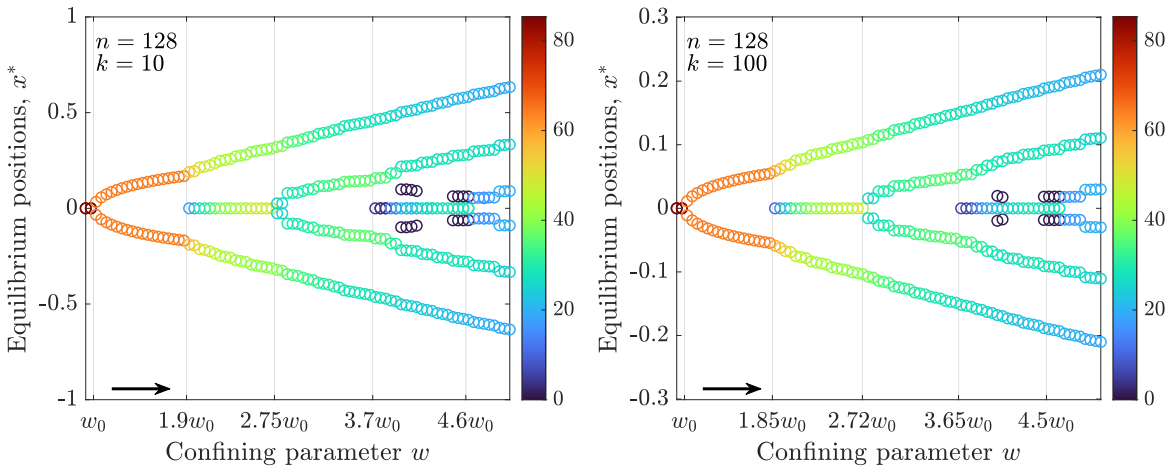

Figure 3.S17. k **dependence.** Equilibrium diagrams for higher values of k. The estimated bifurcation values are marked on the w axis. Larger k appears to accelerate the bifurcation rate, but with diminishing returns– these diagrams' qualitative and quantitative similarity suggests a large-k limit is potentially well-defined. It is important to note the vertical axis scale is different, however; any additional invariance involved in this limit would involve a rescaling the vertical (spatial) axis as well as the existing horizontal axis scaling (implicit in w_0 dependence, since $w_0 \propto k^{-1/2}$).

3.S.3. Lennard-Jones and Morse potentials

As mentioned in Section 3.1, the Lennard-Jones and Morse potentials from physics are models of intermolecular potential energy with short-range repulsion and long-range attraction. These potentials may be described in the following forms:

$$U_{\mathrm{LJ}}(x) = 4\epsilon \left[\left(\frac{x}{\sigma}\right)^{-12} - \left(\frac{x}{\sigma}\right)^{-6} \right] ,$$

$$U_{\mathrm{M}}(x) = D_e \left[e^{-2a(|x|-r_e)} - 2e^{-a(|x|-r_e)} \right] .$$

Fig. 3.S18 shows examples of these potential functions, with as much matching to our default Ricker potential as possible. In particular, this should highlight the limits of their qualitative comparability, and why alteration to a "soft-core" potential amenable to "stacking"/coexistence would be necessary to expect results similar to those presented in this work.

3.S.4. Ricker Oscillators

A model variant of considerable interest for these Ricker-potential-coupled particles is their implementation as coupled oscillators. In this case, their position would represent phase on a periodic domain, like $(-\pi, \pi]$). A slight tweak to the Ricker potential would need to be defined to make it periodic; distance between particles in this space might be taken to be the shortest distance around the circle, or the infinite sum of possible distance interpretations at all $\pm 2\pi m$ multiples, or the potential itself might be made periodic in some other way. In any case, the parameter s (controlling the location of the troughs,

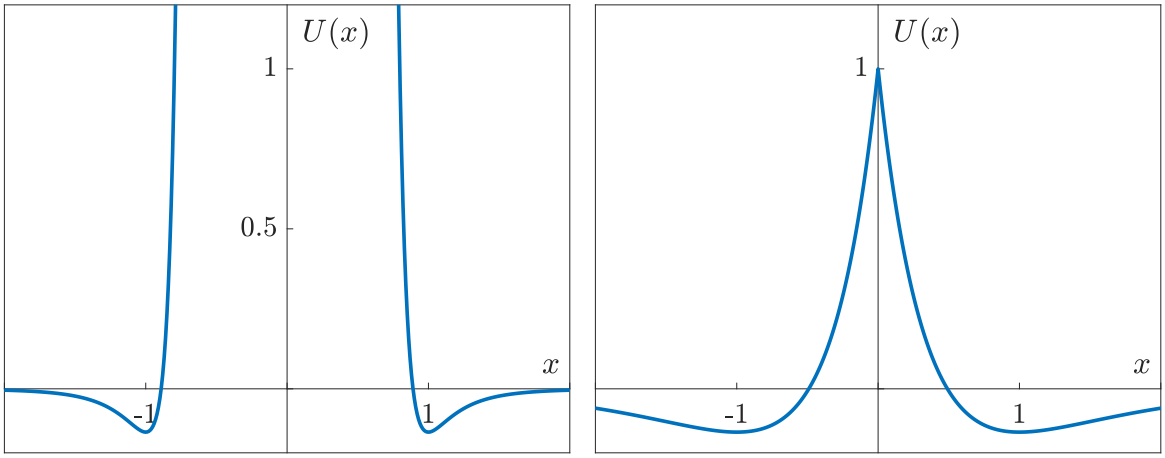

Figure 3.S18. **Other Classic Potentials.** Examples of the Lennard-Jones (**left**) and Morse (**right**) potentials from physics. Parameters have been chosen to match the trough coordinates of our default-parameter Ricker potential—$(\pm 1, e^{-2})$—and the peak of $(0, 1)$ for the Morse potential. Still, we note significant qualitative discrepancies, namely the infinite central spike for Lennard-Jones and the "sharp" origin peak for Morse. These qualities preclude the stability (or even well-defined status) of stacking behavior, and thus the particular richness of behavior we find in our Ricker system, but alterations to smooth behavior at the origin may lead to reconciliation.

which acts as a "preferred distance") is no longer removable by scaling in this paradigm; its ratio with the domain is a qualitatively important value.

Using the simpler, shortest-distance interpretation, we performed simulations and demonstrate the results in Fig. 3.S19. We found that for small n, the particles did settle uniformly at intervals of s. Sometimes the system took a long time to find this state, as it evolves more slowly when evenly spaced—even when the population is more compact than necessary.

However, at large n (such that n times the preferred distance was much larger than 2π), the system appeared to exhibit "frozen disorder," or a "glassy" state where particles neither clump nor uniformly distribute (see Fig. 3.S20). The best lens for understanding

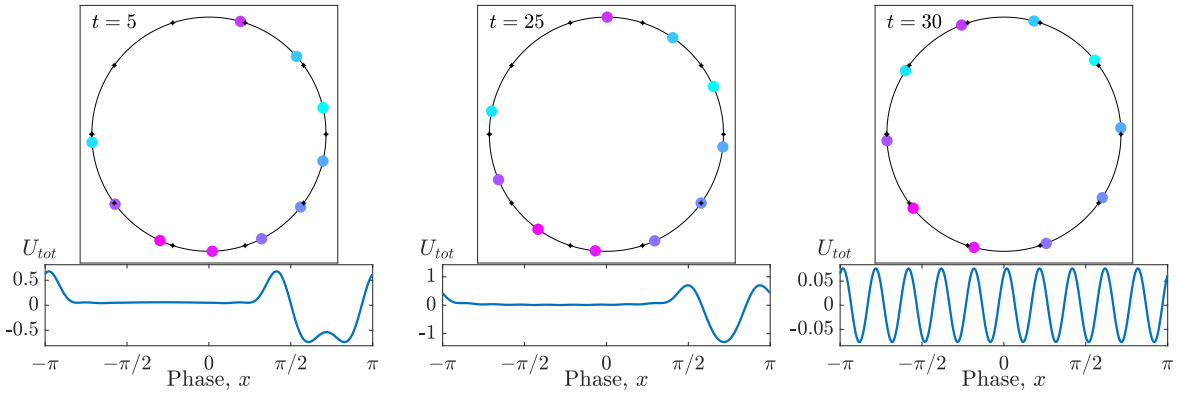

Figure 3.S19. **Oscillator interpretation, slow convergence.** Ten Ricker oscillators with preferred distance $2\pi/10$. The left figure shows the system at time $t = 5$, central figure at $t = 25$, and right figure at $t = 30$; the population swiftly self-arranges to become near-evenly but too-compactly arranged, then slowly separates, until suddenly "snapping" to perfectly even spacing. Black dots around circle indicate preferred distance; we see the particles eventually space themselves at the same intervals. Color indicates particle index, to distinguish and keep track of them over time.

this process appears to be the global potential; as the population evolves, it appears to self-organize almost instantly into a single low frequency wave (created by many individual Ricker potentials) which then damps quickly to reveal middle frequencies at smaller amplitude. As the magnitude of this global potential wave shrinks beneath the scale of a single wavelet, the inherent higher frequencies of individual particles emerge again (see Fig. 3.S20, bottom right).

This apparent phenomenon of self-organization in service of the global potential's frequency-damping is only a numerical observation thus far, and merits future analytical exploration. It is unclear if this disordered state is truly stable or merely quasi-stable, and how the parameter-space transition from even-spacing to disordered "equilibrium" occurs as the domain becomes overpopulated relative to the preferred distance. We believe this is a ripe area for future exploration.

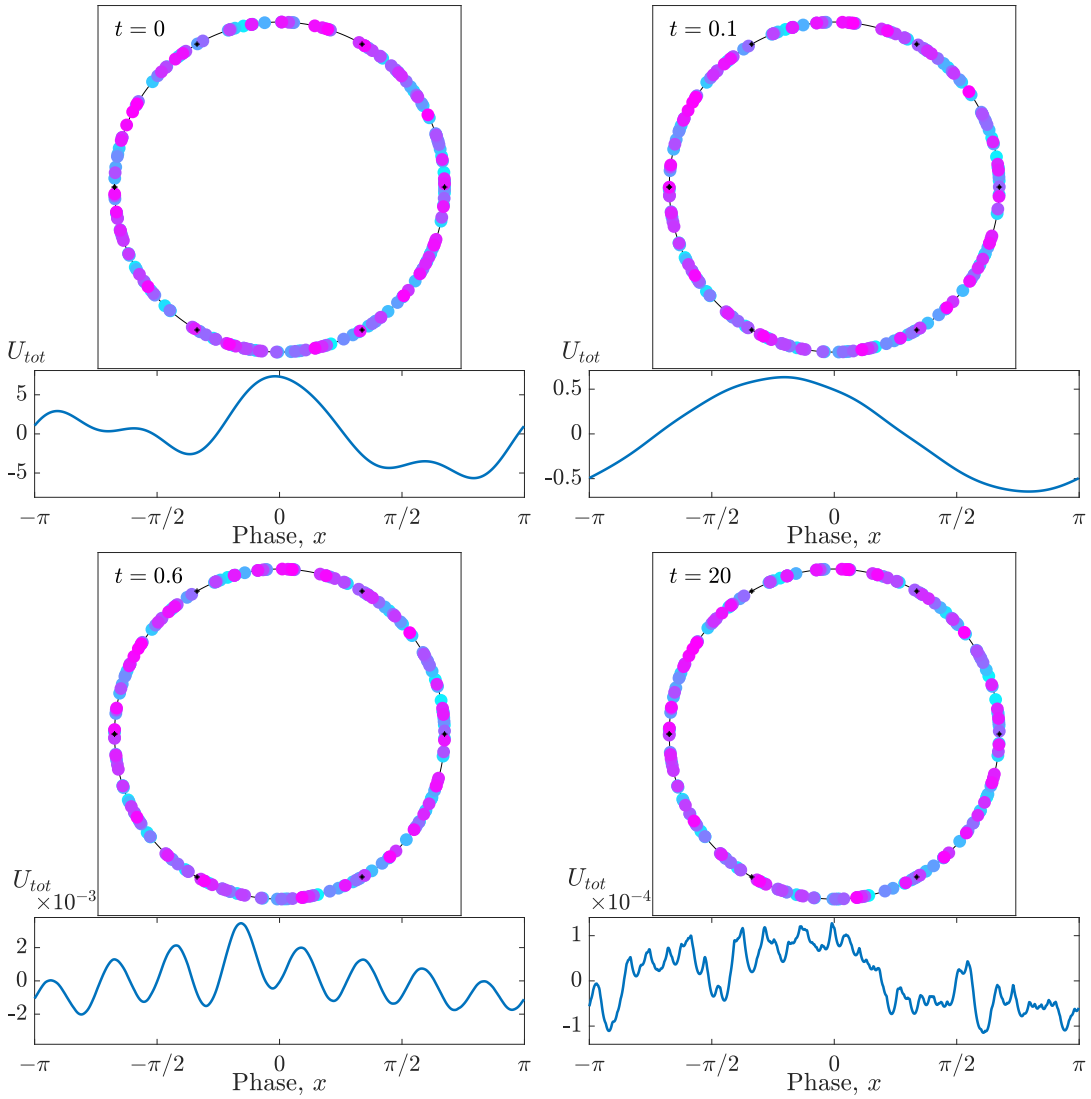

Figure 3.S20. **Ricker oscillator system.** Two hundred Ricker oscillators with preferred distance $2\pi/6$. **Top left:** Random starting state. **Top right:** At $T = 0.1$, the particles have very quickly arranged themselves into a single low-frequency global-potential wave. **Bottom left:** At $T = 0.6$, the low-frequency wave has damped, leaving a mid-frequency wave (with period $2\pi/8$, higher frequency than the Ricker wavelet's preferred distance) of much lower amplitude (two orders of magnitude smaller), with only minute positional adjustments. **Bottom right:** At $T = 20$, the global potential has damped another order of magnitude, to 4×10^{-4}, leaving only the high-frequency spikes of individual Ricker wavelets (which have a "sharp" nondifferentiable corner as they wrap around $\pm\pi$). This "glassy" and distinctly nonuniform state appears to be stable, though it might only be extremely slow to evolve.

References

[1] David Sabin-Miller and Daniel M. Abrams. When pull turns to shove: A continuous-time model for opinion dynamics. *Physical Review Research*, 2:043001, Oct 2020.

[2] David Sabin-Miller and Daniel M Abrams. Modeling and analysis of systems with nonlinear functional dependence on random quantities. *arXiv preprint arXiv:2210.03781*, 2022.

[3] Christopher A Bail, Lisa P Argyle, Taylor W Brown, John P Bumpus, Haohan Chen, MB Fallin Hunzaker, Jaemin Lee, Marcus Mann, Friedolin Merhout, and Alexander Volfovsky. Exposure to opposing views on social media can increase political polarization. *Proceedings of the National Academy of Sciences*, 115(37):9216–9221, 2018.

[4] Annick Dhooge, Willy Govaerts, Yu A Kuznetsov, Hil Gaétan Ellart Meijer, and Bart Sautois. New features of the software matcont for bifurcation analysis of dynamical systems. *Mathematical and Computer Modelling of Dynamical Systems*, 14(2):147–175, 2008.

[5] Richard A. Holley and Thomas M. Liggett. Ergodic theorems for weakly interacting infinite systems and the voter model. *The Annals of Probability*, 3(4):643–663, 08 1975.

[6] Guillaume Deffuant, David Neau, Frederic Amblard, and Gérard Weisbuch. Mixing beliefs among interacting agents. *Advances in Complex Systems*, 3(01n04):87–98, 2000.

[7] Rainer Hegselmann and Ulrich Krause. Opinion dynamics and bounded confidence models, analysis, and simulation. *Journal of Artificial Societies and Social Simulation*, 5(3), 2002.

[8] V. Sood and S. Redner. Voter model on heterogeneous graphs. *Physical Review Letters*, 94:178701, May 2005.

[9] Claudio Castellano, Miguel A. Muñoz, and Romualdo Pastor-Satorras. Nonlinear q-voter model. *Physical Review E*, 80:041129, Oct 2009.

[10] Rainer Hegselmann and Ulrich Krause. Opinion dynamics driven by various ways of averaging. *Computational Economics*, 25(4):381–405, 2005.

[11] Serge Galam and Frans Jacobs. The role of inflexible minorities in the breaking of democratic opinion dynamics. *Physica A: Statistical Mechanics and its Applications*, 381:366–376, 2007.

[12] André CR Martins. Continuous opinions and discrete actions in opinion dynamics problems. *International Journal of Modern Physics C*, 19(04):617–624, 2008.

[13] Gunjan Verma, Ananthram Swami, and Kevin Chan. The impact of competing zealots on opinion dynamics. *Physica A: Statistical Mechanics and its Applications*, 395:310–331, 2014.

[14] D. Knopoff. On a mathematical theory of complex systems on networks with application to opinion formation. *Mathematical Models and Methods in Applied Sciences*, 24(02):405–426, 2014.

[15] Zhihong Liu, Jianfeng Ma, Yong Zeng, Li Yang, Qiping Huang, and Hongliang Wu. On the control of opinion dynamics in social networks. *Physica A: Statistical Mechanics and its Applications*, 409:183–198, 2014.

[16] Shaoli Wang, Libin Rong, and Jianhong Wu. Bistability and multistability in opinion dynamics models. *Applied Mathematics and Computation*, 289:388–395, 2016.

[17] Michela Del Vicario, Antonio Scala, Guido Caldarelli, H Stanley, and Walter Quattrociocchi. Modeling confirmation bias and polarization. *Scientific Reports*, 7:40391, 06 2016.

[18] Juan Pablo Pinasco, Viktoriya Semeshenko, and Pablo Balenzuela. Modeling opinion dynamics: Theoretical analysis and continuous approximation. *Chaos, Solitons & Fractals*, 98:210–215, 2017.

[19] Mohammad Hadi Afrasiabi, Roch Guérin, and SS Venkatesh. Opinion formation in Ising networks. *Online Social Networks and Media*, 5:1–22, 2018.

[20] Serge Galam. Rational group decision making: A random field Ising model at t= 0. *Physica A: Statistical Mechanics and its Applications*, 238(1-4):66–80, 1997.

[21] Serge Galam. Contrarian deterministic effects on opinion dynamics: "the hung elections scenario". *Physica A: Statistical Mechanics and its Applications*, 333:453–460, 2004.

[22] Katarzyna Sznajd-Weron and Jozef Sznajd. Opinion evolution in closed community. *International Journal of Modern Physics C*, 11(06):1157–1165, 2000.

[23] Katarzyna Sznajd-Weron. Sznajd model and its applications. *Acta Physica Polonica B*, 36:2537, 2005.

[24] Giuseppe Toscani et al. Kinetic models of opinion formation. *Communications in Mathematical Sciences*, 4(3):481–496, 2006.

[25] Maria Letizia Bertotti and Marcello Delitala. On a discrete generalized kinetic approach for modelling persuader's influence in opinion formation processes. *Mathematical and Computer Modelling*, 48(7-8):1107–1121, 2008.

[26] Bertram Düring, Peter Markowich, Jan-Frederik Pietschmann, and Marie-Therese Wolfram. Boltzmann and fokker–planck equations modelling opinion formation in the presence of strong leaders. *Proceedings of the Royal Society A: Mathematical, Physical and Engineering Sciences*, 465(2112):3687–3708, 2009.

[27] Bertram Düring and Marie-Therese Wolfram. Opinion dynamics: inhomogeneous boltzmann-type equations modelling opinion leadership and political segregation. *Proceedings of the Royal Society A: Mathematical, Physical and Engineering Sciences*, 471(2182):20150345, 2015.

[28] Claudio Castellano, Santo Fortunato, and Vittorio Loreto. Statistical physics of social dynamics. *Reviews of Modern Physics*, 81:591–646, May 2009.

[29] Tim Groseclose and Jeffrey Milyo. A measure of media bias. *The Quarterly Journal of Economics*, 120(4):1191–1237, 2005.

[30] Robert M Entman. Framing bias: Media in the distribution of power. *Journal of Communication*, 57(1):163–173, 2007.

[31] Michael D. Slater. Reinforcing spirals: The mutual influence of media selectivity and media effects and their impact on individual behavior and social identity. *Communication Theory*, 17(3):281–303, 07 2007.

[32] Stefano DellaVigna and Ethan Kaplan. The Fox News effect: Media bias and voting. *The Quarterly Journal of Economics*, 122(3):1187–1234, 2007.

[33] Gregory J. Martin and Ali Yurukoglu. Bias in cable news: Persuasion and polarization. *American Economic Review*, 107(9):2565–99, September 2017.

[34] Daron Acemoglu and Asuman Ozdaglar. Opinion dynamics and learning in social networks. *Dynamic Games and Applications*, 1(1):3–49, 2011.

[35] Kangqi Fan and Witold Pedrycz. Evolution of public opinions in closed societies influenced by broadcast media. *Physica A: Statistical Mechanics and its Applications*, 472:53–66, 2017.

[36] Keith T Poole and Howard Rosenthal. The polarization of American politics. *The Journal of Politics*, 46(4):1061–1079, 1984.

[37] Pew Research Center. The partisan divide on political values grows even wider. Technical report, October 2017.

[38] Christopher Hare and Keith T Poole. The polarization of contemporary American politics. *Polity*, 46(3):411–429, 2014.

[39] Pew Research Center. Partisanship and political animosity in 2016. Technical report, June 2016.

[40] Henri Tajfel and John C Turner. An integrative theory of intergroup conflict. In *Organizational Identity: A Reader*, chapter 4, pages 56–65. Oxford University Press Oxford, United Kingdom, 1979.

[41] Vanessa Otero. Media bias chart: Version 5.0. *Accessed at https://www.adfontesmedia.com/*, 2020.

[42] William Coffey and Yu P Kalmykov. *The Langevin equation: With applications to stochastic problems in physics, chemistry and electrical engineering*, volume 27. World Scientific, 2012.

[43] Crispin Gardiner. *Stochastic Methods*, volume 4. Springer Berlin, 2009.

[44] Nicolaas G Van Kampen. Itô versus Stratonovich. *Journal of Statistical Physics*, 24(1):175–187, 1981.

[45] Jörn Dunkel and Peter Hänggi. Theory of relativistic brownian motion: the (1+ 1)-dimensional case. *Physical Review E*, 71(1):016124, 2005.

[46] Hans Fischer. *A history of the central limit theorem: From classical to modern probability theory*. Springer Science & Business Media, 2010.

[47] F.S. Hover and M.S. Triantafyllou. Galloping response of a cylinder with upstream wake interference. *Journal of Fluids and Structures*, 15(3):503 – 512, 2001.

[48] Hilbert J. Kappen. Linear theory for control of nonlinear stochastic systems. *Physical Review Letters*, 95:200201, Nov 2005.

[49] Weihai Zhang, Bor-Sen Chen, and Chung-Shi Tseng. Robust H-infinity filtering for nonlinear stochastic systems. *IEEE Transactions on Signal Processing*, 53(2):589–598, 2005.

[50] Nadav Berman and Uri Shaked. H-infinity-like control for nonlinear stochastic systems. *Systems & Control Letters*, 55(3):247–257, 2006.

[51] Robert H Kraichnan. Dynamics of nonlinear stochastic systems. *Journal of Mathematical Physics*, 2(1):124–148, 1961.

[52] B. V. Gnedenko and A. N. Kolmogorov. *Limit distributions for sums of independent random variables*. Addison-Wesley Mathematics Series. Addison-Wesley, Cambridge, MA, 1954. Translated and annotated by K. L. Chung. With an Appendix by J. L. Doob.

[53] Gisiro Maruyama. Continuous Markov processes and stochastic equations. *Rendiconti del Circolo Matematico di Palermo*, 4(1):48, 1955.

[54] George E Uhlenbeck and Leonard S Ornstein. On the theory of the Brownian motion. *Physical Review*, 36(5):823, 1930.

[55] Ming Chen Wang and George Eugene Uhlenbeck. On the theory of the Brownian motion II. *Reviews of Modern Physics*, 17(2–3):323, 1945.

[56] Nicolaas Godfried Van Kampen. *Stochastic processes in physics and chemistry*. Elsevier, 2007.

[57] Daniel T Gillespie. *Markov processes: an introduction for physical scientists*. Elsevier, 1991.

[58] John C Slater. A simplification of the hartree-fock method. *Physical review*, 81(3):385, 1951.

[59] Yoshiki Kuramoto. Self-entrainment of a population of coupled non-linear oscillators. In *International symposium on mathematical problems in theoretical physics*, pages 420–422. Springer, 1975.

[60] Z Csahók, F Family, and T Vicsek. Transport of elastically coupled particles in an asymmetric periodic potential. *Physical Review E*, 55(5):5179, 1997.

[61] Peter Schwerdtfeger, Nicola Gaston, Robert P Krawczyk, Ralf Tonner, and Gloria E Moyano. Extension of the lennard-jones potential: Theoretical investigations into rare-gas clusters and crystal lattices of he, ne, ar, and kr using many-body interaction expansions. *Physical Review B*, 73(6):064112, 2006.

[62] J.W.J. Hosken. Ricker wavelets in their various guises. *First Break*, 6(1), 1988.

[63] Yanghua Wang. The Ricker wavelet and the Lambert W function. *Geophysical Journal International*, 200(1):111–115, 11 2014.

[64] Joseph D Johnson and Daniel M Abrams. A coupled oscillator model for the origin of bimodality and multimodality. *Chaos: An Interdisciplinary Journal of Nonlinear Science*, 29(7):073120, 2019.

[65] Claude Cohen-Tannoudji, Bernard Diu, and Franck Laloë. *Quantum Mechanics, Volume 3: Fermions, Bosons, Photons, Correlations, and Entanglement*. John Wiley & Sons, 2019.

[66] P. M. M. Maessen, Th. A. Rijken, and J. J. de Swart. Soft-core baryon-baryon one-boson-exchange models. ii. hyperon-nucleon potential. *Phys. Rev. C*, 40:2226–2245, Nov 1989.

[67] Th A Rijken, VGJ Stoks, and Y Yamamoto. Soft-core hyperon-nucleon potentials. *Physical Review C*, 59(1):21, 1999.

[68] G. Yatsenko, E. J. Sambriski, M. A. Nemirovskaya, and M. Guenza. Analytical soft-core potentials for macromolecular fluids and mixtures. *Phys. Rev. Lett.*, 93:257803, Dec 2004.

[69] G Bard Ermentrout and Nancy Kopell. Parabolic bursting in an excitable system coupled with a slow oscillation. *SIAM journal on applied mathematics*, 46(2):233–253, 1986.

[70] Bard Ermentrout. Type i membranes, phase resetting curves, and synchrony. *Neural computation*, 8(5):979–1001, 1996.

[71] Frank C Hoppensteadt and Eugene M Izhikevich. *Weakly connected neural networks*, volume 126. Springer Science & Business Media, 1997.